Inaugural Dissertation

Human presynaptic active zone: basic biology and disease

Joaquín Damián Joacaz Campos Muñoz

2025

Inaugural Dissertation

for

obtaining the doctoral degree of the

Combined Faculty of Mathematics, Engineering and Natural Sciences

of the

Ruprecht - Karls – University Heidelberg

Presented by

M.Sc. Joaquín Damián Joacaz Campos Muñoz

born in: Santiago, Chile

Oral examination: May 28th, 2025

Human presynaptic active zone: basic biology and disease

Referees: Prof. Dr. med. Christian Schaaf

Prof. Dr. rer. nat. Gudrun A. Rappold

Abstract

Presynaptic terminals release neurotransmitter in response to incoming electrical impulses, control information transfer between neurons in neural networks, and mediate directly or indirectly most brain functions. In humans, dysfunction of presynaptic terminals contributes to devastating brain disorders such as Alzheimer, schizophrenia, and autism. However, despite of its obvious significance, how defects in the function of presynaptic terminals contribute to the etiology of brain disorders, remains largely unknown. This is because not even the most fundamental operation principles of normal human nerve terminals are well-understood, let alone their dysfunction in disease.

Here, I study the basic biology of human presynaptic terminals, as well as their dysregulation in autism-spectrum disorder (ASD). I focus on a protein family called RIMs (Rab interacting molecules), which are central components of the presynaptic active zones. I capitalized on emerging human pluripotent stem-cell technologies to generate human neurons, on CRISPR/Cas9 genome editing to genetically engineer human neurons and create disease models, and on advanced physiological and microscopy technologies to uncover the basic biology of human presynaptic terminals as well as their dysfunction in ASD. Remarkably, I found that compound genetic removal of both RIM1 and RIM2, the main brain RIM isoforms, disassembles human active zones (AZ), prevents synaptic vesicle docking and priming, and blocks synaptic vesicle fusion, rendering human presynaptic terminals functionally silent. Genetic experiments in which either RIM1 or RIM2 are selectively deleted, revealed that RIM1 is the functionally dominant isoform in human neurons.

As RIM1 is also a common target of mutations in autistic patients, I generated a panel of knock-in lines comprising all currently described ASD-linked mutations in RIM1, and analyzed systematically their impact on human neuron structure and function. I found that all these disease-linked variants dysregulated human synaptic communication via two convergent mechanisms: impairing either vesicle priming or calcium channel coupling to synaptic vesicles. Importantly, this translates into enhanced or reduced information flow across neural human networks, highlighting the critical role of balanced neurotransmission in the pathogenesis of neuropsychiatric disorders.

My work offers a unifying view on the basic biology of human active zones and their dysregulation in autism. To the best of my knowledge, this study represents the first effort aiming to understand how normal human presynaptic terminals work, and how brain disease

affects them. Along this line, here I contribute to future efforts aiming to the development of new therapeutic strategies to reverse common presynaptic mechanisms disrupted in autistic patients.

Zusammenfassung

Präsynaptische Endigungen setzen Neurotransmitter als Reaktion auf eintreffende elektrische Impulse frei, steuern die Informationsübertragung zwischen Neuronen in neuronalen Netzwerken und vermitteln direkt oder indirekt die meisten Gehirnfunktionen. Beim Menschen trägt eine Fehlfunktion präsynaptischer Endigungen zu schwerwiegenden Gehirnerkrankungen wie Alzheimer, Schizophrenie und Autismus bei. Trotz ihrer offensichtlichen Bedeutung bleibt jedoch weitgehend unbekannt, wie Defekte in der Funktion präsynaptischer Endigungen zur Entstehung von Gehirnerkrankungen beitragen. Dies liegt daran, dass selbst die grundlegendsten Funktionsprinzipien normaler menschlicher Nerventerminals nicht gut verstanden sind – geschweige denn ihre Fehlfunktionen bei Krankheiten. In dieser Arbeit untersuche ich die grundlegende Biologie menschlicher präsynaptischer Endigungen sowie ihre Dysregulation bei Autismus-Spektrum-Störungen (ASD). Mein Fokus liegt auf einer Proteinfamilie namens RIMs (Rab-interagierende Moleküle), die zentrale Komponenten der präsynaptischen aktiven Zonen darstellen. Ich nutze moderne Technologien mit pluripotenten Stammzellen, um menschliche Neuronen zu erzeugen, CRISPR/Cas9-Genomeditierung zur genetischen Manipulation von Neuronen und zur Erstellung von Krankheitsmodellen sowie fortschrittliche physiologische und mikroskopische Methoden, um die grundlegende Biologie menschlicher präsynaptischer Endigungen sowie ihre Fehlfunktionen bei ASD zu entschlüsseln.Bemerkenswerterweise stellte ich fest, dass die kombinierte genetische Entfernung von RIM1 und RIM2, den beiden Hauptisoformen im Gehirn, menschliche aktive Zonen (AZ) auflöst, das Andocken und die Vorbereitung synaptischer Vesikel verhindert und die Fusion synaptischer Vesikel blockiert – wodurch menschliche präsynaptische Endigungen funktionell stummgeschaltet werden. Genetische Experimente, bei denen entweder RIM1 oder RIM2 selektiv gelöscht wurden, zeigten, dass RIM1 die funktionell dominante Isoform in menschlichen Neuronen ist. Da RIM1 auch ein häufiges Ziel von Mutationen bei autistischen Patienten ist, erzeugte ich eine Reihe von Knock-in-Zelllinien, die alle derzeit beschriebenen ASD-assoziierten Mutationen in RIM1 umfassen, und analysierte systematisch deren Auswirkungen auf die Struktur und Funktion menschlicher Neuronen.

Kommunikation menschlicher Neuronen über zwei konvergierende Mechanismen dysregulieren: entweder durch Beeinträchtigung der Vesikel-Priming oder durch eine gestörte Kopplung von Calciumkanälen an synaptische Vesikel. Dies führt zu einer verstärkten oder reduzierten Informationsübertragung in menschlichen neuronalen Netzwerken und

unterstreicht die entscheidende Rolle einer ausgewogenen Neurotransmission bei der Pathogenese neuropsychiatrischer Erkrankungen.

Meine Arbeit bietet eine einheitliche Sicht auf die grundlegende Biologie menschlicher aktiver Zonen und deren Dysregulation bei Autismus. Meines Wissens stellt sie den ersten Versuch dar, zu verstehen, wie normale menschliche präsynaptische Endigungen funktionieren und wie Gehirnerkrankungen sie beeinflussen. In dieser Hinsicht markiert sie einen wesentlichen Meilenstein für zukünftige Bemühungen zur Entwicklung neuer therapeutischer Strategien, um häufig gestörte präsynaptische Mechanismen bei autistischen Patienten zu korrigieren.

Contents

Abbreviations

AraC……. Cytosineβ-D-arabinofuranoside

ASD..... Autistic Spectrum Disorder

AZ..... Active Zone

ChR……... Channel Rhodopsin

CNV……... Copy Number Variant

dKO……... double Knockout

DIV…… Days in Vitro

ddPCR…….. digital-droplet PCR

EM..... Electron Microscopy

ESCs..... Embryonic Stem Cells

FRAP…… Fluorescence Recovery After Photobleaching

HET……... Heterozygous Knockout

HPF/FS……. High Pressure Freezing/Freeze substitution

ICC…… Immunocito-Fluorescence

IDR…… Intrinsically Disordered Regions

iGluts……. Induced Glutamatergic Neurons

iNs……..... Induced Neurons

GWAS..... Genome Wide Association Studies

LHA……... Left Homology Arm

LLPS……..... Liquid-Liquid Phase Separation

NDD…….. Neurodevelopmental disorders

NSCs……..... Neural stem cells

NPCs…….. Neural precursor cells

PCR……. Polymerase Chain Reaction

Pen/Strep…… Penicillin/ Streptomycin

PFA……. Paraformaldehyde

PEI…….. Polyethylenimine

PSCs..... Pluripotent Stem Cells

PSD..... Post Synaptic Density

qPCR…….. quantitative PCR

RIM..... Rab-Interacting-Molecule

RIMBP..... RIM Binding Protein

RNP…… Ribonucleoprotein

RHA…… Right Homology Arm

SCZ..... Schizophrenia

SFARI..... Simons Foundation Autism Research Initiative

SNV……. Single Nucleotide Variation

VGCC..... Voltage Gated Calcium Channels

WT…… Wild Type

List of Figures

1.Introduction

1.1 Human synapses: basic biology and disease

Mental abilities, at their most fundamental level, depend on communication between neurons in our brains. Communication between neurons occurs at highly specialized structures called synapses. Synapses not only convey information across neural networks but they also compute and process this information, and as such they represent the most fundamental computational unit of the brain. Perhaps not surprisingly, synapses mediate directly or indirectly most if not all brain functions, and thus represent the foundation of all our mental abilities.

Although synapses have been extensively studied in many model organisms such as C. elegans, the fruit fly, and the mouse, very little is known about the principles that control operation of human synapses. This is important because, even though many commonalities across different organism synapses have been found, emerging evidence indicates that human synapses might operate somehow differently [1]. Although the underlying mechanisms are not fully understood, and are currently intensively studied, several factors might contribute to this. First, human-specific genes, which can confer specific properties to human synapses [2]. Second, human specific chromatin regulations, which can control large genetic programs, including those controlling synaptic function [3]. Third, human-specific non-coding regions, commonly known as human accelerated regions (HARs) which, can typically act as enhancers to control human neuron development and function [4, 5]. Fourth, although essential synaptic components have high levels of conservation, there are also differences in amino acid sequences that may play a role in how synaptic communication is finely-tuned, and how mutations in human synaptic proteins underlie pathogenicity [2, 6-8].

Thus, despite enormous progress and the immense insight obtained from model organisms, studies directed to understand the basic biology of human neurons and synapses are urgently demanded. This is particularly crucial when addressing mechanisms of disease, which can be slightly different to what can be inferred from models' organisms. These slight differences, might indeed account at least in part for the lack of efficiency of many therapeutic strategies based on animal models' work. This also indicates that strategies aimed to treat human brain disease must ultimately be validated in a human-cell background.

1.2 Pathology of human synapses

Emerging evidence derived from recent genomic studies in patients, indicate that neurodegenerative, neurodevelopmental, and especially neuropsychiatric diseases are associated with alterations in synaptic function. Neuropsychiatric diseases such as autism spectrum disorder (ASD) and schizophrenia (SCZ) exact a substantial toll, representing nearly 10% of the global burden of disease. This burden extends beyond health implications to encompass significant economic ramifications, with projections indicating a staggering $16 trillion USD burden by 2030 [5]. Despite enormous efforts, current treatments continue to be inefficient, and thus new approaches to treat these devastating diseases are needed.

Studying neuropsychiatric disease and finding more effective therapeutic strategies to treat them has proven very challenging. This is part because these diseases exhibit considerable heterogeneity, with overlapping symptoms that complicate diagnosis. Also, unlike other brain diseases such as Alzheimer's or Parkinson's disease, neuropsychiatric disorders often lack clear pathophysiological markers, making it difficult to elucidate the underlying pathogenic mechanism. Moreover, these disorders are highly heterogeneous with a complex genetic etiology. Neuropsychiatric diseases are highly heritable, but there is no single gene responsible for them. Rather, multiple genes have been identified as contributors to these disorders [9, 10].

Over the past two decades, emerging genomic technologies have facilitated the analysis of genetic data from thousands of individuals with ASD, shedding light on the disorder's genetic landscape (Figure 1). Genome-wide association studies (GWAS) have identified numerous risk alleles with small individual effects that collectively contribute significantly to ASD susceptibility [6]. Concurrently, whole-exome sequencing has revealed a wealth of rare de novo and inherited mutations, particularly in genes involved in neuronal signaling, chromatin remodeling, and synapse formation, underscoring their potential roles in ASD pathogenesis (Figure1, next page) [7, 8].

Given that most cases of ASD are non-syndromic and characterized by an exacerbated enrichment of rare mutations targeting synaptic proteins, its pathogenesis may be understood as an expression of synaptic dysfunction. This suggests that, in the absence of dramatic structural abnormalities in neural circuits or overarching brain development abnormalities, communication between neurons might be impaired. Thus, studying this "synaptic node" presents itself as valuable working frame to uncover common mechanisms that could shape disease pathogenesis and by that identifying targets for therapeutics [11-13].

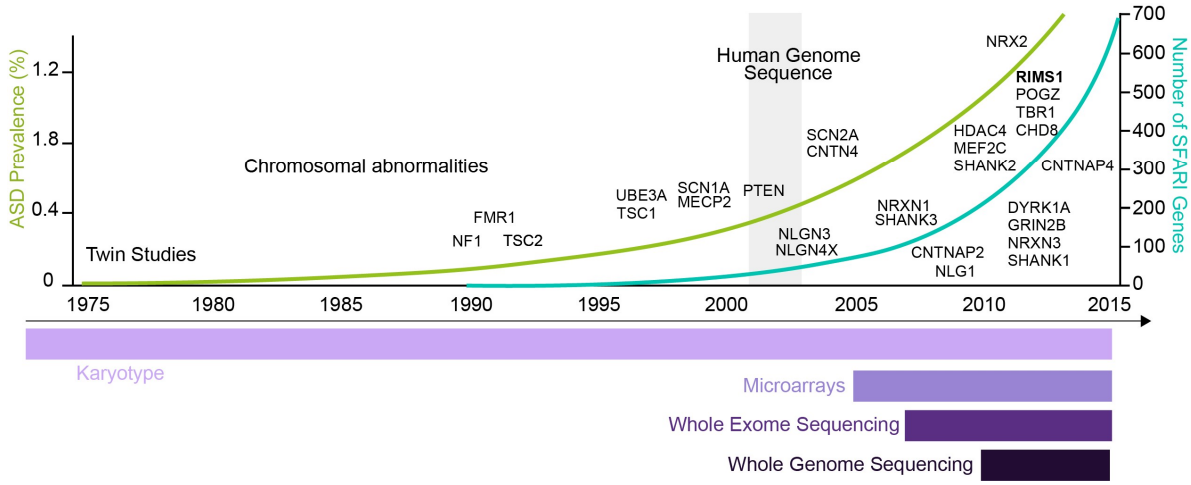

Figure 1 The evolving genetic landscape of ASD over recent decades. The figure presents a timeline summarizing key aspects of ASD research: Upper panel: Prevalence trends and the increasing number of ASD-associated genes cataloged in the SFARI Gene database. Notable scientific milestones and the discovery of relevant genes are highlighted. Lower panel: Advancements in genetic technologies and their corresponding timeframes. Adapted from [14].

However, rigorous investigation of ASD-associated genes presents several challenges. First, the sheer number of implicated genes makes comprehensive multi-gene studies impractical, complicating the identification of convergent mechanisms. Second, multiple ASD-associated variants exist within each gene, potentially contributing differently to pathogenesis and increasing the complexity of analysis. Third, many of these genes have reduced penetrance, limiting their utility in generating robust mouse models. To date, most ASD mouse models focus on syndromic genes, and even these models have yielded limited translational insights into concrete mechanisms and treatments [15, 16].

1.3 Making functional human neurons

A powerful approach to studying ASD-associated genes and mutations has emerged with advancements in stem-cell technologies. Since the discovery of the Yamanaka factors [17], substantial progress has been made in developing fast and reliable protocols for cellular differentiation, de-differentiation, and trans-differentiation [18]. Together, these breakthroughs have enabled the generation of induced pluripotent stem cells (iPSCs) from patient-derived somatic cells and the subsequent differentiation of pluripotent cells into disease-relevant neuronal subtypes [19-23]. Such technological advances provide a virtually unlimited source of human neurons for modeling neurological disorders [24], and have greatly facilitated the assessment of patient-specific neuronal phenotypes, pharmacological interventions, and even genetic rescue experiments [24] [25].

In addition, pluripotent-stem cell technologies have opened up an unprecedented opportunity to study the basic molecular and cellular biology of human neurons and synapses. This is because these models are amenable to genetic engineering, enabling rapid and efficient generation of compound knockout lines in reasonable time-frames [26], which would be impractical in mouse models, for instance. Moreover, the advent of CRISPR/Cas9 genome-editing technologies has further revolutionized the field, allowing for precise correction of patient-derived variants and high-throughput genetic modifications in healthy cells. This approach allows the study of multiple gene variants simultaneously, providing deeper insights into their functional consequences [27].

Thus, the integration of stem cell differentiation technologies with the genome-editing capabilities of CRISPR/Cas9 presents a powerful approach for investigating ASD-associated genetic variants in human synapses. Given the critical role of synapses as functional nodes in ASD pathogenesis, the ability to generate an unlimited supply of genetically modifiable and physiologically relevant human neurons offers a highly versatile and informative system. Combined with deep analysis of synaptic function using modern physiological and microscopy technologies commonly used in rodent studies, this approach holds significant promise for uncovering disease mechanisms and identifying novel therapeutic targets.

1.3 Then, what is a synapse?

As I mentioned in the previous paragraphs, neurons communicate with each other at synapses. Synapses, at the most fundamental level, comprise a “presynaptic compartment” (generally arising from the axon) that releases chemical neurotransmitters, and a “postsynaptic compartment” (generally arising from dendrites), which can sense and respond to released neurotransmitters [28]. These two compartments are positioned in very close proximity to each other, usually less than 30 nm apart [29], forming a physical juncture between them. Indeed, the two membranes are held together by several synaptic cell adhesion protein families (commonly known as synaptic CAMs), which form heterophilic interactions with each other across the synaptic cleft [28].

In addition to this pre-post association via synaptic CAMs, both the pre- and postsynaptic compartments are heavily populated by a distinctive plethora of specialized protein families. On the presynaptic side, there are entire proteins families devoted to organize synaptic vesicle pools (Synapsin, Piccolo/Bassoon, ELKS), to organize the active zone to enable efficient and precise release of synaptic vesicles (VGCC, RIM, RIMBP, Munc13), and also proteins families involved in the fusion reaction itself (Syntaxin, Munc18, Synaptobrevin, SNAP25). On the

postsynaptic side, there are entire families of neurotransmitter receptors (AMPA, NMDA, metabotropic receptors in excitatory synapses), scaffold proteins that organize postsynaptic receptors (PSD95, SHANK, Homer, GRIP, SAPAP), structural actin cytoskeleton components, and signaling proteins that initiate multilevel postsynaptic responses [28]. The high concentration of these proteins at the postsynaptic membrane produces an electron dense area which is clearly visible by electron microscopy and is called the “postsynaptic density” (PSD) [29-32].

1.4 Release needs an Active Zone

At the presynaptic membrane nonetheless, the distribution of proteins is not homogeneous. Indeed, there is an area of particularly high protein concentration where synaptic vesicles fuse and release their content, the neurotransmitter. This area is also electron dense, and is called the presynaptic active zone (AZ, Figure 2). The AZ consist of a network of highly insoluble proteins that interact with each other and with multiple other intracellular proteins. AZs are precisely opposed to PSDs, separated by the presynaptic plasma membrane, the synaptic cleft, and the postsynaptic plasma membrane containing the neurotransmitter receptors [33, 34].

Morphologically, the AZ can be divided into three compartments: the presynaptic plasma membrane, the cytomatrix immediately attached to the membrane, and the electron dense protrusions into the cytoplasm, called “dense projections” [34]. Although this subdivision is morphologically correct, AZs are functional units, and many proteins involved in their architecture do not respect these morphological borders. Active zone components can be divided into two groups.

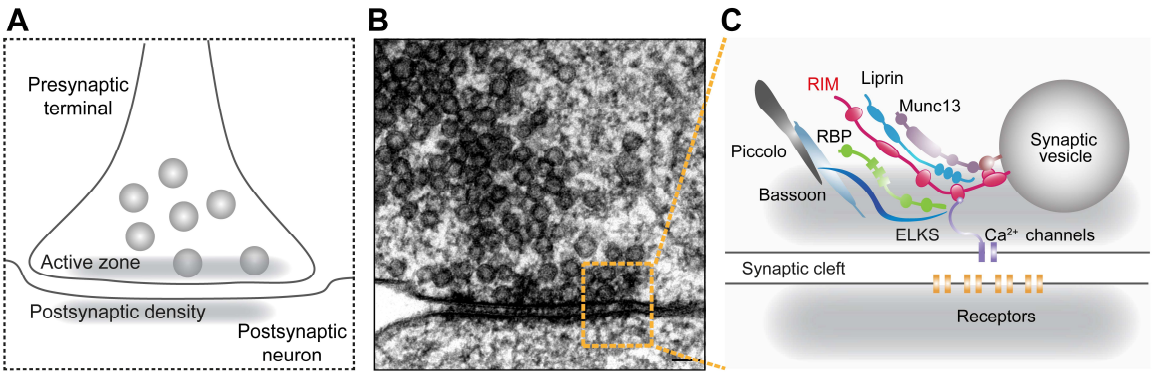

Figure 2 The synapse and the active zone (previous page). A) Schematic of the synapse indicating the presynaptic and postsynaptic compartments. B) Electron microscopy image showing a human synapse. Scale bar = 50nm. C) Schematics of an active zone, depicting key components.

The first group comprises big scaffold proteins that are preferentially enriched at the AZ: RIM, Munc13, RIMBP, ELKS, Bassoon/Piccolo and Liprin-α. And a second group of proteins that can be found at the AZ but are not restricted to it: SNARE proteins and their regulators, channels and receptors, cell adhesion proteins and cytoskeletal proteins [33]).
AZ assembly appears to vary across different synapse types; however, it generally follows a hierarchical organization and has some degree of independence from the post synaptic compartment, i.e. it proceeds in a cell autonomous fashion [35-37]. Furthermore, AZ formation seems to be highly redundant. For instance, studies in mice have shown that single knockouts of key AZ proteins such as RIM, RIMBP, or ELKS result in minimal effects on AZ formation, suggesting a significant level of functional redundancy between these components [38, 39]. In contrast, compound knockouts of RIM and RIMBP, lead to pronounced disruptions in AZ structure, although synaptic transmission is not entirely abolished [40, 41]. Interestingly, Liprin-α levels remain unaffected in these compound knockouts, indicating either its independence from other AZ components or its role as an upstream regulator in the AZ assembly process. Supporting this hypothesis, studies in C. elegans and recent work in human neurons demonstrated that Liprin-α is recruited to the plasma membrane by the synaptic cell adhesion protein neurexin. This recruitment of Liprin-α appears to be a prerequisite for the subsequent assembly of other AZ components.[26, 42]

A key property of several AZ proteins is their ability to undergo liquid-liquid phase separation (LLPS). LLPS is a dynamic process that allows biomolecules to de-mix from the cytoplasm and form distinct, dynamic membrane-less aggregates with dramatically different compositions and properties. It is well-established that the formation of LLPS aggregates is driven by multiple weak interactions, mediated by the intrinsically disordered regions (IDRs) of proteins — segments that do not adopt canonical structural domains and are typically enriched in amino acids such as proline. In the AZ, LLPS may favor the incorporation or concentration of active zone components in a synergistic manner, contributing to the AZ assemble and precise functioning [43]. For instance in C.elegans, deletion of the IDR in the AZ proteins ELKS-1 and SYD2, produced notorious defects in AZ assembly and function [44]. Moreover a recent study shows how different presynaptic compartments segregate through LLPS and allow the transport of synaptic vesicles between a reserved pool and the ready-to-release pool [45]. Importantly, AZ are not randomly distributed within the presynaptic terminal. Instead, they are strategically positioned to maximize the alignment between synaptic vesicle (SV) release sites and neurotransmitter receptors in the postsynaptic membrane [46], presumably enhancing the efficiency of synaptic transmission.

1.5 Rab Interacting Molecules (RIMs)

Rab-Interacting Molecule 1 or RIM1 was discovered in the Südhof laboratory in the late nineties [47]. It was found as a molecule able to bind exclusively to Rab-3, a vesicle GDP-binding protein known to regulate vesicle fusion. They described their localization to the AZs and its ability to enhance exocytosis in a Rab3 dependent manner in PC12 cells [47]. Afterwards, RIM1 has been intensively characterized and it is known to belong to a family that include other 3 different members, RIM2, RIM3 and RIM4. RIM1-4 are encoded by different genes located in different chromosomes and capable of generating multiple transcripts due internal promoters an alternative splicing sites. RIMS1, the gene encoding RIM1, generates a long transcript termed RIM1α, which represents the full version of the protein. This protein consists of at least five clearly identifiable functional domains. Towards the N-terminal region of the protein resides a zinc-finger domain that is surrounded by α-helices, then it possesses a central PDZ-binding domain and finally, towards the C-terminal, two C2 domains. Between these two C2 domains an unstructured proline-rich (PxxP) region is located (Figure 3A). RIM1β, a shorter version of the protein produced by a down-stream promoter, lacks the N-terminus α-helix of the first domain present in RIM1α. Extensive previous work indicates that, in mice, these functional domains perform partly overlapped/partly segregated functions by interacting with different presynaptic partners [34, 48]. The zinc finger at the N-terminus binds to Munc13 to control priming of synaptic vesicles [38]. In contrast, the a-helices that surround the zinc finger bind to Rab proteins (Rab3 and Rab27), presumably to regulate vesicle docking [49]. The central PDZ domain binds to active zone VGCCs, and helps clustering them at the active zone [39]. The function of C2 domains is less understood, though a recent paper indicated that C2B domains, located at the most C-terminus end of RIM1, might mediate binding to Liprins and membrane phospholipids to control fusion downstream of priming and calcium influx [50]. Finally, the proline-rich sequences located in between RIM1 C2 domains bind strongly and selectively to RIM-binding protein (RIMBP), another crucial active zone component that regulates the nanoscale organization of VGCC at the active zone [39, 40, 49]. Thus, RIM1 can directly regulate presynaptic calcium channel clustering via its PDZ domain but also indirectly, via interactions with active zone RBPs (Figure 3B).

1.6 ASD-linked RIM1 mutations: linking active zone dysfunction to disease?

Recent studies, leveraging on whole-genome sequencing, have identified rare mutations in the RIMS1 gene in ASD probands [51-54]. Furthermore, subsequent meta-analyses have

confirmed a significant enrichment of likely deleterious mutations in RIMS1 and other synaptic genes, underscoring their involvement in ASD pathogenesis [55, 56].

Currently RIM1 has been catalogued as a “category 1 gene” according to the Simons Foundations Autism Research Initiative (SFARI) gene database. According to this database this tier corresponds to a high confidence association between the gene and the disorder. RIM1 is also part of the SPARK database list of ASD associated genes. The strength of RIM1 association comes from the several different reports showing ASD patients carrying “likely disruptive” mutations in different locations of the RIM1S gene. Thirteen mono-allelic rare variants are listed in total.

Three of them are intronic variations, and the remaining ten are located in exonic regions. Out of the ten coding variations, three of them are missense variants located in exons 16, 25 and 28 (Figure 3, diamonds). The remaining seven mutations are nonsense or frameshift mutations deemed to produce early stop codons, and located across the gene in exons 2, 5, 6, 20, 21, 23, 24 (Figure 3A, circles).

But is RIM1 the only AZ protein linked to ASD? Clearly not. In addition to RIM1, the SFARI database also lists other AZ proteins. For instance Munc13 and Piccolo are classified as a "strong candidate" for syndromic ASD [57, 58].

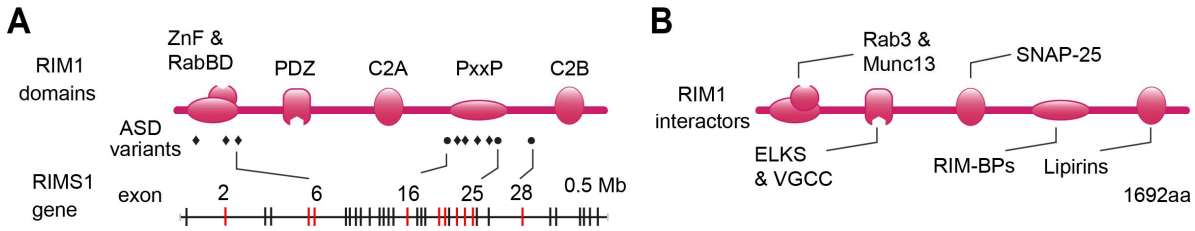

Figure 3. RIM1 domains, ASD linked mutations and interactors. A) Schematics of the RIM1 protein, indicating different functional domains and positions of ASD-linked variants, and RIMS1 gene with exon containing ASD variants are colored red. B) Schematics of RIM1 proteins indicating the partners that interact with the different functional domains.

Furthermore, Cav2.1 is designated as "high confidence" for syndromic ASD, along with its regulatory subunit α2δ [59, 60]. Additional AZ proteins implicated in ASD include RIMBP1 [61], and Liprin-α [53, 61, 62], both classified as "strong candidates". Importantly, most of these proteins not only localize to the active zones, but also represent binding partners of RIM1. This suggests that ASD pathogenesis may not only be rooted in postsynaptic dysfunction [11, 63,

64] but could also be specifically linked to impairments at the AZ. This highlights the AZ as a critical hub whose dysfunction may play a central role in ASD pathogenesis.

2. Motivation and objectives

To date, most efforts devoted to uncovering the mechanisms of ASD pathogenesis have been done in non-human model organisms (typically rodents), commonly using overexpression of mutant transgenes. With the advent of pluripotent stem cells, studies have focused on patient-derived cells, with many using non-isogenic lines as controls, typically analyzing only one or two different mutations per gene. Together, these studies have generated a wealth of valuable insight into the etiology of ASD. But how do we move forward? One potential avenue for advances is to try to find convergent mechanisms of pathogenicity. Ideally, this should be done using a human-neuron background, knocking-in large numbers of pathogenic variants as opposed to relying on overexpression which is prone to artifacts, and analyzing several lines per variant and their corresponding isogenic controls. Finding unifying principles of pathogenesis with such an approach can serve as a base for future studies aiming to tackle these dysfunctions therapeutically. This might be particularly important considering the wealth of genetic data currently available. Literally, hundreds of 'synaptic' variants linked to disease have been identified, but we know very little about how these variants impact synapse function to contribute to disease.

My PhD thesis aims to help fill this gap. Here I focus on a single protein family called RIMs, which represent a central component of the human presynaptic active zone. I first studied the basic biology of RIMs in human synapses. Then, I systematically assessed how a panel of mutations in RIM1, the main RIM isoform in the human brain, impacts their structure and function to contribute to ASD pathogenesis. In doing so, I could directly compare the effects of multiple different ASD variants impacting RIM1, thus allowing me to identify unifying pathogenic mechanisms with potential therapeutic value.

Overarching Goal

The primary objective of this study is to characterize the composition of the human active zone and determine the role of RIM proteins in the basic biology of human synapse and their dysregulation in ASD.

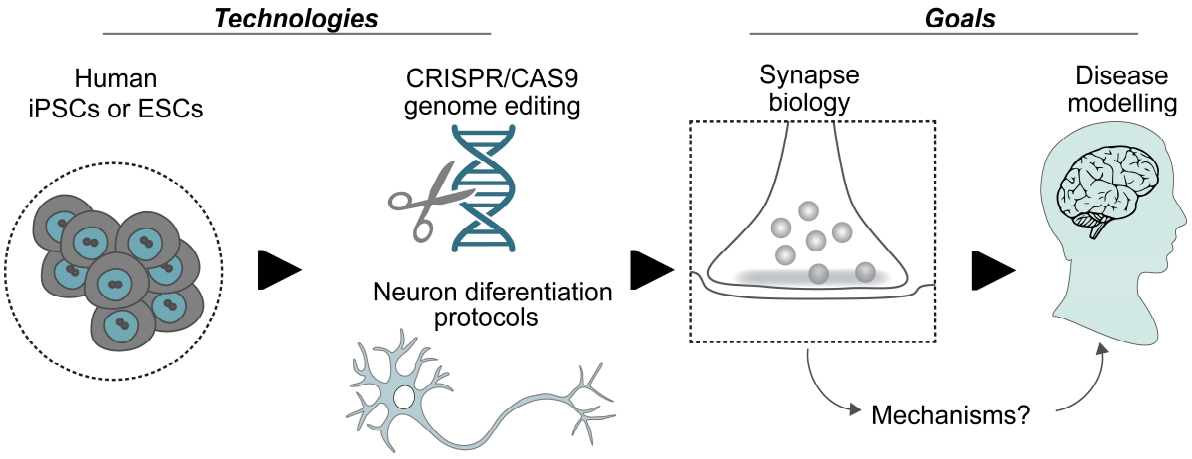

Figure 4. Key technologies and goals of this thesis. Schematics of fundamental technologies used in this thesis to investigate human synapse biology and their dysregulation in disease.

Specific Objectives

To achieve this goal, I propose three independent but inter-related specific aims, as follows.

1. To determine the composition of normal and RIM-depleted human presynaptic terminals. For this, I combine CRISPR/Cas9-based genetic engineering in stem cells primed to develop into human neurons, and assess the structure and function of human synapses combining high-pressure freezing electron microscopy, stimulated emission depletion (STED) super-resolution microscopy, and patch clamp electrophysiology.

2.To generate and validate isogenic control and mutant human PSC lines carrying ASD linked RIM1 variants. I leveraged human pluripotent stem cells (PSCs) and CRISPR/Cas9 technology to knock-in all known coding ASD-linked mutations. This approach allowed me to establish a comprehensive panel of isogenic control (wild-type) and mutant (knock-in) lines. Using recently optimized, highly efficient differentiation protocols, I generated human neurons carrying either wild-type or mutant RIM.

3. To functionally analyze the synaptic composition, structure and physiology of RIM1 ASD linked mutant terminals. To assess the impact on terminals composition and structure, I used confocal, STED and electron microscopy. To assess the impact of ASD-linked RIM1 mutations on synaptic function, I conducted longitudinal multi-electrode array (MEA) recordings and patch-clamp electrophysiology.

3. Results

3.1 Molecular anatomy of human presynaptic active zones

What is the molecular composition of human active zones? To begin addressing this question, I first measured the levels of a panel of AZ proteins previously described in other model organisms, including RIMs. For this, I efficiently and reproducibly generated induced glutamatergic neurons (iGluts) from embryonic stem cells (ESCs) using state-of-the-art, recently published protocols. Specifically, I employed a method designed to yield a predominantly homogeneous population of excitatory neurons resembling glutamatergic forebrain cortical neurons. This approach is straightforward, relying only on two lentiviruses, the growth factors BDNF and NT-3, and the addition of mouse glia to enhance neuronal viability (see Methods, Figure 5A, B) [65].

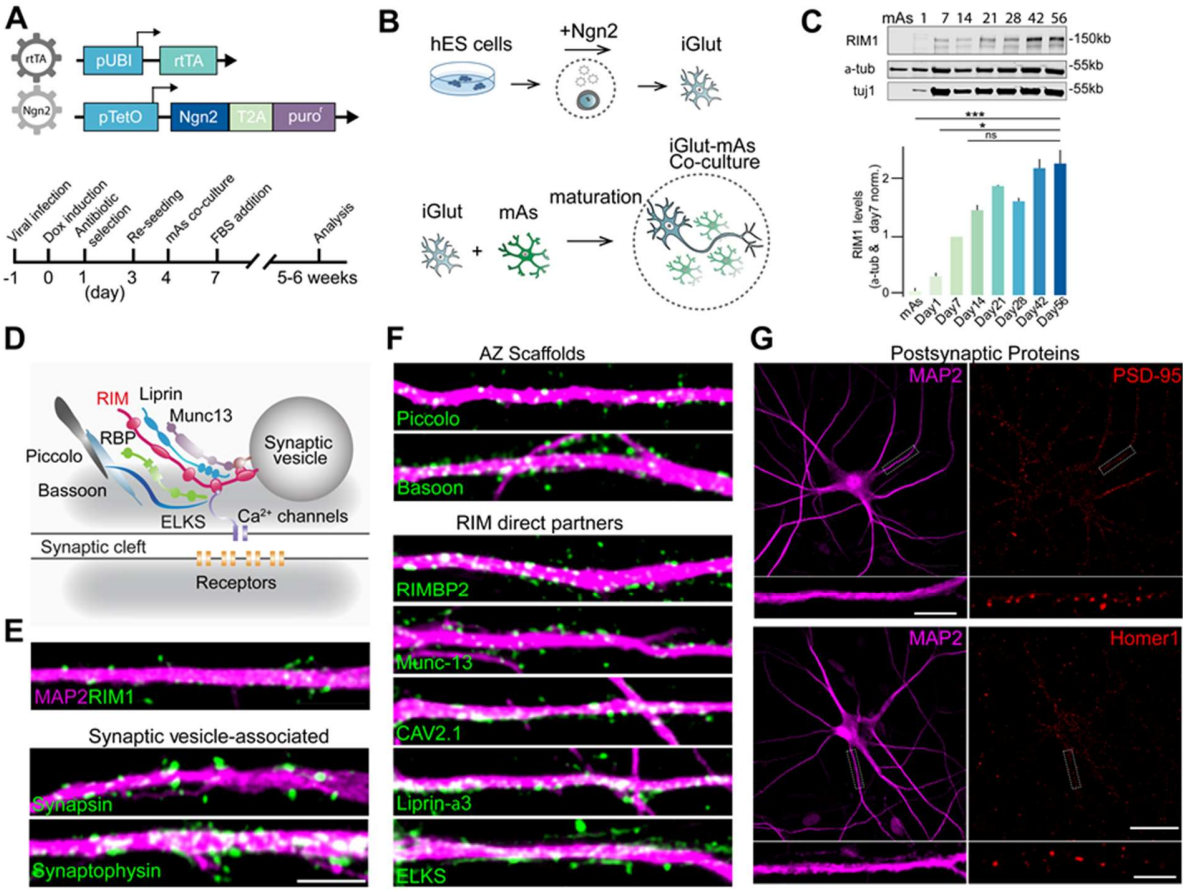

Figure 5. Induced human neurons express RIM1 and key synaptic proteins (previous page). A) Upper panel: schematics of lentivirus constructs used for iGluts generation: Bottom panel: time-line of iGluts production. B) Schematics of iGluts culture generation. C) Time-dependent protein expression of RIM1 in human iGluts. N = 3 cultures, *** $p < 0.001$, * $p < 0.05$, ns = non-significant. D) Schematic of the AZ, showing RIM (red) and its interacting partners on synaptic vesicles, presynaptic membranes, and within the AZ. E-F) Representative confocal images showing the expression of different presynaptic proteins (green) opposed to dendrites stained against the Microtubule Associated Protein 2 (MAP2, magenta). Scale bar = 5 µm. G) Representative confocal images showing the expression of two postsynaptic proteins (red), Postsynaptic Density 95 (PSD-95) and Homer1, on the soma and dendrites delimited by the signal of MAP2 (magenta). Below each low-magnification image, a crop corresponding to the enclose area, is shown. Scale bar full images = 40 µm. Scale bar crops = 5 µm.

Next, I assessed the temporal expression of RIM1, one of central component of the AZ in other model organisms, in human iGluts (Figure 5C). RIM1 protein expression was detectable by day 7 post-induction, progressively increasing until day 42, at which point it appeared to stabilize (Figure 5C). This increment and plateau in RIM1 expression suggested that the iGluts and their synapses mature over time reaching some degree of stability at around 6 weeks *in vitro*. Based on this, I further examined the expression of various synaptic proteins at day 42 using immunocytochemistry.

For this, I first stained iGluts with antibodies against MAP2, a marker of the postsynaptic somatodendritic compartment, which delineated dendrites where presynaptic terminals might establish contact. Immunofluorescence for RIM1 revealed a distinct punctate pattern along the dendrites of iGluts, indicating that RIM1 is localized and concentrated at synaptic sites (Figure 5E). I further examined the expression and localization of additional synaptic proteins using the same approach. iGluts expressed and localized key synaptic vesicle proteins, including Synapsin and Synaptophysin, as well as the large AZ scaffolds Piccolo and Bassoon. Direct interaction partners of RIM1, such as RIMBP, Munc13, Calcium Channel 2.1 (CAV2.1), Liprin-α3, and ELKS, were also expressed and localized along dendrites in a puncta pattern (Figure 5F). Additionally, postsynaptic proteins PSD-95 and Homer-1 were also detected inside the iGlut's dendrites (Figure 5G). These findings collectively suggest that the iGluts form synapses, recruiting all classical major pre- and postsynaptic components previously described in other model organisms.

3.2 RIM, a central component of the human active zone.

Are RIM proteins essential for human AZ function? In addition to enabling the study of human synapses, the use of human pluripotent stem cells (PSCs) provides a powerful advantage: the ability to rapidly generate knockout lines using state-of-the-art gene targeting and gene editing approaches. In the mammalian brain, two main long RIM isoforms are expressed, RIM1 and

RIM2. Thus, I decided to capitalize on CRISPR/Cas9 technology, to remove either RIM1, or RIM2 separately, or to remove them both in a compound double knockout (dKO) line. I designed a simple strategy to knock out RIM genes efficiently by using two single guide RNAs (sgRNAs) to excise an entire exon (Figure 6A).

To knock out RIM1, I targeted PSCs with sgRNAs directed at introns 8 and 9, aiming to remove exon 9—a critical out-of-frame exon common to most RIM1 isoforms (Figure 6A, top). Similarly, to knock out RIM2, I targeted introns 10 and 11 of the RIMS2 gene to delete exon 11, an out-of-frame exon shared by most RIM2 isoforms (Figure 6A, bottom). Following targeting, I screened approximately 386 clones by PCR, and confirmed the loss of the targeted exon by PCR and sequencing.

Successfully edited clones that had lost the targeted exons in both alleles were isolated alongside with unedited clones prime to be used as side by side isogenic controls of the targeted clones. I validated and analyzed at least 2 edited clones and their respective isogenic controls per condition. iGluts derived from RIM1 knockout clones showed a reduced RIM1 protein level when analyzed with a RIM1-specific antibody (Figure 6B). For RIM2 knockout clones, an antibody recognizing both RIM1 and RIM2 was used (as all available antibodies against RIM2 cross-react with RIM1) revealing a ~50% reduction in protein levels in the derived iGluts (Figure 6C). To generate RIM1/2 double knockout (dKO) clones, I re-targeted one of the isolated RIM1 knockout clones using sgRNAs for RIMS2. iGluts derived from these dKO clones showed a nearly complete loss of RIM1/2 protein when analyzed with the RIM1/2 antibody (Figure 6D). These results validated my RIM1, RIM2, and RIM1/2 knock-out lines.

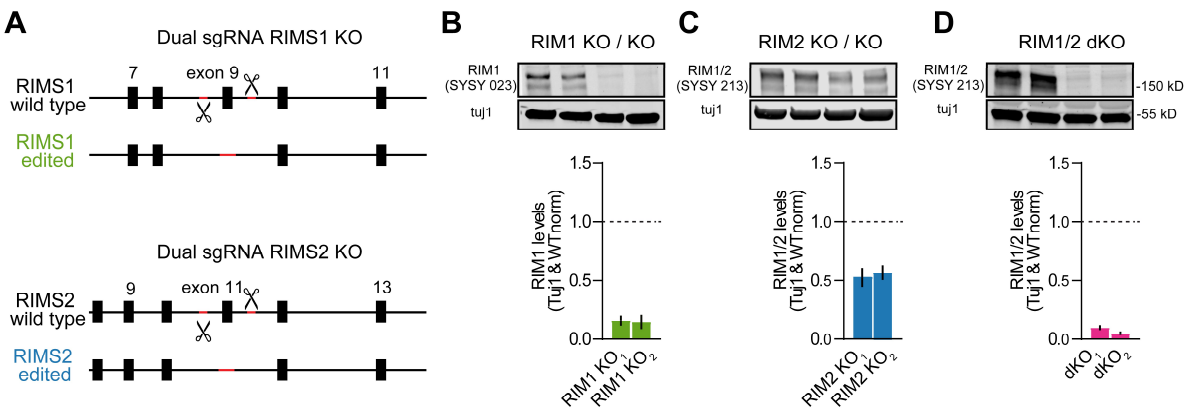

Figure 6 Simple CRISPR/CAS9 targeting strategies to knock out RIM proteins. A) Schematics of targeting strategy to knockout RIM1 (top) or RIM2 (bottom). B-D. Representative blots (top) and quantifications (bottom) of RIM proteins in (B) RIM1 KOs, (C) RIM2 KOs, or (D) RIM1/2 dKOs iGluts.). N=3. Bar plot indicates the mean of the data. Error bars = SEM.

To assess the effects of deletion of RIM1 or RIM2, or their combined deletion on synaptic function, I performed whole-cell voltage-clamp recordings, in the presence of TTX. RIM1 KO iGluts exhibited a pronounced ~60% reduction in the frequency of miniature excitatory postsynaptic currents (mEPSC), while the amplitude and kinetics of the remaining events were unchanged (Figure 7A–C). In contrast, RIM2 KO had virtually no phenotype, although I could observe a small decrease in amplitude which did reach significance. Notably, RIM1/2 double KO led to a synergistic reduction in mEPSC frequency, resulting in >95% decrease, while the amplitude and kinetics of the sparse remaining events remained unchanged (Figure 7G–I).

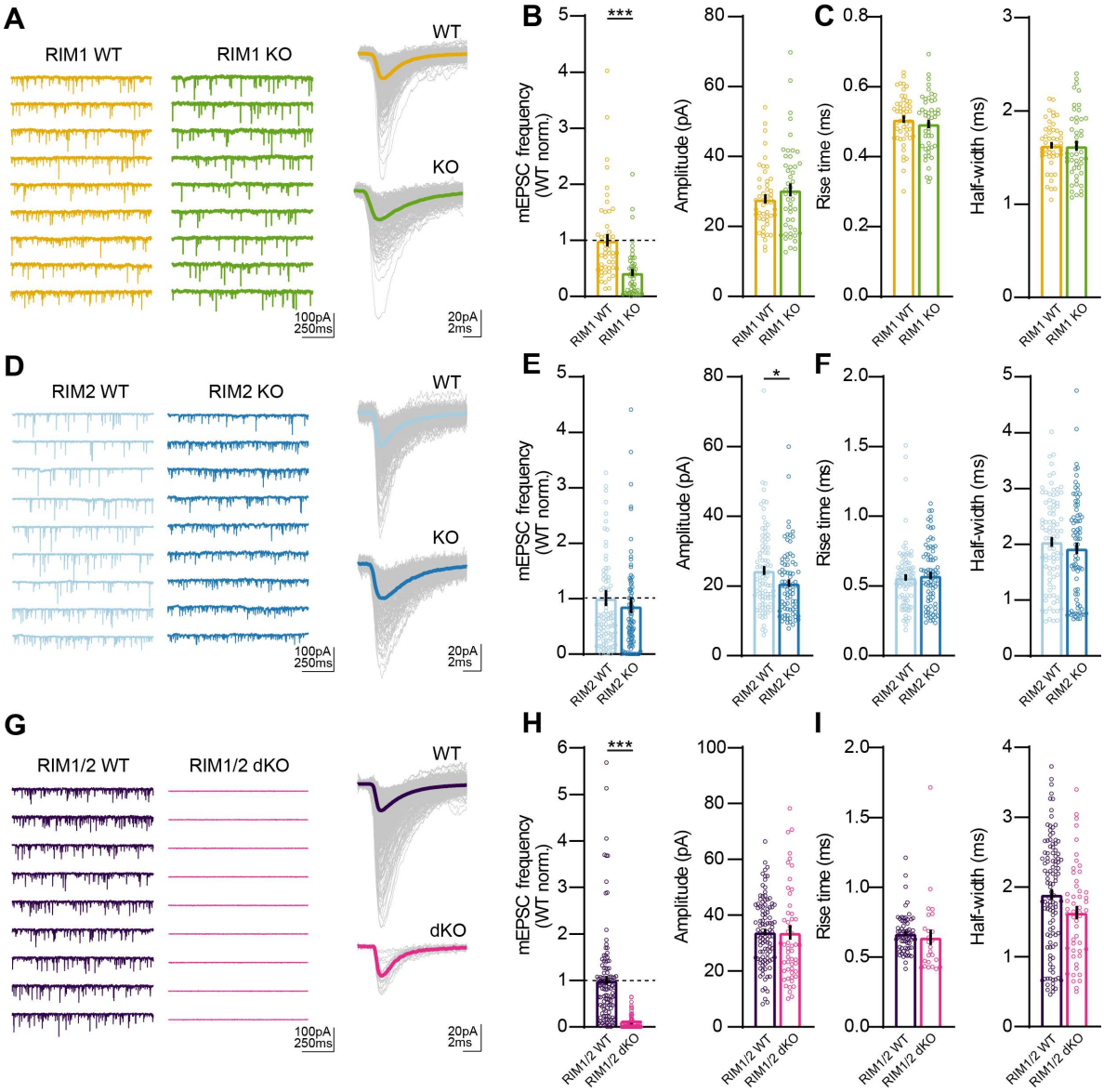

Figure 7 RIM1/2 dKO nearly abolished spontaneous release. A, D, G) mEPSC representative traces (left) and single events (right) for RIM WT and KO iGluts. B, E, H). Quantification of mEPSC frequency and amplitude. C, F, I) Quantification of rise time and half-width. Bar plot indicates the mean of the data. N = 50-90/2-3 (cells/batches). Bar plot indicates the mean of the data. Error bars = SEM. Unpaired t-test. *** p < 0.001, * p < 0.05.

These results allowed me to draw two main conclusions. First, in contrast to other model organisms [66-69], RIMs seem to be particularly essential in human. Second, in human synapses, RIM1 plays a predominant role in maintaining synaptic function, while RIM2 provides partial support that becomes more critical once in the absence of RIM1. This hypothesis is further supported by the observation that the solely RIM1 overexpression in dKO iGluts largely restored the synaptic function (Figure S1).

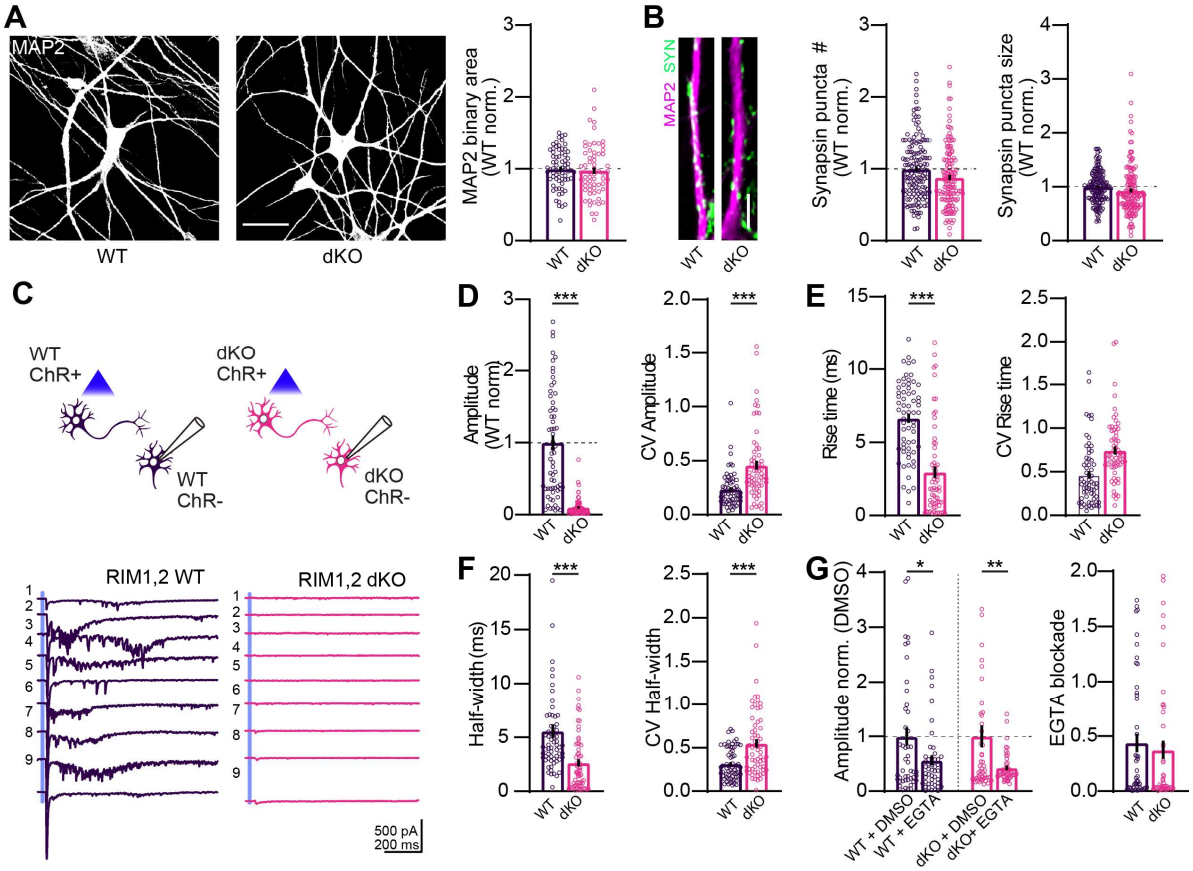

Figure 8. RIM1/2 dKO blocks evoked release. (A) Representative confocal images showing WT and dKO iGluts stained against MAP2 and quantification of MAP2 binary Area. N = 64-70/3 (cells/batches). Scale bar = 50 µm. B) Representative confocal crops showing dendrites of WT and dKO iGluts stained against MAP2 and Synapsin (SYN). Quantification of SYN puncta number and SYN puncta area. N = 146-153/4. C) **Top.** Schematic of the recording configuration. iGluts expressing Channelrhodopsin (ChR) are stimulated by a pulse of blue light while a ChR negative cell is recorded in voltage-clamp configuration. **Bottom**. Representative traces of evoked currents in RIM1/2 WT and RIM1/2 dKO iGluts. D) Quantification of evoked EPSCs amplitude and CV of amplitude. E) Quantification of rise time and CV of rise time, (F) half width and CV of half width. N = 64-63/3 (cells/batches). G) Quantification of evoked events of iGluts incubated with DMSO or EGTA and EGTA blockade. N = 46-48/2 (cells/batches). Bar plots indicate the mean of the data. Error bars = SEM. Unpaired t-test. *** p < 0.001. Part of the recordings (1 batch out of 3) were performed by C. Acuna.

I next investigated whether the pronounced effects on spontaneous release in RIM1/2 dKO iGluts could be attributed to gross alterations in overall development or morphology. To assess this, I measured the total MAP2-positive area covered by dKO iGluts and found no significant differences compared to WT iGluts, indicating normal development with comparable branching and soma size (Figure 8A). Additionally, I examined synapse number by quantifying Synapsin puncta, a classical synaptic marker. While a slight (8%) reduction in puncta number was observed, this decrease was not statistically significant. Puncta area remained unchanged (Figure 8B). Thus, neither gross morphological changes nor synapse development could account for the dramatic decrease in spontaneous release.

To gain further insight into the underlying mechanism triggering these defects, I studied evoked transmitter release. Unlike mEPSC recordings, where action potential firing is suppressed using TTX to isolate release-associated changes, action potential-evoked events can provide deeper insight into underlying biophysical mechanisms impacted by a particular genetic perturbation. For these experiments, I prepared neuronal cultures in which a small subset of iGluts (10%) expressed GFP, while the majority (90%) expressed the engineered channelrhodopsin variant oCHIEF (hereafter referred to as ChR) [70]. I then performed voltage-clamp recordings from GFP-positive, ChR-negative cells to specifically analyze evoked responses elicited by light stimulation (Figure 8C, top).

Evoked EPSC amplitudes were severely reduced, showing > 95% decrease upon deletion of RIM1,2. Additionally, the coefficient of variation (CV) of evoked event amplitude increased significantly, doubling relative to controls (Figure 8D). The CV, calculated as the ratio of the standard deviation to the mean amplitude across multiple stimulation sweeps, serves as a measure of synaptic transmission reliability, which is altered when there are less primed vesicles, or when the VGCC coupling to the release machinery is changed. A higher CV indicates greater variability in response amplitude, suggesting impaired synaptic efficacy and increased trial-to-trial fluctuations in neurotransmitter release [40]. Furthermore, the kinetics of synaptic events was altered in dKO iGluts, with a statistically significant ~50% reduction in both rise time and half-width. I also assessed whether compound RIM1/2 deletion influences the sensitivity of remaining release (<10%) to EGTA. Inside nerve terminals, EGTA acts as a slow calcium chelator, reducing the amount of transmitter released per action potential. The extent of this reduction is proportional to the distance between VGCCs and release sites, as calcium must diffuse from the mouth of the channels to the vesicular calcium sensor to trigger vesicle fusion. Thus, when VGCCs are closely coupled to the release machinery, EGTA has a small

effect compared to when VGCC are physically uncoupled from the release sites [71]. For this, I examined evoked responses under the same experimental conditions as before, but now comparing evoked responses after incubation with either DMSO (as a control) or 100 µM EGTA-AM for 15 minutes at 37 °C. Events amplitude in dKO iGluts showed to have a more pronounced decrease in amplitude when incubated with EGTA, in line with a possible loss of VGCC coupling (Figure 8G left). Nonetheless the difference between the degree of EGTA blockade was not significantly different than in WT iGluts. This might be in part because the residual current upon deletion of RIM1,2 was very small to start with (<1/10 of the original control size), making measurements of EGTA blockade more challenging.

3.3 Genetic removal of RIMs disrupts presynaptic fine structure

Are these dramatic effects on both miniature and evoked synaptic transmission related to actual changes in synapse structure or more specifically AZ composition? To answer this question, I first relied on super resolution STED microscopy. STED allows for quantitative estimations of AZ protein contents with high spatial resolution (Figure 9A, left, middle). Staining iGluts with the postsynaptic marker PSD95 and the presynaptic marker Synaptophysin enabled unequivocal identification of synapses, facilitating the measurement of the signal intensity of a third AZ marker: including RIM, Munc13, RIMBP2, CAV2.1, ELKS, and Liprin-α3. Thus, I imaged synapse-rich areas and analyzed intensity profiles of "side-view" synapses, defined as those where PSD-95 appeared elongated and was flanked on one side by Synaptophysin (Figure 9A, B). Intensity measurements were performed along a rectangle centered at the peak of the PSD-95 signal, measuring 1.2 × 0.2 µm (Figure 9A right, C left). Using this approach, I compared AZ composition in RIM1/2 WT and dKO iGluts. DKO iGluts show a dramatic decrease in RIM signals, as expected, confirming that these synapses are virtually devoid of RIM (Figure 9C, I). Then, I also observed a clear and significant decrease in Munc13 signal of around 70% (Figure 9, H), and partial decreases in the signals of RIMBP2 and CAV2.1 was also observed (Figure 9 E, F). In contrast, the levels of ELKS remain unchanged (Figure 9E, F, K, L), while Liprin-α significantly increased by about 50% (Figure 9H, I, M, N). Thus, deletion of RIMs dramatically affects the integrity of human presynaptic active zones.

To address whether these changes in AZ composition may affect the fine-scale ultrastructure of the synapses as a whole, I switched to electron microscopy (EM). I utilized high-pressure freezing/freeze substitution (HPF/FS) as the sample preparation method [72] .Compared to traditional fixation methods for EM, HPF/FS provides superior sample preservation while significantly reducing the appearance of artifacts. This is particularly important when examining

synapses where structure may be distorted or miss localized. RIM1/2 dKO iGluts showed seemingly normal pre- and postsynaptic compartments with evident postsynaptic densities and similar number of synaptic vesicles (SV) pools (Figure 10A, C).

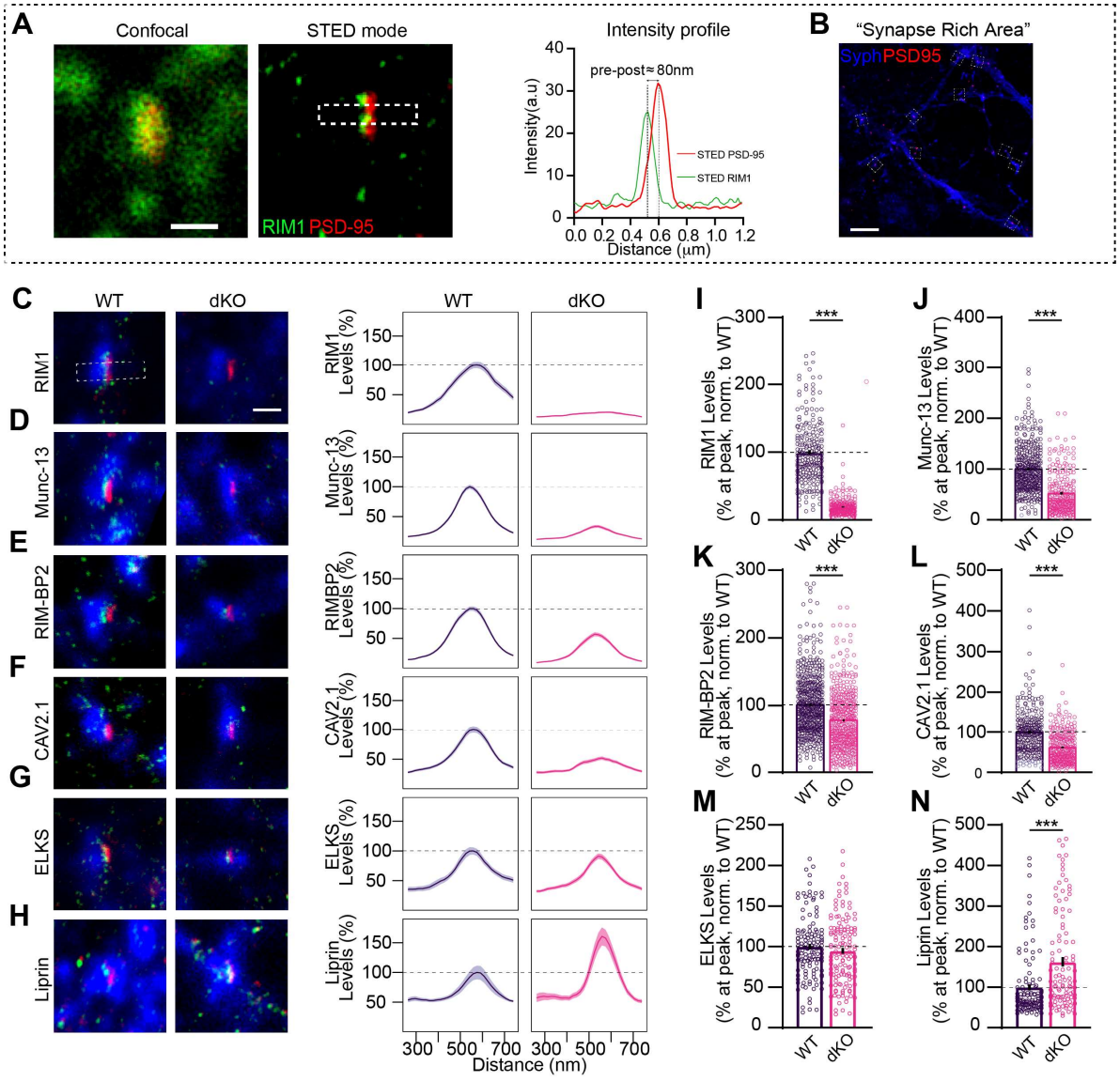

Figure 9. RIM1/2 dKO disrupts the AZ. A) Representative images of the same synaptic profile imaged in confocal and STED mode (Left). Florescence intensity profile over the rectangle on the STED image (Right). B) Low magnification STED image of a synapse rich area indicating several profiles (squares).C-H) Representative STED images of RIM1/2 WT and dKO synapses, with labeling for PSD-95 (red), Synaptophysin (blue), and the AZ markers (green): RIM1 (C), Munc13 (D), RIMBP2 (E), CAV.2.1 (F), ELKS (G), Liprin (H) follow by average fluorescence intensity profiles of each respective marker. I-N) Quantification of peak intensity for RIM1 (I), Munc13 (J), RIMBP2 (K), CAV.2.1 (L), ELKS (M), and Liprin (N) signals in WT and dKO iGluts. N = 107-360/2-3 (profiles/batches). Bar plots indicate the mean of the data. Error bars = SEM. Unpaired t-test. *** $p < 0.001$.

Remarkably I found that RIM1,2 dKO were nearly devoid of docked synaptic vesicles (SVs) (Figure 10A, C). These are vesicles that appear in close contact (<2 nm or touching the AZ membrane) to the AZ membrane, which are usually called docked synaptic vesicles, and that likely represent a large fraction of primed synaptic vesicles that form the readily releasable pool. In addition, vesicles within 30nm (a fraction of which would form the RRP) to the AZ were also significantly decreased, but the total amount of SVs in the terminals showed no difference. Interestingly a small increase in the size of the SVs was noted while the length of the PSD remained unchanged (Figure 10 C, E).

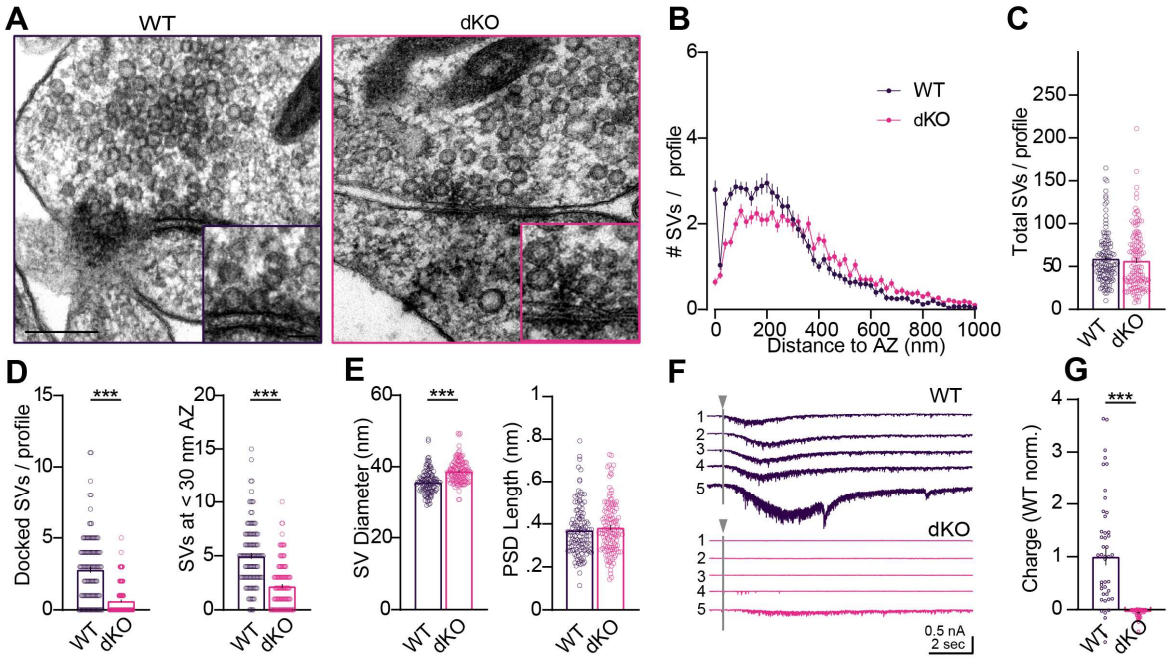

Figure 10. RIM1/2 dKO dramatically reduces vesicle docking and the size of the RRP. A) Representative transmission electron microscope images of high-pressure frozen RIM1/2 WT and dKO synapses. Scale bars: 200 nm in main panels; 50 nm in insets. B) Quantification of: number SVs as function of distance to the AZ, (C) total number SVs, (D) docked SVs and SVs within 30 nm of the AZ, (E) SV diameter and PSD length. N = 118-129/2 (profiles/batches. F) Representative sucrose evoked current traces. G) Quantification of sucrose evoked total charge. N = 22-24/2 (cells/batches). Bar plots indicate the mean of the data. Error bars = SEM. Unpaired t-test. *** $p < 0.001$.

In order to confirm that these dramatic structural defects reflect a near elimination of primed synaptic vesicles, we evaluated the response of RIM1/2 dKO to hypertonic sucrose application. In these experiments, cells are patched and held at near -70 mV holding potentials in voltage clamp, while a low resistance pipette containing a 0.5M sucrose solution is positioned in close proximity (~100 μm) to them. Then, cells are challenged with this hypertonic sucrose solution

for 5 secs, which promotes release of all vesicles in very close proximity to the AZ membrane (the RRP of vesicles), by mechanical distortion [73]. Thus, the extent of release is proportional to the size of the RRP. In accordance with what I observed in the EM experiments, I found that dKO iGluts showed a tremendous reduction in the total charge evoke by the sucrose puff, reinforcing the idea that RIM proteins are crucial for the docking and priming of the SVs to the AZ membrane in human synapses (Figure 10F, G). Given the surprising and substantial reduction in docked SVs, I sought to confirm this observation made in normal thin-sections (70 nm), by employing this time electron tomography of thick sections (250 nm). I reconstructed three WT and two dKO synapse tomograms and manually segmented them (Figure S2A, B, C). The reduction in docked SVs was also evident with this technique. Although the remaining SV distribution appeared similar and the size of the SVs did not differ between dKO and WT synapses (Figures S2G, F, H).

These results indicate that deletion of RIMs have a particularly prominent effect in human neurons, more pronounced than what has been found in other model organisms such as mice, C. elegans, or fly [66-69]. Can this be linked to the actual differentiation protocol I used? To address this concern, I assessed the impact of RIM1,2 deletions after using a different differentiation protocol, a protocol based on the gradual conversion of PSCs into neural stem cells, and then guiding their maturation into neurons with growth factors (Figure S3). In these dKO neurons, RIM1/2 proteins were absent, as expected, but synapse number remained normal (Figure S3B, C). Similar to Ngn-2 based differentiation, removal of Rim from these neurons dramatically changed the AZ composition and the mEPSC frequency (Figure S3, F-N), indicating that at large, the dramatic RIM1/2 dKO phenotype in human induced neurons is independent of the differentiation method used.

Taken together, these results indicate that RIM proteins are central component of the human active zone. This role of RIMs seems to mainly relay mainly on RIM1 but not on RIM2. Mechanistically, RIMs do not affect the gross morphology of neurons and number of synapses, but instead is essential for the assembly of the AZ because in their absence, the levels of Munc13, RIMBP2 and CAV2.1 are dramatically reduced. These AZ defects translate into a near complete elimination of the readily-releasable pool of vesicles, and which in turn block spontaneous and evoked transmitter release from human nerve terminals.

3.4 A panel of PSCs carrying ASD-linked variants

In the previous section, I have shown that RIM proteins, and in particular RIM1, play a crucial role in human AZs, which extends even further than what has been observed before. Remarkably, recent large-scale genomic studies in autistic patients have identified RIM1 prominent target of variants linked to this disease. This further suggests that RIM1 dysfunction, and thus AZ dysfunction, might contribute to ASD pathogenesis with high-penetrance. But would these pathogenic variants, which affect only RIM1, and actually even only one allele of RIM1, render any structural and physiological phenotype in human neurons?

To assess the impact of ASD-linked mutations in RIM1, I first generated a panel of stem-cell lines carrying each of the 10 coding RIM1 variants associated with autism spectrum disorder identified to date (Figure 12A). To achieve this, I utilized the highly efficient CRISPR/Cas9 system, which enables precise cutting near the target genomic sites, thereby increasing the likelihood of introducing the desired mutation, using a single-stranded DNA oligo that contains the intended mutation, as a donor template (Figure 11A, B). I carried this out with a simple pipeline targeting each mutation with the same approach. I transfected wild type H1 ESCs with RNP-Cas9/sgRNA complexes and an ssDNA donor that contain the intended mutation in each case. After the transfection I split the cells and seeded them as single cells (Figure 11B).

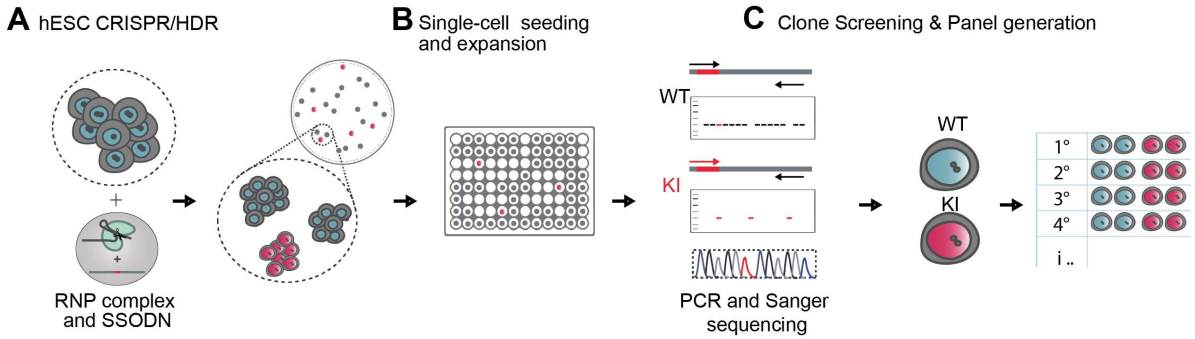

Figure 11. Generation of a panel of ESC lines carrying ASD-linked RIM1 variants. A) Stem-cells are transfected with a ribonucleoprotein (RNP) complex, consisting of purified Cas9 protein complexed with a synthetic single guide RNA, and a single-stranded DNA oligo. B) Transfected cells are then seeded as single cells into petri dishes. Individual colonies are picked and transferred to 96-well plates for expansion and DNA extraction. DNA extracted from the 96-well plates are screened by PCR using primers specific to both mutant and wild-type alleles. Sanger sequencing is then performed to confirm the precise insertion of mutations, and validated clones are selected to establish the isogenic panel. WT, wild type.KI, knock-in. RNP, ribonucleoprotein complex. ssODN, single-stranded oligo DNA.

After a week, these cells form colonies that I transferred to 96-well plates from where I extracted DNA in order to perform a PCR screening to identify correctly targeted clones and their isogenic wild types controls (Figure 11C). I developed a tailored targeting strategy for each mutation,

which are located in exons 2, 5, 6, 16, 20, 21, 23, 25, and 28 of the RIMS1 gene (Figures 12B and S4).

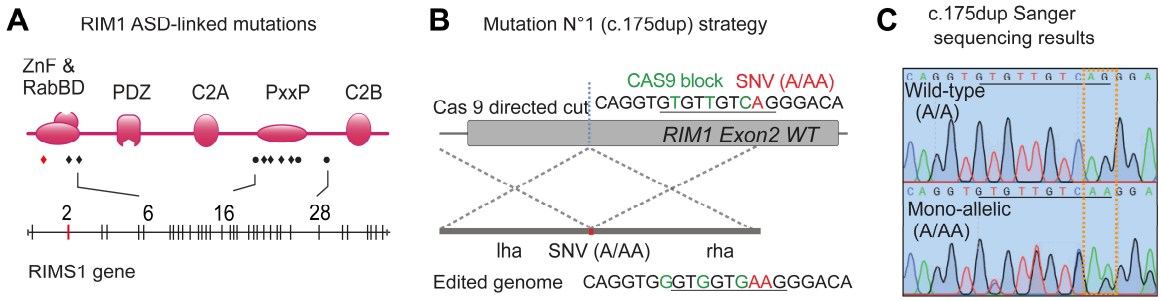

Figure 12. Typical targeting strategy to generate lines carrying a ASD-linked RIM1 variant. A) Schematic of the RIM1 protein and gene, highlighting functional domains and exon locations. The positions of ASD-linked mutations are marked by diamonds for missense mutations and circles for nonsense mutations. The red diamond denotes Mutation #1, as detailed in panel B. B) Targeting strategy for introducing Mutation #1, designed to insert an additional "A" in exon 2 of RIM1. Cas9 blocking mutations are shown in green, and the intended mutation is highlighted in red. C) Chromatogram showing sequencing results for wild-type and knock-in clones at the targeted RIM1 exon 2 regions. The precise location of the intended mutation is marked by an orange rectangle. SNV, Single Nucleotide Variant; lha, left homology arm; rha, right homology arm.

Clones were first screened using PCR, and putative knock-in clones were further validated by Sanger sequencing. An example is shown in Figure 12. Wild-type clones displayed clean, distinctive sequences which aligned precisely with both the reference genome and the parental line sequences. In contrast, the selected knock-in heterozygous clones exhibited mixed peaks specifically at the target sites, where either Cas9 blocking mutations or ASD-linked mutations were introduced (Figures 12C & S4).

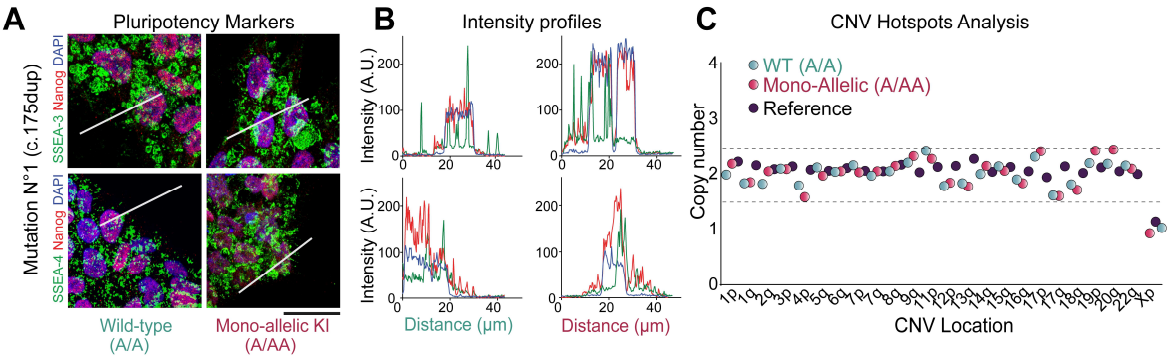

Figure 13. Validation of knock-in lines. A) Confocal images showing mutation N°1 wild type and knock-in PSCs colonies stained for 3 different canonical pluripotency markers. Nanog (Red), SSEA-3 (Green, upper panels) and SSEA-4 (green, lower panels). Additionally, nuclei were stained with DAPI. Scale bar = 60 µm. B) Intensity profiles for each micrograph from A measured along the white lines. C) CNV analysis results from a wild type and a knock-in clone for RIM1 ASD-linked mutation N° 1 over 24 loci.

After targeting all 10 mutations I screened in total 3774 colonies. Out of these, 58 clones were selected either as isogenic wild type (WT from now on) or heterozygous knock-in (KI, from now on) clones, which comprise my panel of RIM1 ASD linked mutations (Table 2.1).

Table 1. Summary of all knock-in lines generated for my PhD thesis project.

N°	Exon	Allele	Residue	Screened	Generated
1	2	c.175dup	Arg59Fs	192	2WT/2KI
2	5	c.586dup	Thr196Fs	480	3WT/3KI
3	6	c.981C>G	Tyr327Ter	384	2WT/2KI
4	16	c.2708G>A	Arg903Gln	288	2WT/2KI
5	20	c.3139del	Thr1047Fs	384	2WT/2KI
6	21	c.3264C>A	Cys1088Ter	576	2WT/2KI
7	23	c.3430C>T	Arg1144Ter	480	2WT/2KI
8	24	c.3522_23del	Gln1174Fs	192	2WT/2KI
9	25	c.3577A>G	Arg1193Gly	384	2WT/2KI
10	28	c.4045G>T	Ala1349Ser	384	3WT/3KI
		Total clones		**3774**	**58**

For each variant, I generated and analyzed at least two pairs of isogenic clones (named WT1/KI1 and WT2/KI2, respectively). Moreover, for at least one pair of clones per variant, I evaluated the quality and genome integrity of the lines after targeting, aiming to minimize potential off-target genetic aberrations that might impact my analysis. specifically, I measured the levels of three canonical pluripotency markers characteristic of healthy pluripotent stem cells, and quantified copy number variation (CNV) profiles at key hotspots commonly associated with variation in human pluripotent stem cells across nearly all chromosomes (Figures 13A, B, C & S5) [74].

3.5 Impact of ASD-linked RIM1 variants on protein levels

After validating the lines, I started the analysis. As an initial step, I decided to assess whether the introduction of these pathogenic variants affect RIM1 expression, or protein levels in human neurons. Thus, I generated iGluts from the targeted clones and performed western blot and qPCR experiments. As anticipated based on the nature of these variants (none-sense, frameshifts, missense), some of these variants significantly reduced RIM1 protein levels in the KI clones compared to their isogenic WT controls. Specifically, the mutations Arg59Fs (exon 2), Thr196Fs (exon 5), Tyr327Ter (exon 6), Thr1047Fs (exon 20), Cys1088 (exon 21), Arg1144Ter (exon 23), and Gln1174Fs (exon 24) (Figure 14B, C) resulted in 40–60% decreases in RIM1 protein levels, all statistically significant. In contrast, the mutations Arg903Gln (exon 16), Arg1193Gly (exon 25), and Ala1349Ser (exon 28) did not lead to significant changes in RIM1 protein levels (Figure 14B, C). A similar trend was observed at the mRNA level. QPCR analyses revealed that nonsense and frameshift mutations caused a

significant reduction in RIM1 mRNA levels, whereas missense mutations did not affect mRNA expression (Figure 14D).

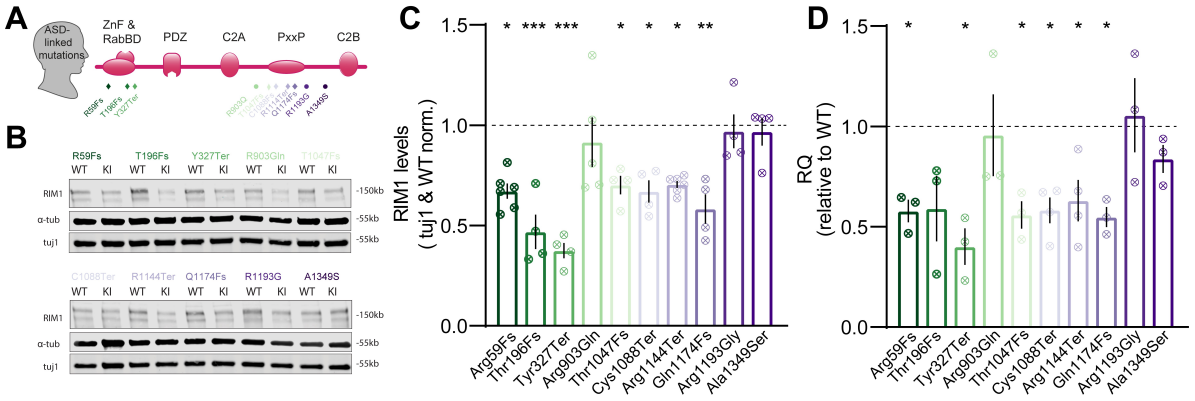

Figure 14. Effect of ASD-linked RIM1 variants on protein levels. A) RIM1 protein schematic indicating functional domains and location of ASD-linked mutations. In diamonds, nonsense mutations, in circles, missense mutations are shown. B) Representative blot showing protein expression of RIM1, α-tub (α-tubulin) and tuj1 in WT (wild type) and KI (knock in) iGluts. C) Quantification of RIM1 protein levels of KI iGluts compared to their isogenic WT controls. D) Quantification of RIM1 mRNA levels of KI iGluts compared to their isogenic WT controls. N = 3-6 cultures. Bar plots indicate the mean of the data. Error bars = SEM. Unpaired t-test. * $p < 0.5$, ** $p < 0.01$, *** < 0.001.

3.6 Impact of ASD-linked RIM1 variants on human neuron activity

Do changes in RIM1 dosage have functional consequences? Do mutations that do not alter RIM1 protein levels produce any effect on human neuron function?

To address these questions in a robust and efficient manner, I employed multi-electrode array (MEA) recordings. iGluts carrying each mutation were seeded onto proprietary 48-well MEA plates, which support normal neuronal maturation, provide high spatial resolution with 16 electrodes per well, and enable recordings in a controlled environment without exposing the cells, allowing for longitudinal analyses (Figure 15A, B). Control iGluts, derived from non-targeted ESCs and cultured on these plates, exhibited increasing levels of electrical activity over time. By 20 days in vitro (DIV), all electrodes within a well detected spikes, although the overall spike rate remained relatively low. By 30 DIV, spike counts increased substantially, plateauing around 60 DIV (Figure 15B).

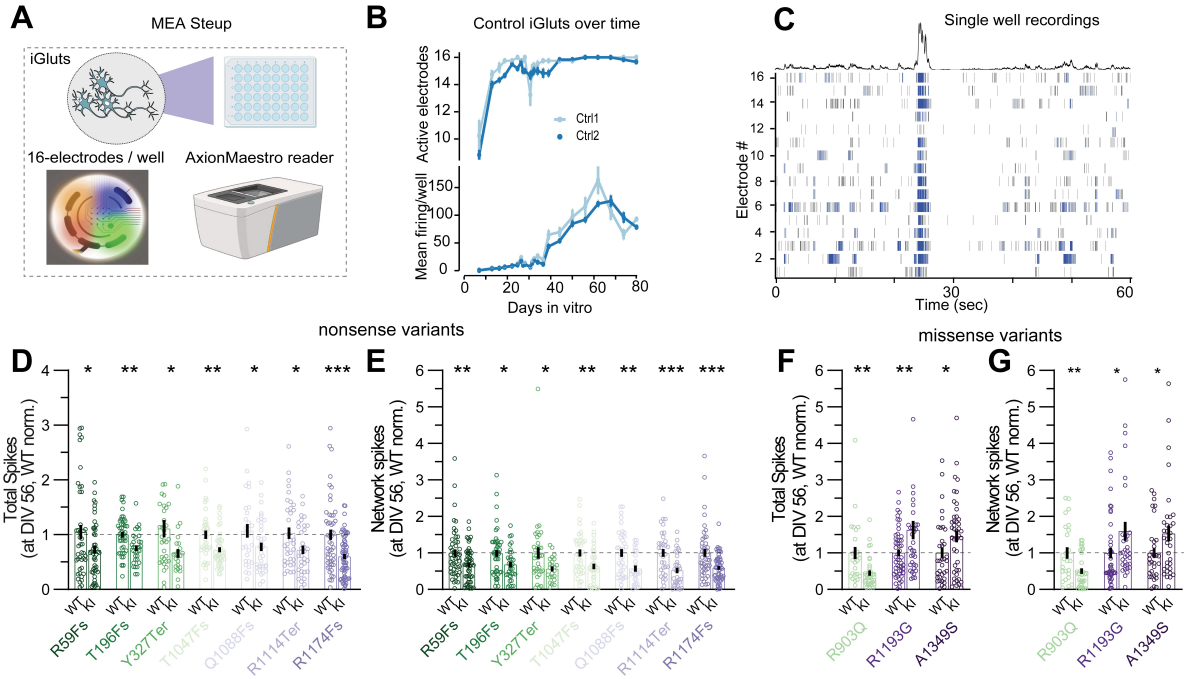

Figure 15. Impact of ASD-linked RIM1 variants on overall human neural activity. A) Experimental approach used for Multi-Electrode Array (MEA) recordings of human neural activity. iGluts were seeded in 48-well MEA plates, with each well consisting of 16 electrodes. Activity was measured at different time points (longitudinally) in a plate reader without affecting the cells viability and development. B) Exemplary traces of 2 groups of wild-type iGluts recorded over 80 days, indicating number of active electrodes (top), and the mean firing rate per well over time. C) Exemplary recordings from all 16 electrodes of a typical well at DIV50. Vertical lines (black) indicate the timing of single spikes. Vertical lines (blue) indicate the occurrence of "network" spikes. D) Summary of the total number of spikes or (E) network spikes recorded during 10 minutes in WT and KI neurons for nonsense variants, or (F, G) missense variants. N = 28-67/2-4 (wells/batches). Bar plots indicate the mean of the data. Error bars = SEM. Unpaired t-test * p < 0.5, ** p < 0.01, *** < 0.001. MEA recordings were performed by Jana F. Tegethoff.

Analysis of iGluts carrying nonsense mutations, which resulted in decreased RIM1 levels, revealed a consistent reduction in activity. This was evident as a 20–40% decrease in the total number of detected spikes per recording, which was statistically significant for all mutations by DIV 56 (Figure 15D). Similarly, a more pronounced reduction in network activity (defined as spikes temporally synchronized across more than four electrodes within the same well within a 10-ms interval, see Figure 15C) was observed in iGluts carrying nonsense mutations, with reductions of approximately 25–50% (Figure 15E). In contrast, missense mutations exhibited divergent effects. The R903Q mutation led to a 40–50% reduction in both total and network activity, resembling the decrease observed in iGluts carrying nonsense mutations. However, iGluts carrying the R1193G and A1349S mutations displayed the opposite phenotype, with both total and network activity increasing by nearly 100% at DIV 56 (Figure 15F, G).

Taken together, systematic MEA-based analysis of all ASD-link RIM1 variants support their contribution to ASD pathogenesis. But what are the underlying mechanisms? This is the

question I will address in the next sections. To facilitate the analysis, I analyzed nonsense variants separately from missense variants.

3.7 Synaptic aberrations triggered by nonsense variants

In this section, I will focus on nonsense variants, followed by an analysis of missense mutations later. To determine whether nonsense mutations impact iGluts morphology or synapse development, I analyzed MAP2 binary area and Synapsin puncta number in iGluts carrying nonsense mutations using immunocytochemistry and confocal imaging. Overall, mutant iGluts did not exhibit significant changes in the MAP2 area. While minor variations were observed—such as a decrease for mutations T1047Fs and Q1088Fs and an increase for R1114Ter—these differences were not statistically significant (Figure 16A, B). Similarly, neither Synapsin puncta number nor Synapsin puncta size showed more than slight variability, and these changes were also not statistically significant (Figure 16C, D).

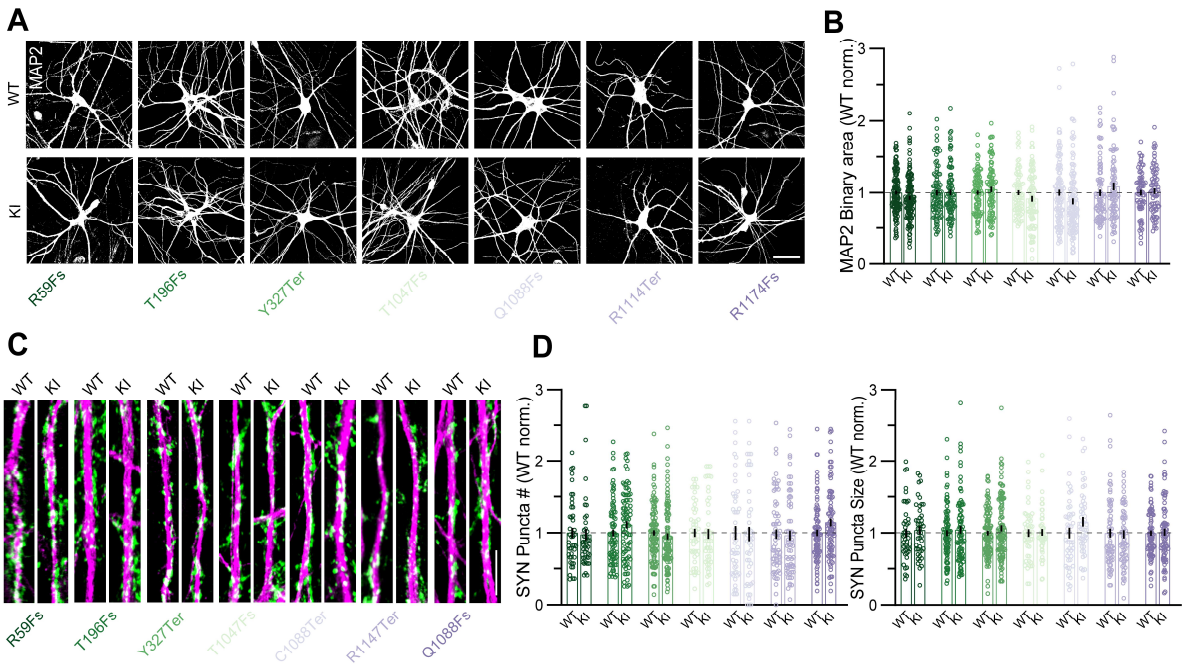

Figure 16. Nonsense variants effects on neuronal morphology and synapse numbers. A) Representative confocal images showing WT (up) and KI (bottom) iGluts stained against MAP2 for every RIM1 ASD-linked nonsense variant. B) Quantification of MAP2 binary Area. N = 68-136/2-4 (cells/batches). Scale bar = 50 µm. C) Representative crops showing dendrites of WT and KI iGluts from nonsense variants. Scale bar 5 µm. D) Quantification of Synapsin puncta number and Synapsin puncta size for nonsense variants. N = 44-108/2-3 (images /batches). Bar plots indicate the mean of the data. Error bars = SEM.

To confirm and gain a deeper understanding of the physiological effects of the RIM1 ASD-linked nonsense mutations, I systematically performed patch-clamp recordings of iGluts

carrying each of these mutations and their respective isogenic controls. Specifically, I recorded spontaneous miniature synaptic currents in the presence of 0.5 µm TTX, to suppress action potentials. Remarkably, I observed a significant decrease in mEPSC frequency in all clones carrying nonsense mutations (Figure 17 A, B, C). These results are consistent with and confirm the findings observed in the MEA experiments. Moreover, a clear pattern is confirmed in which all nonsense mutations exhibit decreased synaptic activity pointing to defects in synaptic release. Taken together these data suggest that all nonsense variants are mildly affecting RIM1 protein levels, and that it's enough to produce a physiological phenotype (loss of function). This nonetheless is not accompanied by any gross morphological changes or by a decrease in the synapse number.

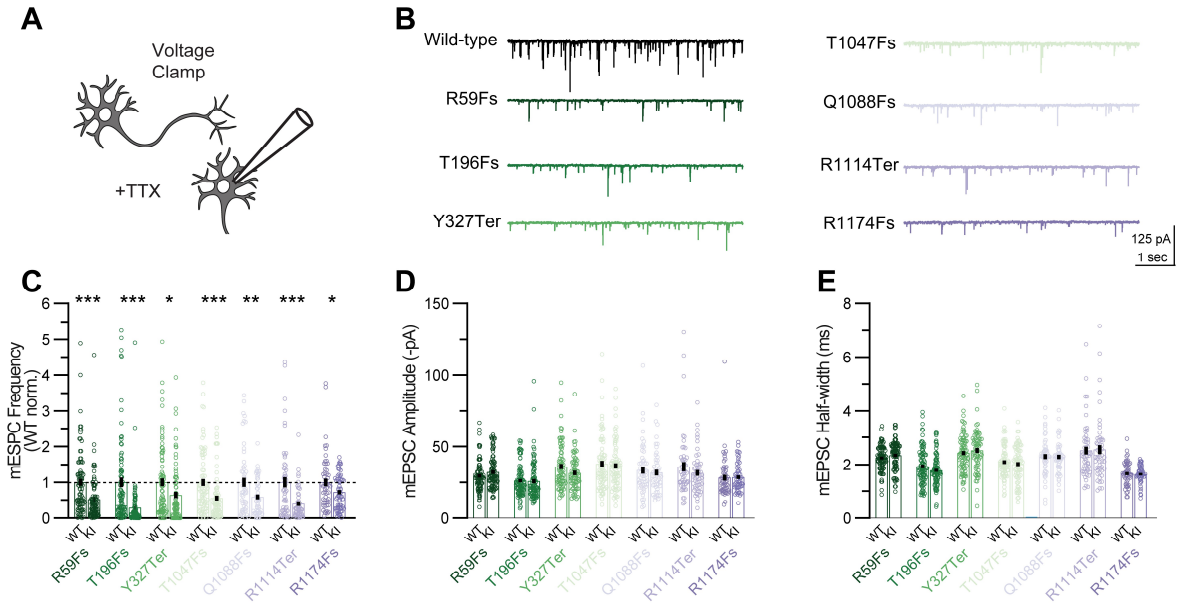

Figure 17. Nonsense variants effects on miniature release. A) Schematic representing voltage clamp recordings, miniature events corresponding to spontaneous release from terminal are recorded from an individual iGlut. B) Representative mEPSC recordings from control neurons (wild-type, WT), and from all nonsense variants linked to ASD. (C) Quantification of the miniature events frequency for WT and KI iGluts, (D) amplitude and (E) half-width. N =54-104 (cells/2-4 batches). Bar plots indicate the mean of the data. Error bars = SEM. Unpaired t-test * $p < 0.5$, ** $p < 0.01$, *** < 0.001.

3.8 Mono-allelic loss of RIM1 mimics release impairments of nonsense variants

Considering that all nonsense mutations showed a similar decrease in RIM1 protein levels (approximately 50%) and exhibited phenotypic synaptic functional effects in the same direction and of similar magnitude, I reasoned that these mutations likely impact the function of human synapses by a common underlying mechanism, which is triggered by the ~50% protein loss, as it would occur upon RIM1 heterozygous knockout. This also suggested that the underlying

mechanism by which all nonsense variant trigger synaptic aberrations, could be studied in heterozygous knockout lines, without the need of analyzing all lines carrying nonsense variants, which would not be practical. Thus, I generated new heterozygous KO ESC lines using the same approach used to generate the full KO of RIM1. From this targeting round, I instead isolated RIM1 heterozygous knockout (from now on HETs) PSCs lines for further analysis (Figure 18A).

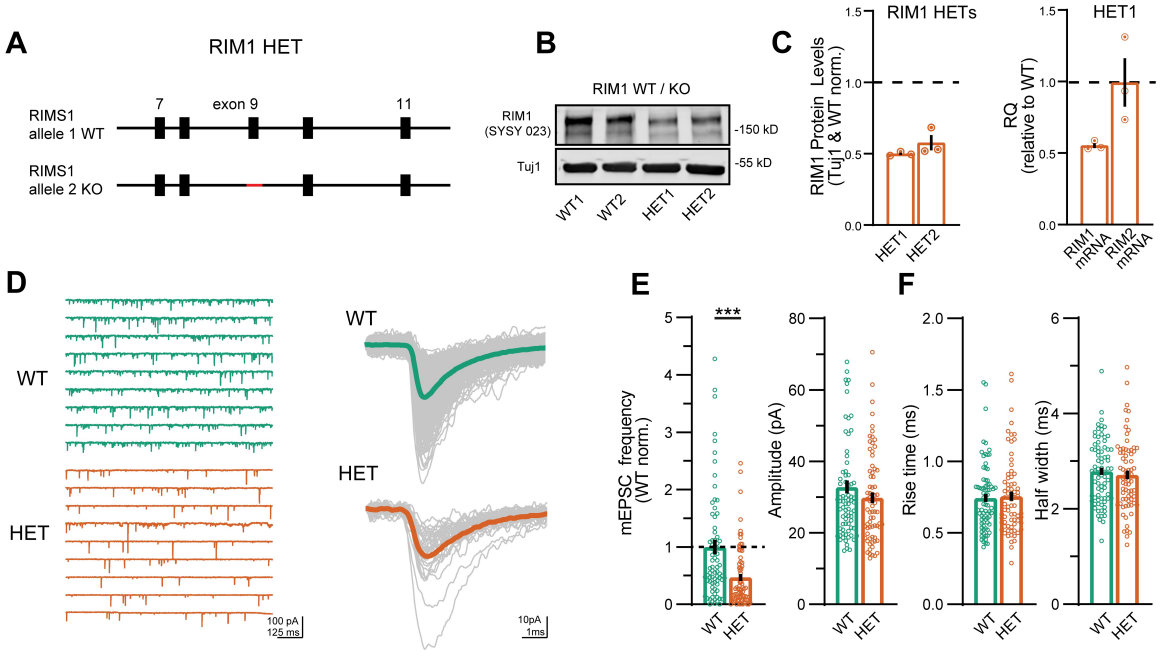

Figure 18. RIM1 heterozygous knock-out iGluts show reduced miniature release. A) Schematics of HET cells alleles at RIM1 locus. B) Representative western blot against RIM1 of two different wild type clones and two different RIM1 HET clones derived iGluts samples along with RIM1 protein levels quantification. C) RIM1 and RIM2 mRNA levels in HET1 clone derived iGluts. D) mEPSC representative traces (**left)** and single events averaged trace **(right)** for RIM1 WT and HET iGluts. E) Quantification of miniature event frequency and amplitude. F) Quantification of mEPSC rise time and half width. N = 78/3 (cells/batches). Bar plots indicate the mean of the data. Error bars = SEM. Unpaired t-test. *** < 0.001.

As expected, RIM1 HET iGluts showed a 50% decrease in RIM1 protein levels, as determined by western blot using the specific antibody against RIM1 (Figure 18B, C). This decrease was accompanied by a 50% reduction in RIM1 mRNA levels, while RIM2 mRNA levels remained unaffected (Figure 18C) thus mimicking the profile of nonsense mutations. Analysis of mEPSC of HET iGluts revealed a significant reduction in the frequency of about 50%, similar to the effects seen in nonsense mutations, while amplitude and kinetics of the individual events were not affected (Figure 18D, F, G).

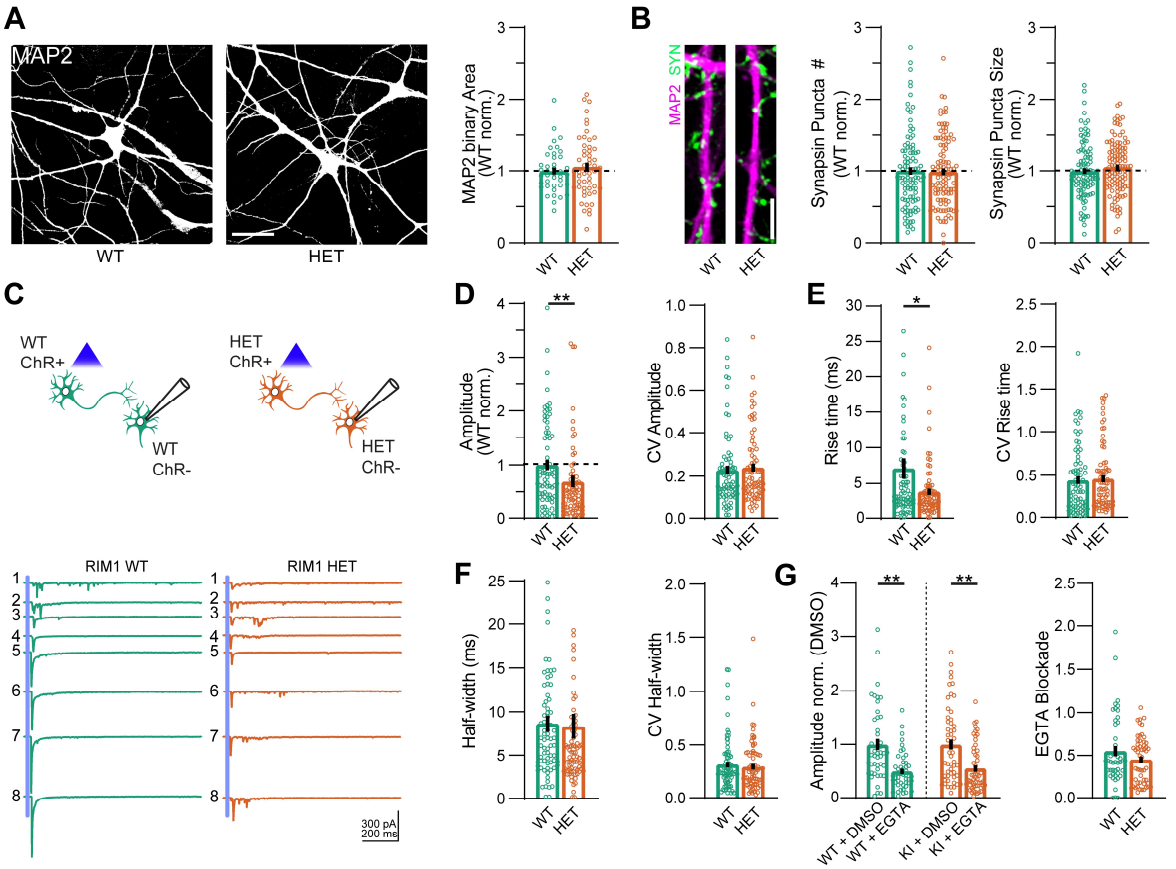

Figure 19. RIM1 heterozygous knock-out decreases evoked events amplitude. A) Representative confocal images showing WT and HET iGluts stained against MAP2 and quantification of MAP2 binary Area. N = 40-52/3 (cells/batches). Scale bar = 50 µm. B) Representative confocal crops showing dendrites of WT and HET iGluts stained against MAP2 and Synapsin (SYN). Quantification of SYN puncta number and SYN puncta area. N = 100-110/3 (images/batches). C) **Top**. Schematic representing the recording configuration. iGluts expressing Channel Rhodopsin are stimulated by a pulse of blue light while a ChR negative cell is recorded in voltage clamp configuration. **Bottom**. Representative traces of evoked currents in RIM1/2 WT and RIM1/2 HET iGluts. D-F) Quantification of (D) evoked EPSC amplitude and CV of amplitude, (E) rise time and CV of rise time, (F) half width and CV of half width. N = 64-63/3 (cells/batches). G) Quantification evoked EPSC amplitude after DMSO or EGTA incubation and EGTA blockade. N= 45-54/3 (cell/batches). Bar plots indicate the mean of the data. Error bars = SEM. Unpaired t-test. *** p < 0.001. ** p < 0.01. * p < 0.05

Gross somatodendritic morphology and synapse number was also not affected, again in line with what I observed in the iGluts carrying nonsense mutations (Figure 19A, B), nonetheless evoked events amplitude along with rise time was significantly reduced by around 40 and 50% respectively (Figure 19C, D). Interestingly no significant difference was observed in the CV of amplitude, rise time, half-width, and in the EGTA sensitivity (Figure 19G).

3.9 RIM1 heterozygous knock-out partly disrupts AZ, and synaptic vesicle docking/priming

HET iGluts exhibited structural changes at the active zone measured by STED microscopy. As expected, a decrease in RIM1 protein levels was noticeable at synapses; although small, this reduction was statistically significant (Figure 20A, G). Additionally, Munc13 levels were also diminished. A slight but non-significant decrease was observed in ELKS, while no changes were detected in RIMBP2, CAV2.1, or Liprins (Figure 20B–L).

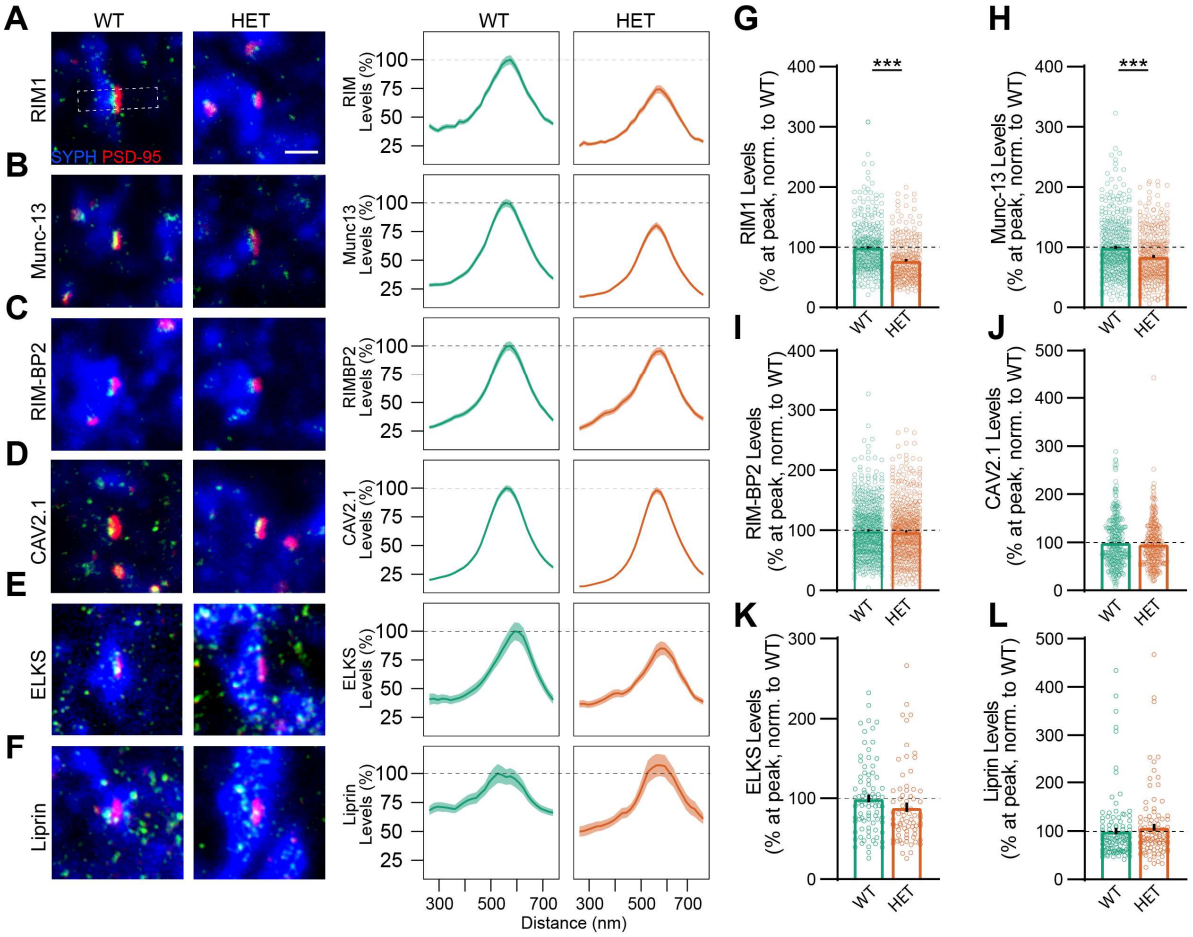

Figure 20. RIM1 heterozygous knock-out altered AZ composition. A-F) Representative STED images of WT and HET synapses, with labeling for PSD-95 (red), Synaptophysin (blue), and the AZ markers (green): (A) RIM1, (B) Munc13, (C) RIMBP2, (D) CAV.2.1, (E) ELKS and (F) Liprin followed by average fluorescence intensity profiles of each respective marker. I-N) Quantification of peak intensity for (I) RIM1, (J) Munc13, (K) RIMBP2, (L) CAV.2.1, (M) ELKS, and (N) Liprin signals. N = 72-334/2-3 (profiles/batches). Bar plots indicate the mean of the data. Error bars = SEM. Unpaired t-test. *** $p < 0.001$.

When examining HET synapses under the electron microscope, they appeared largely normal compared to WT synapses, containing SVs and a clearly distinguishable PSD (Figure 21A, B).

Although the overall distribution of vesicles was similar between WT and HET synaptic profiles (Figure 21B, C), a detailed analysis revealed a consistent and significant decrease in the number of docked vesicles and in the number of vesicles located within 30 nm of the AZ membrane (Figure 21D). No differences were observed in the size of the SVs or the length of the PSD (Figure 21E). Finally, the responses to hypertonic sucrose application were significantly reduced in HET lines (Figure 21F, G).

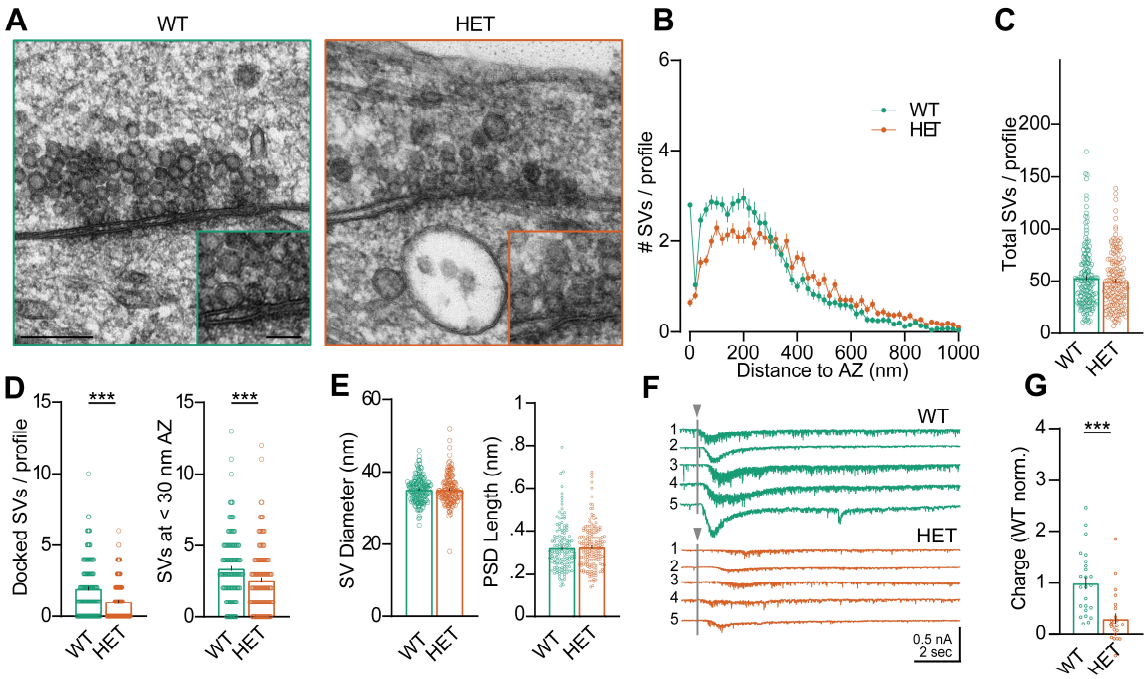

Figure 21. heterozygous knock-out reduces vesicle docking and priming. A) Representative electron microscope images of high-pressure frozen RIM1 WT and HET iGluts. Scale bars: 200 nm in main panels; 50 nm in insets. B) Quantification of: number SVs as function of distance to the AZ, (C) total number SVs, (D) docked SVs and SVs within 30 nm of the AZ, (E) SV diameter and PSD length. N = 151-164/3 (profiles/batches). F) Representative sucrose evoked current traces. (G) Quantification of sucrose evoked total charge. N = 24/2 (cells/batches. Bar plots indicate the mean of the data. Error bars = SEM. Unpaired t-test. *** $p < 0.001$.

Taken together, these results indicate that a ~50% reduction in the levels of RIM1 at the AZ, (as it occurs in the heterozygous RIM1 mutants I just described above or in the lines carrying missense ASD-link RIM1 variants I discussed before) is sufficient to impair synaptic communication between human neurons. Mechanistically, this impairment is due to a partial disassembly of the presynaptic AZ, which prevents normal docking and priming of synaptic vesicles for release, resulting in near 50% reduction in synaptic transmission between neurons in human neural networks.

3.10 Mechanisms underlying synaptic aberrations triggered by missense variants.

In contrast to the nonsense variants I just described, the 3 missense variants studied rendered divergent phenotypes on MEA recordings (Figure 15). What are the underlying mechanisms responsible for these changes? To address this question, I first performed patch-clamp recordings of miniature activity in isogenic control and knock-in lines (Figure 22).

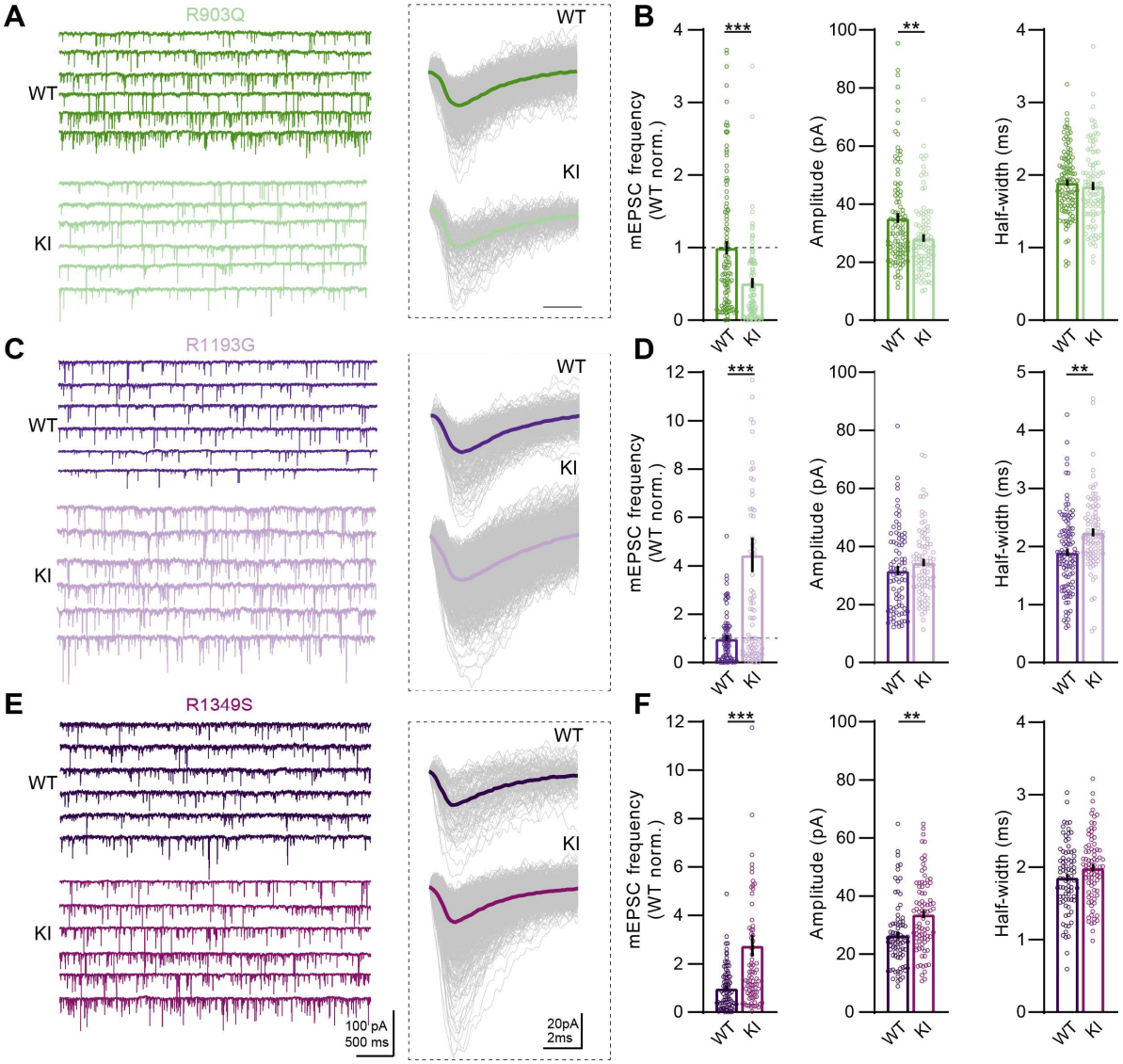

Figure 22. ASD-linked missense RIM1 variants exhibit divergent changes in miniature release. A-E) mEPSC representative traces (**left**) and single events averaged traces (**right**) for RIM1 WT and RIM1 of iGluts missense mutations (A) R903Q, (C) R1193G and (E) A1349S. B, D, F) Quantification of mEPSC frequency, amplitude and half width. N = 50/ 2 (cells/batches). Bar plot indicates the mean of the data. Error bars = SEM. Unpaired t-test. *** $p < 0.001$, ** $p < 0.01$.

These experiments showed a ~50% decrease in mEPSC frequency in iGluts carrying the R903Q mutation, whereas mutations R1193G and A1349S led to a four- and two-fold increase in mEPSC frequency, respectively (Figure 22A–F). These findings are consistent with observations from MEA experiments (See Figure 15). Importantly, these differences were not due to gross morphological changes or due to changes in synapse numbers, because neither of them was significantly altered for any of these variants (Figure 23A, B).

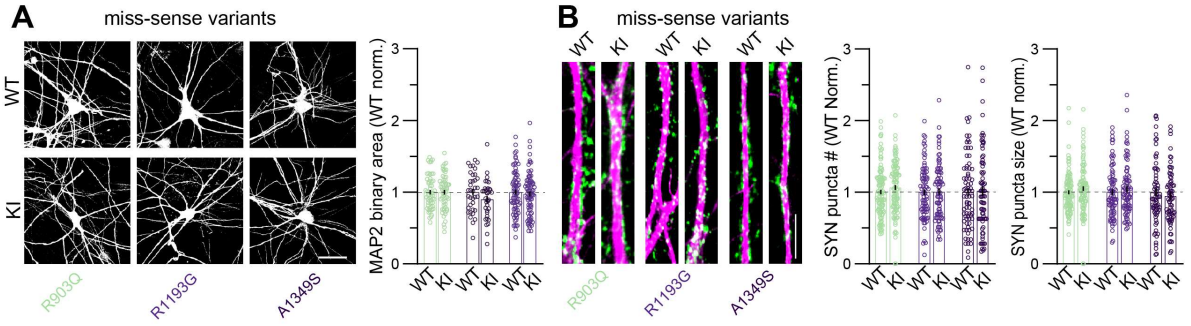

Figure 23. ASD linked missense RIM1 variants exhibit normal morphology and synapse number. A) Representative confocal images showing WT (**top**) and KI (**bottom**) iGluts stained against MAP2 for every RIM1 ASD-linked missense variant and quantification of MAP2 binary Area. N = 36-78/2-3 (cells/batches). Scale bar = 50 µm. B) Representative crops showing dendrites of WT and KI iGluts from missense variants and quantification of Synapsin puncta number and Synapsin puncta size. N = 104-1110/3 (images /batches). Scale bar 5 µm Bar plots indicate the mean of the data. Error bars = SEM.

Remarkably, the analysis of active zone composition using STED, revealed small but significant changes in synapses carrying the R903Q mutation. Specifically, a modest but significant decrease in RIM1, Munc13, and RIMBP2 levels was observed, while CAV2.1 remained unchanged (Figure 24 A, D, G). In contrast, the R1193G and A1349S mutations did not affect the levels of any of these AZ proteins (Figure 24B, C, E, I). Together, these results suggest that while the loss-of-function effect of the R903Q variant could be explained by partial disassembly of the active AZ, the gain of function effects of the R1193G and A1349S variants could not.

To gain deeper insight into the potential underlying mechanism mediating this, I again turned to patch clamp electrophysiology and studied in more detail evoked synaptic transmission. Consistent with the MEA and mEPSC results presented previously, the R903 mutation decreased amplitude of evoked events, accompanied by an increase in the CV of amplitude. EGTA sensitivity did not significantly change (Figure 25A-E). Conversely, the mutations R1193G and A1349S exhibited the opposite phenotype. Both mutations led to a considerable increase in evoked event amplitude and a significant increase in half-width, consistent with a

stronger synaptic connection. Additionally, R1193G showed a slight reduction in the CV of rise time, while A1349S displayed minor reductions in the CV of amplitude and half-width (Figure 26A-D, F-I).

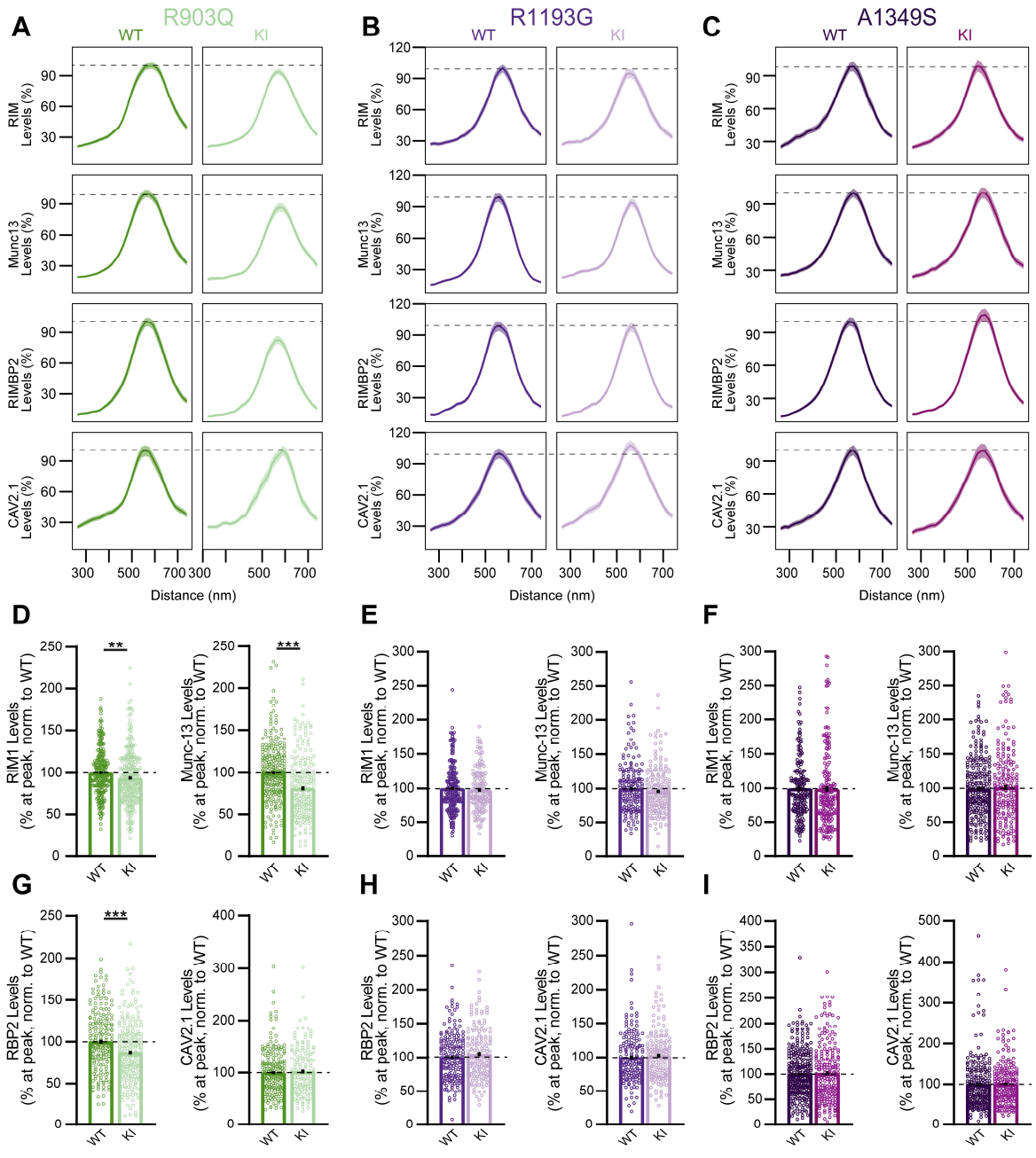

Figure 24. Subtle active zone composition changes in R903Q knock-in iGluts. STED fluorescence intensity profiles for RIM1, Munc-13, RIMBP2 and CAV2.1 RIM1 WT and KI iGluts from miss –sense mutations R903Q (A), R1193G (B) and A1349S (C). Quantification of peak levels of RIM and Munc13 (D, E, F). Quantification of peak levels of RBP2 and CAV2.1 (G, H, I). N = 166-300/2 (cells/batches). Bar plots indicate the mean of the data. Error bars = SEM. Unpaired t-test. *** $p < 0.001$. ** $p < 0.01$.

Interestingly for both R1193G and A1349S variants EGTA sensitivity was almost completely abolished. Altogether, these experiments indicate that phenotypes observed in R1193G and A1349S mutants, can indeed be explained by changes in coupling of VGCC to calcium sensors. In stark contrast, phenotypes triggered by R903 cannot be explained by such a mechanism.

In a major effort to further dissect the mechanisms of synaptic aberrations triggered by the missense variants, I performed EM and sucrose experiments in neurons carrying these missense variants. Overall, I found the ultrastructure of these synapses was rather normal, and could not detect difference in the total number of SVs, docked SVs, SVs size or PSD length were found for mutation R903Q (Figure S6 A-E), R1193G and A1349S (Figure S7 A-E, H-L). In line with these EM results, sucrose puffing experiments also did not reveal any significant difference in any of the three mutations (Figure S6 F, G & Figure S7F, G, M. N).

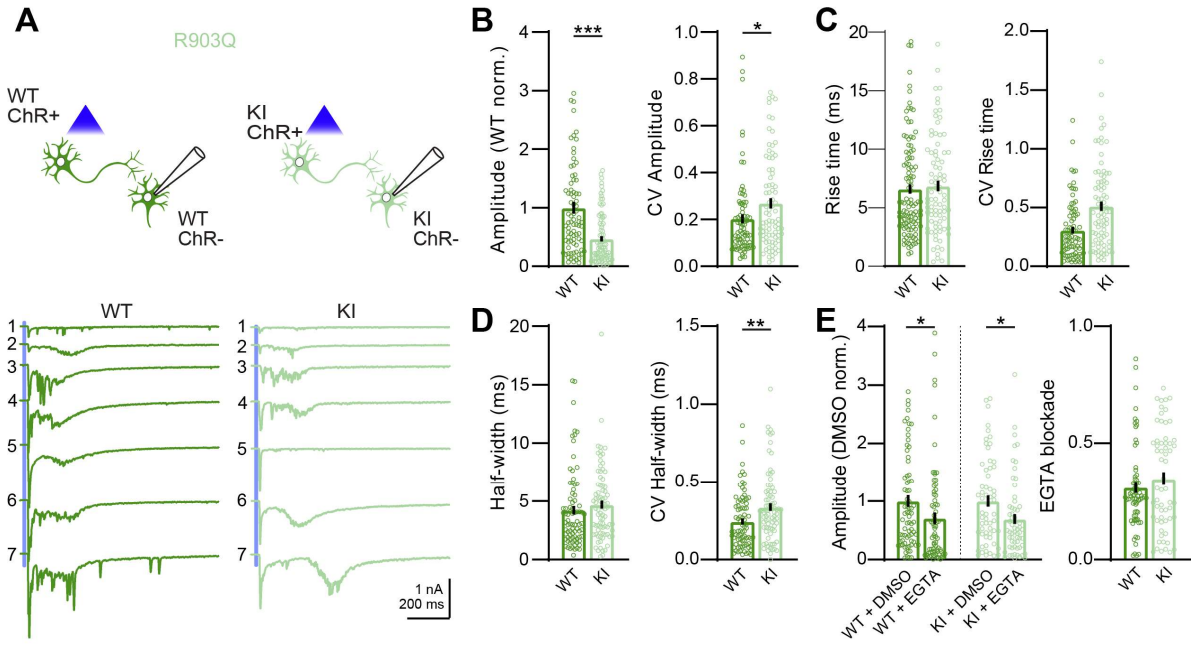

Figure 25. Reduced evoked release in R903Q knock-in iGluts. A) Schematics representing the recording configuration and representative traces of evoked currents of WT and R903Q KI iGluts. B) Quantification of evoked currents amplitude, rise-time and half-width. C) Quantification of amplitude CV, rise-time CV and half –width CV. N = 82-84/3 (cells/batches). D) Quantification of evoked EPSCs amplitude of cells pre-incubated with DMSO or with EGTA, and calculated EGTA blockade. N=60-75/3 (cells/batches). Bar plots indicate the mean of the data. Error bars = SEM. Unpaired t-test, *** p < 0.01. ** p < 0.01. * p < 0.05.

Taken together, iGluts carrying RIM1 ASD-linked missense mutations have notoriously divergent effects. On one hand, the R903Q mutation induces a mild alteration of the active zone, characterized by decreased levels of Munc13 and RIMBP2, while largely preserving

normal synaptic ultrastructure, and normal sensitivity to EGTA, indicating that these defects cannot be attributable to impaired VGCC coupling.

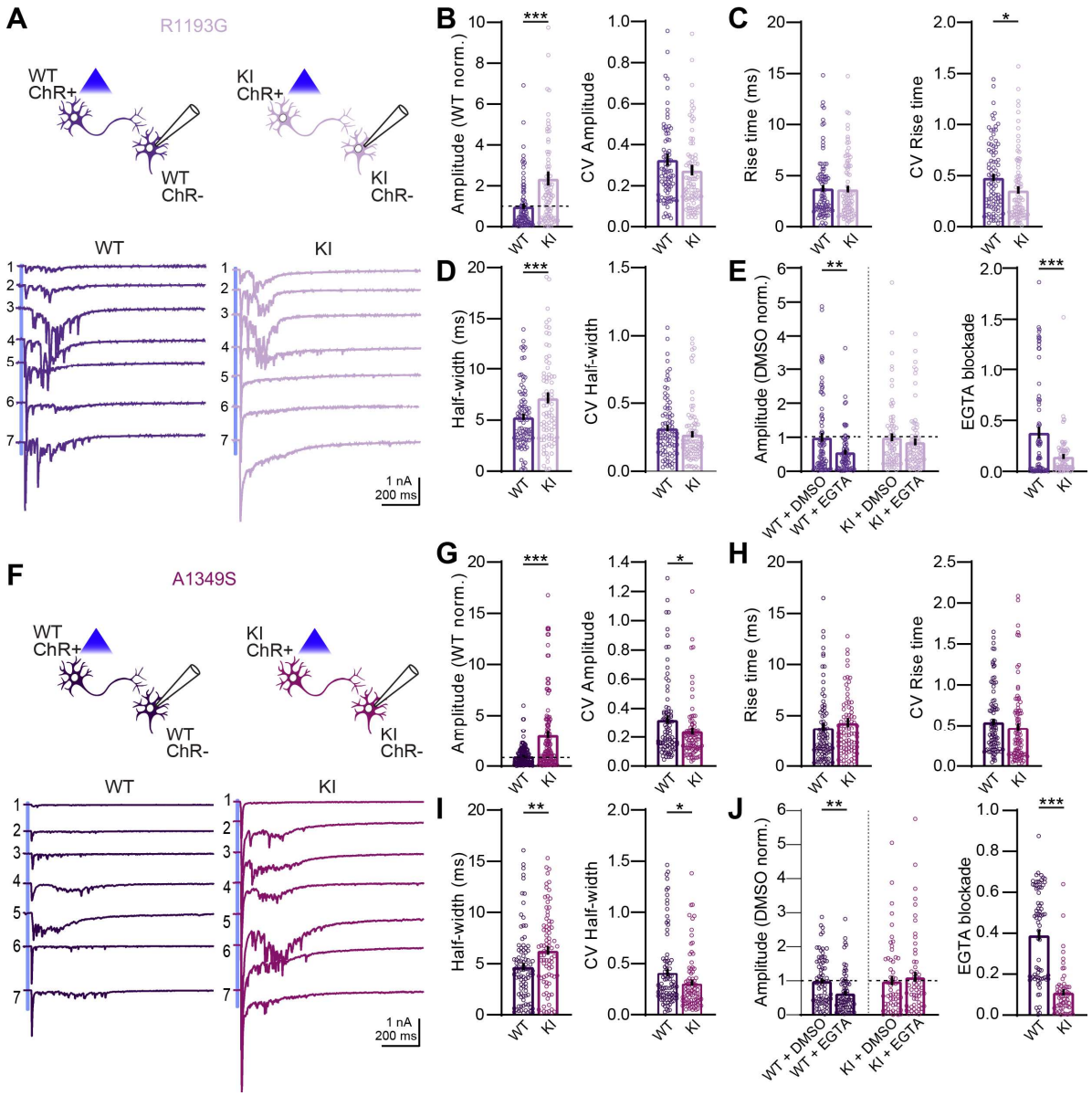

Figure 26. Decreased EGTA sensitivity in R1193G and A1349S knock-in iGluts. A, F) Schematic representing the recording configuration. iGluts expressing Channel Rhodopsin are stimulated by a pulse of blue light while a ChR negative cell is recorded in voltage clamp configuration. Representative traces of evoked currents in RIM1 WT, (A) R1934G KI or (F) A1349S KI iGluts. B, G) Quantification of evoked EPSC amplitude and CV of amplitude, (C, H) rise time and CV of rise time, (D, I) half width and CV of half width. N = 86-33/3 (cells/batches). E, J) Quantification of evoked EPSCs amplitude of cells pre-incubated with DMSO or with EGTA, and calculated EGTA blockade. N=59-75/3 (cells/batches). Bar plots indicate the mean of the data. Error bars = SEM. Unpaired t-test, *** $p < 0.001$, ** $p < 0.01$. * $p < 0.05$.

In contrast, the R1193G and A1349S mutations exhibit a largely normal AZ composition and synaptic ultrastructure, but both mutations lead to a significant increase in evoked current amplitude, accompanied by a pronounced change (a decrease) in the sensitivity of evoked release to the slow calcium chelator EGTA. This indicates that these mutations exert their function by increasing VGCC coupling without any disruption in the active zone structure itself.

Last, I assessed the possibility that RIM1 ASD-linked missense mutations may affect its ability to undergo liquid-liquid phase separation (LLPS). RIM1 is a protein containing a significant proportion of intrinsically disordered regions (IDRs), which may contribute to its LLPS capabilities. Interestingly, all three missense mutations are located precisely within regions of RIM1 classified as IDRs (Figure 26A). To test this, I transfected HEK cells with a plasmid encoding full-length human RIM1 or its mutated variants, along with a plasmid containing RIMBP1, a RIM1 partner known to undergo LLPS with RIM1. I analyzed the formation of LLPS droplets and their dynamics of recovery using FRAP experiments (Figure 26B). As expected, transfected HEK cells exhibited droplets containing both RIM1-Scarlet and RIMBP1-GFP signals, which appeared to colocalize (Figures 26C, E). Upon quantification, I found that RIM1 R903Q displayed significantly fewer droplets compared to the wild type (Figure 26D, left). Conversely, mutations R1193G and A1349S did not differ from the wild type in droplet formation. Interestingly, a slight but significant increase in the size of the R903Q droplets was observed (Figure 26D, middle). Although a small decrease in colocalization levels was noted for R903Q, this difference was not statistically significant. FRAP experiments, which involved bleaching the Scarlet signal, revealed a classic fast recovery pattern commonly associated with LLPS droplets (Figures 26F, G). However, when comparing the maximum recovery after bleaching, the R903Q mutation exhibited a small but statistically significant reduction in recovery. In contrast, mutations R1193G and A1349S showed no differences from the wild type in recovery curves or maximum recovery (Figure 26H, I). Altogether, these experiments indicate that indeed the R903Q might compromise active zone integrity by mildly impairing the ability of RIM1 to phase separate within nerve terminals. In contrast, R1193G and A1349S variants do not affect the ability of RIM1 to undergo LLPS.

Figure 27. Impaired liquid-liquid phase separation in hRIM1 R903Q mutant (next page). A)3D representation of the hRIM1 full-length protein (AlphaFold model) at different angles, highlighting the positions of three ASD-linked missense variants: R903, R1193, and S1349 (residue surfaces in purple). Known domains are shown in different colors. Residues predicted to form “intrinsically disordered regions” (MobiDB-lite) are marked in red. The "front view" was defined arbitrarily; the "side view" was produced by rotation along the z-axis, and the "top view" was generated by rotation in the xy-plane. B) Schematic representation of liquid-liquid phase separation (LLPS) experiments. HEK cells were transfected with a RIMBP1-GFP plasmid and either a wild-type human full-length RIM1-mScarlet plasmid or mutant human full-length RIM1 plasmids carrying ASD-linked missense variants. C) Representative images of droplets formed in HEK cells by the accumulation of RIMBP1-GFP and RIM1-mScarlet (wild-type or mutant). D) Quantification of the number of RIM1-mScarlet droplets (**left**), the size of RIM1-mScarlet droplets (**middle**), and the Pearson colocalization coefficient (**right**) for the mScarlet signal respect the GFP signal in wild-type or mutants RIM1. E) Representative confocal images showing RIM1-mScarlet and RIMBP1-GFP droplets before FRAP. E) Fluorescence intensity measured along the dotted white line is shown in the adjacent graph. F) Representative confocal images from FRAP experiments. "Low mag" shows a low-magnification image of a whole cell, followed by time points from a FRAP experiment on a single droplet (corresponding to the white square in "Low mag"). G) Recovery traces for GFP and mScarlet fluorescence in droplets shown in F. H) Average recovery traces for RIM1 and the three missense mutants. Quantification of the maximum (MAX) recovery after bleaching for RIM1 and the three missense mutants. Scale bars: C, D, and F ("Low mag") = 10 µm; F ("time points") = 1 µm. Bar plots indicate the mean of the data. Error bars = SEM. N = 43-53/3 (cells/batches). Ordinary One-way ANOVA *** $p < 0.001$. * $p < 0.05$.

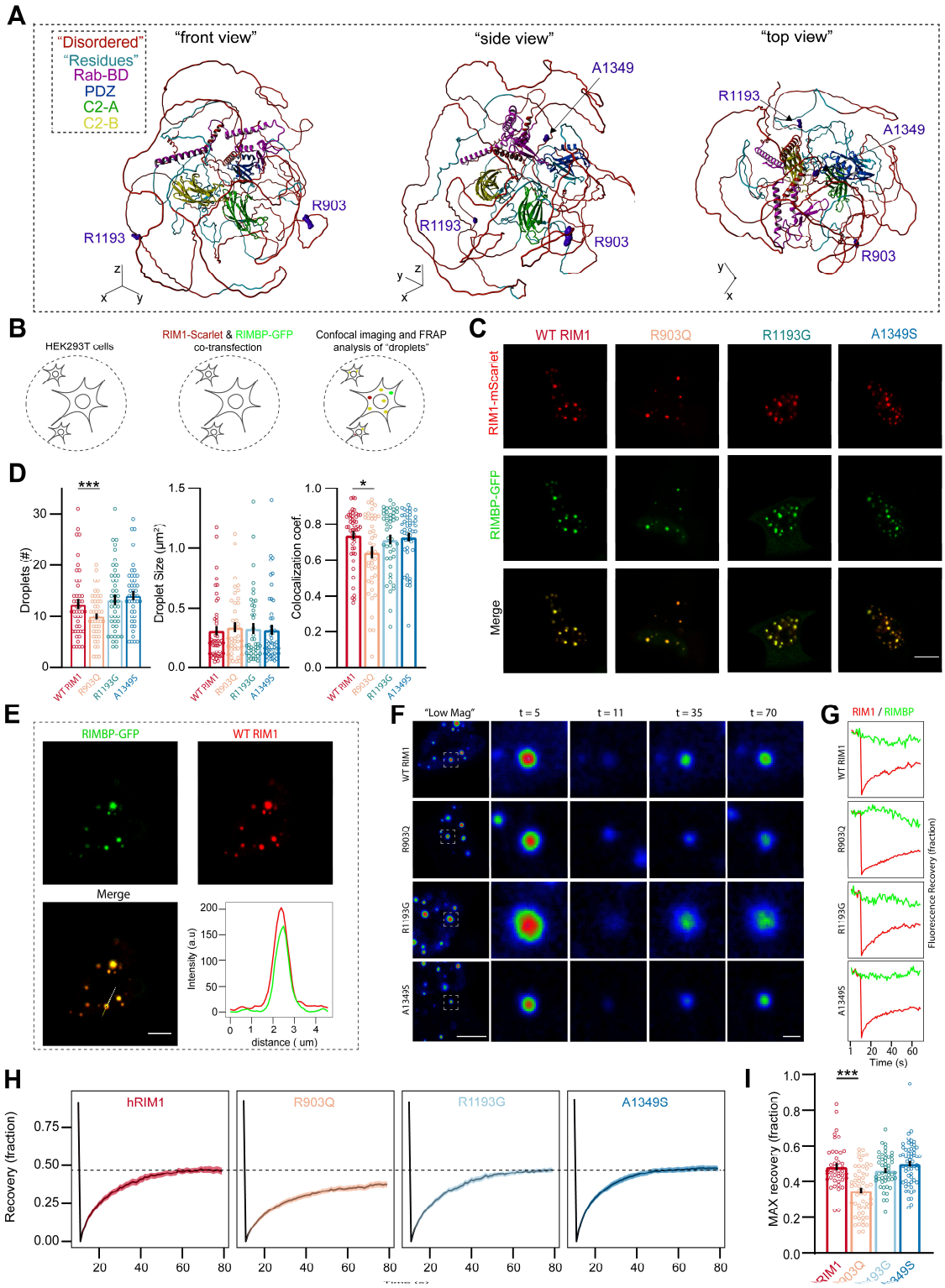
A
"Disordered"
"Residues"
Rab-BD
PDZ
C2-A
C2-B
"front view"
"side view"
"top view"
R903
R1193
A1349
B
HEK293T cells
RIM1-Scarlet & RIMBP-GFP co-transfection
Confocal imaging and FRAP analysis of "droplets"
C
WT RIM1
R903Q
R1193G
A1349S
RIM1-mScarlet
RIMBP-GFP
Merge
D
Droplets (#)
Droplet Size (µm²)
Colocalization coef.
E
RIMBP-GFP
WT RIM1
Merge
Intensity (a.u)
distance (um)
F
"Low Mag"
t = 5
t = 11
t = 35
t = 70
G
RIM1 / RIMBP
Fluorescence Recovery (fraction)
Time (s)
H
hRIM1
Recovery (fraction)
I
MAX recovery (fraction)

4. Discussion

In this thesis, I studied human presynaptic terminals. I focus on a protein called RIM. RIMs are a large and evolutionary conserved protein family and represent a central component of the active zone. Although RIMs were discovered over 20 years ago, and its function in several model organisms has been extensively studied [39, 47, 66, 68, 69], a comprehensive understanding of its role in human active zone structure, synaptic assembly, and neurotransmission remains incomplete. Furthermore, a key member of this protein family, RIM1, is a prominent target of mutations in autistic patients [2, 51-54, 62]. But how RIM1 dysfunction contributes to disease pathogenesis, particularly ASD, is poorly understood. These are the questions I sought to address in this study.

4.1 RIM proteins at the human synapse

In this thesis, I described the basic composition of the human active zone and determined that RIMs play a central role in maintaining its structure and function. I found that genetic deletion of all RIMs in human neurons triggers particularly severe physiological and structural phenotypes, nearly abolishing spontaneous and evoked transmitter release (~95% reduction) (Figures 7 & 8). Structurally, removal of RIMs largely disassembles the active zone, because it dramatically reduced the local levels of other central active zone components such as Munc13 and RIMBP, and also strongly reduced the levels of calcium channels, which normally cluster at the AZ to promote fast, efficient, and highly-localized calcium entry upon the arrival of an action potential. Interestingly, deletion of RIMs also triggered a ~50% increase in the local levels of Liprins (Figure 9), which in human neurons represent the first master organizer of presynaptic assembly ever identified [26]. Although the reason for this increase in Liprin levels is currently unknown, I speculate it might represent a compensatory mechanism in response to depletion of all RIM isoforms from the active zone. Indeed, our own recent findings indicate that under physiological conditions, RIMs rely at least partially on direct interactions with Liprins to cluster at the AZ ([75]). This interaction is mediated by RIM C2B domains and the coiled-coil domain of Liprins. Disruption of these interactions in point mutants revealed that this RIM/Liprin complex does not change the AZ levels of Liprins, but it significantly reduces RIM AZ levels, leading to defects in priming and calcium channel coupling. Thus, the upregulation of Liprins observed here, might represent a mechanism of subcellular compensation aimed to make recruitment of RIMs more efficient, when their levels are downregulated.

I also performed ultrastructural analysis of RIM depleted human synapses using HPF/FS electron microscopy. This analysis revealed that removal of all RIMs from human neurons results in massive defects in vesicle recruitment to the vicinity of the presynaptic membrane (Figure 10). Indeed, vesicles at distances <5 nm from the presynaptic membrane nearly disappeared in the mutants, whereas those located within <30nm were reduced by ~2/3. Altogether, this indicates that RIM proteins are central for the assembly of AZs. In their absence, vesicles recruitment to the release sites is nearly completely prevented. What are the functional consequences of this? Mechanistically, removal of RIMs nearly ablated the pool of readily-releasable pool (RRP) of synaptic vesicles, which I measured by patch clamp, after application of hypertonic sucrose to nerve terminals (Figure 9). This in turn translated into the massive effect on spontaneous or evoked transmitter release, mentioned earlier (Figures 7 & 8).

It is important to mention that these prominent, nearly complete structural and functional phenotypes I observe here in the absence of RIM, differ from previous measurements performed in synapses of other model organisms. For instance, in mice, deletion of RIMs reduces release by ~2/3 in vivo and by ~60% in vitro ([40]). In C. elegans and the fruit fly neuromuscular junction, deletion of RIM reduces evoke release by 50 and 60% respectively [66, 69]. Indeed, in mice, complete physiological and structural phenotypes such as the one I report here, can only be observed upon combine deletion of two entire protein families in RIM1/2–ELKS1/2 and RIM1/2–RIMBP1/2 quadruple knockout neurons [40, 41]. These differences between model organisms are also apparent for another AZ protein family called Liprins. In human neurons, Liprin-α1–4 quadruple resulted in empty presynaptic terminals, completely devoid of synaptic vesicles. In mouse neurons, the same genetic manipulation resulted in only mild effects on the pool of readily releasable vesicles [26, 76].

The reason for these differences are unknown, but I can speculate on two possible scenarios. First, it could be due differences in the experimental design. In all mouse studies, these proteins were conditionally deleted, as their germ-line removal is lethal, and the analyzes were performed 2-3 weeks after conditional deletion. And although complete protein loss by the time of analysis was ensured in these studies, it is conceivable that complete disassembly of the active zone takes longer timeframes. Second, another possibility is that mouse and human synapses inherently differ in how they respond when key synaptic components are disrupted or lost. A compelling example is a recent study in which neurons carrying pathogenic mutations in the synaptic cell adhesion molecule gene *NRXN1* were derived from both human and mouse

embryonic stem cells, using exactly the same protocols and timeframes. Notably, significant phenotypic alterations were observed exclusively in neurons generated from human cells [7], highlighting potential species-specific differences in synaptic vulnerability and regulation.

Last, although my analysis revealed that both RIM1 and RIM2 are expressed in induced human neurons, only RIM1 seems to sustain a major role in synaptic function under normal conditions. Indeed, deletion of RIM1 alone triggers a large physiological phenotype, whereas removal of RIM2 alone does not significantly change transmitter release (Figures 7). Moreover, RIM1 overexpression alone can fully rescue the physiological phenotypes of RIM1/2 dKO. This aspect seems to align well with mouse studies, where RIM1 KO also seems to have a relatively bigger effect than RIM2 in priming due to the presence of the Rab-binding domain next to the Zn-finger domain that interacts with Munc13 [38].

4.2 All RIM1 ASD-linked nonsense mutations produce a mono-allelic loss of RIM1 leading to haploinsuficiency.

My results indicate that ASD-linked nonsense and frameshift mutations analyzed here, result in an approximately 50% reduction in RIM1 protein levels. These mutations are distributed throughout the entire RIMS1 gene, raising the possibility that some may produce truncated protein variants, which still might be functional if many of their domains remain intact. However, qPCR analysis revealed a concomitant decrease in RIM1 mRNA levels across all mutants, irrespective of the mutation's position within the gene—including the most upstream mutation located in exon 24. This finding is consistent with nonsense-mediated mRNA decay triggered by the presence of a premature stop codon [77]. Indeed, this mechanism seem to prominently operate for RIM1, as nearly complete depletion of RIM1 mRNA has been observed in conditional RIM1 knockout mice, in which Cre recombinase-mediated deletion of exon 6, which creates a frameshift leading to an early stop codon, causes to a drastic reduction in transcript levels [67, 78].

Phenotypically, all clones carrying these nonsense mutations developed iGluts with normal overall morphology and normal synapse densities. Previous studies have also reported no significant morphological alterations in RIM mutants and have shown that homozygous deletion of RIM1—or even both RIM1 and RIM2—does not affect synapse density in hippocampal CA1 neurons within the distal stratum radiatum or in cultured mouse hippocampal neurons [39, 79]. However, physiological analysis of these mutations revealed a consistent pattern of reduced activity. Using MEA, a medium-throughput assay capable of measuring the activity of dozens

of cells simultaneously across multiple electrodes in a single well, I observed a significant (~20-30%) decrease in the total number of detected spikes. Interestingly, when considering only "network spikes"—defined as spikes occurring simultaneously in at least four electrodes within a 10 ms window—I found an even greater reduction across mutants (40-50%). This is particularly relevant, as network spikes are more likely to reflect activity arising from synaptically connected cells (i.e. synaptic activity), intrinsic firing of induced neurons due to spontaneous oscillation of their membrane potential.

Indeed, I could demonstrate these synaptic phenotypes using a more precise, single-cell approach, such as patch-clamp recordings. This analysis revealed two key findings. First, the mutations did not alter intrinsic cellular properties, as indicated by unaltered input resistance, rheobase, and action potential threshold (data not shown). Second, I observed a striking ~50% reduction in the frequency of mEPSC, without changes in their amplitude or kinetics. This result is unexpected, as previous studies in cultured hippocampal neurons have reported such a substantial decrease only in the complete knockout of RIM1 (CA1 inhibitory interneurons)[67]. Indeed, in early studies, heterozygous mutants were not uncommonly used as controls.

Since all nonsense mutations led to reduced RIM1 protein and mRNA levels and consistently impaired synaptic transmission, I hypothesize that they contribute to pathogenesis by decreasing RIM1 dosage. This form of haploinsufficiency has been observed in mouse models for other synaptic proteins, including CASK, STXBP1, and SHANK3 [63, 80, 81]. I directly tested this in straight heterozygous RIM1 knockout neurons I generated, where RIM1 levels are reduced by ~50%. And indeed, they displayed an approximately 50% reduction in synaptic transmission, mirroring the release defects observed in the panel of nonsense and frameshift mutations. Thus, this approach uncovered haploinsufficiency phenotypes for human RIM1.

Mechanistically, a ~50% reduction in RIM1 levels, partially disassembled active zone, which prominently affected the size of the RRP (reduced by ~70%) by impairing vesicle docking, but did not affect calcium channel density (Figure 20) or their fine scale localization (Figure 19) within the active zone. This result is surprising, because RIMs are known to regulate both process, and indeed complete deletion of RIMs did change both the RRP and AZ calcium channels (Figure 20). So why organization of vesicle pools and in particular of those forming the RRP is more sensitive to RIM1 dosage than recruitment of calcium channels? I speculate this might have to do with the stoichiometry of protein utilization for these processes. Specifically, mobilization of vesicles might require a large number of RIM molecules, whereas

tethering calcium channels to the release sites might not. Indeed, it is known that very few calcium channels are required for spike-mediated vesicle fusion and release of neurotransmitters [71, 82]. Some studies suggest that even a single calcium channel can trigger release of a synaptic vesicle upon arrival of an action potential [83]. In stark contrast, vesicular proteins, and in particular those that interact with RIM (Rab3A) to form the priming complex with Munc13, are much more abundant. Quantitative estimations indicate that each vesicle has around a dozen of Rab3A molecules, thus facilitating the formation of at least as many priming complexes per vesicle [84]. Another potential explanation might be that a reduction in RIM1 levels, as it occurs in heterozygous mutants or in neurons carrying the nonsense variants, also reduces the levels of Munc13 at the AZ, which is also essential for priming, whereas other AZ proteins involved in calcium channel tethering to the AZ zones are not changed (Figure 20), and thus can more easily compensate for RIM1 loss.

Taken together, the findings presented here provide evidence that ASD-associated nonsense mutations in RIM1, which lead to reduced synaptic RIM1 protein levels, impair synaptic transmission by disrupting AZ organization, decreasing Munc13 levels, thus affecting the pool of SVs positioning in close proximity to the presynaptic membrane, commonly known as RRP.

4.3 RIM1 ASD linked missense mutations have divergent phenotypes by affecting different RIM1 functions.

Three of the ten mutations analyzed in this thesis are missense mutations. Interestingly these mutations are located in highly conserved amino acids across mammalian RIM1s (Figure S8) nonetheless they do not fall into any of the classical functional domains previously described, but rather into intrinsically disordered regions, IDRs (Figure 2.25A). In contrast to nonsense variants, none of these missense mutations alter AZ RIM1 levels, but trigger distinct functional phenotypes.

Two of these variants, R1193G and A1349Q, strongly increased synaptic transmission, despite no detectable changes in AZ composition, synaptic ultrastructure. Remarkably, this effect was mediated by changes in the fine scale localization of VGCC within the AZ, because the sensitivity of EGTA of evoked release was significantly decreased, indicating a reduction in the physical distance between AZ calcium channels and the vesicular calcium sensor (Synaptotagmin) [39, 85]. But how can this be explained mechanistically? My results indicate that these two pathogenic variants do not change the density of calcium channels at the active zone, and thus cannot be simply due to changes in the copy number calcium channels (Figure

24). Instead, I hypothesize this might be due to strengthening interactions with other molecules controlling calcium channel localization, such as RIMBPs [39, 86]. Along this line, it is interesting to point out that these two pathogenic variants are located in proximity to the PXXP domains of RIM, which are used for interactions with RIMBPs. Future studies aiming to measure the strength of RIM1/RIMBP binding might help clarify this issue. Another possible mechanistic explanation for these phenotypes might be that the mutation changes AZ levels of other calcium channels different than CAV2.1. In fact, bulk mRNA sequencing has shown high levels of expression of CAV2.2 and CAV2.3 in iGluts [87] . Sadly, no good antibodies exist for those presynaptic channels, and thus this hypothesis cannot be tested directly. Last, regardless of the underlying molecular mechanism, it is very likely that changes in coupling are due to nanoscale re-organization of the presynaptic VGCC within the active zone. Thus, this might represent sub-active zone changes operating at distances of 20nm or even lower [44, 82]. This is, clearly, below the spatial resolution and sensitivity of STED microscopy, which was used here. Future studies using technologies with higher spatial resolution such as Minflux [88] or DNA–PAINT [89], might help clarify these questions.

The last missense variant studied, the R903Q mutation, triggered not an increase in transmission (as for the two variants discussed above), but rather the opposite: a sizable decrease in overall synaptic function. This likely resulted as a consequence of subtle alterations in AZ composition, because small changes in Munc13 and RIMBP2 levels were detected using STED microscopy (Figure 24). These changes, however, were not pronounced enough as to trigger detectable changes in the ultrastructure of nerve endings or in the organization of vesicle pools, including the RRP (Figure S6). Furthermore, this was not due to changes in VGCC coupling to synaptic vesicles, because the EGTA sensitivity remained unaffected (Figure 25). Rather, the AZ changes triggered by these mutations might be a consequence of altering the ability of RIM to undergo phase separation within nerve terminals (Figure 27). Phase separation is critical for proper AZ assembly, and relies specifically on the formation of RIM/RIMBP co-condensates, which initiate the nucleation of the active zone [90]. Without RIM/RIMBP complexes, no active zone is formed in vitro [90] or in vivo [40]. Remarkably, my results indicate that the R903Q mutation reduces RIM1’s ability to undergo liquid-liquid phase separation (Figure 27). This, I hypothesize, might lead to small changes in AZ levels of Mucn13 and RIMBP2, and ultimately to reduction in release probability. Notably, a recent study demonstrated a reduction in Munc13 nanodomains size following LLPS disruption [91]. Future studies aiming to uncover the exact underlying mechanism, are warranted.

4.4 Strengths and Limitations

This study is based on the use of human PSCs in which I introduced ASD-associated RIM1 mutations to generate a panel of isogenic cell lines carrying these mutations alongside their respective controls. This approach, in my view, has many advantages. For example, it eliminates the potential confounding effects of genetic background variability and enables the investigation of phenotypes under endogenous and physiologically relevant levels of mutant proteins. Moreover, it allowed me to generate multiple clones for each variant, and to model all variants affecting RIM1, thus enhancing the robustness of the analysis and facilitating the identification of convergent pathogenic mechanisms.

Nonetheless, like any other approach, this also has limitations. One of these could be that induced neurons represent a generic type of human neuron, which to some extent resemble a forebrain excitatory glutamatergic neuron according to mRNA expression profiles [22, 65, 87]. This means that these findings may not generalize to every type of neuron or synapse. Moreover, brain expression of RIM proteins is not homogeneous. For instance, according to Human Brain Atlas data RIM1 and RIM2 are similarly expressed in the neocortex, though the first is highly expressed in the cerebellum and the second highly enriched in the eye. This indicates that these two proteins may have different levels of importance in synapses located in these different tissues, in which their expression may be modulated to the required levels. Thus, it is clear that the functions of many synaptic components are synapse- and cell—type specific [92-95], and therefore, these potential differences cannot be studied using my model system. Another potential limitation could be that all these analyses were done in a two-dimensional system, as oppose to circuits operating in a more naturalistic 3D environment. This of course, might be relevant, particularly for genetic perturbations that affect dendritic or axonal morphology, and connectivity. However, our initial assessment indicates that RIM1 pathogenic variants have a purely synaptic phenotype, suggesting that a 2D system might be good enough to study this. Last, an evident limitation of this study is that it was all done in vitro, raising questions as to whether findings from in vitro assays can be readily assumed to be reproduced in vivo. While I think this might be a reasonable criticism for research in model organisms where experiments could potentially be reproduced in whole animals, it might not be for research in human neurons, not only for obvious ethical reasons, but also because of specie-specific phenotypes, which likely would not be possible to adequately recapitulate in other model organisms.

5. Conclusion

This thesis aimed to study the basic biology of human presynaptic terminals, and its dysfunction in genetic models of ASD. It focused on RIMs, a protein family that is a central and evolutionary conserved component of the presynaptic active zone. My main findings can be summarized as follows.

First, at the most fundamental level, I found that RIMs are particularly essential for human presynaptic function. Genetic deletion of all main RIM isoforms blocked the assembly of human active zones, causing massive impairments if synaptic vesicle docking, and priming, and ultimately nearly completely eliminating spontaneous and evoked synaptic transmission.

Second, in human neurons RIM1 and RIM2 have redundant roles, with RIM1 having a more prominent role than RIM2. Indeed, individual deletion of RIM1 reduced transmission by ~50% whereas deletion of RIM2 rendered no significant changes on transmission. However, combined deletion nearly completely ablates neurotransmitter release.

Third, RIM1 is a prominent target in autism pathogenesis. Indeed, thus far ten exonic variants impacting RIM1 have been identified in patients with ASD, indicating that RIM1 dysfunction might contribute to ASD very high-penetrance. However, despite its obvious significance, how any of these RIM1 pathogenic variants impact human synaptic function to disease was unknown. In an effort to uncover the underlying convergent pathogenic mechanism, I used medium-to-high throughput CRISPR/Cas9 homology-directed repair technology to generate a panel of pluripotent stem cell lines carrying all the currently ADS-linked RIM1 variants (10!) and their corresponding isogenic controls.

Fourth. Morphological analysis of neurons containing each of these variants and their isogenic controls, revealed that none of the variants changed the basic morphology of human neurons or the density of human synapses. In contrast, biochemical measurements revealed that 7/10 variants reduce RIM levels, while the remaining 3 variants do not change it.

Fifth. Large-scale multi-electrode array recording revealed that each variant studied in this project alters human neuron network activity. Eight of these variants reduce it, while the remaining two increase it.

Sixth. Detailed analysis using patch clamp electrophysiology, super-resolution STED microscopy, electron microscopy, and liquid-liquid phase separation experiments revealed that these pathogenic variants trigger two convergent mechanisms of pathogenicity within nerve terminals. 1. They disrupt the proper assembly of presynaptic active zones leading-this explains the reduction in transmission triggered by 8/10 variants. 2. They change the fine-scale localization of the presynaptic calcium channels within the active zones-this explains the increased transmission triggered by 2/10 remaining variants.

Seventh, these results indicate that well-balanced information transfer is essential for the correct operation of human neural networks. Genetic disruptions that reduce or exacerbate synaptic transmission can disrupt this balance thereby contributing to disease pathogenesis. Moreover, my work is the first to link presynaptic dysfunction to autism pathogenesis. The mechanistic insights I gained through this work, is expected to pave the way for future development of therapeutic strategies to treat autism caused by presynaptic dysfunction.

6. Material and Methods

6.1 Materials

6.1.1 Cells

Cells	Culture Media	Origin
Healthy donor 6 (HD6)	mTeSr Plus / E8	Heidelberg University
HEK293	DMEM plus FBS	ATCC
Mouse Astrocytes	DMEM plus FBS	P0 pups
WA01 (H1)	mTeSr Plus / E8	Wii Cell

6.1.2 Cell culture reagents

Reagent	Supplier	Catalog #
Accutase	SIGMA (Saint Louis, USA)	A6964
Alt-R™ S.p. Cas9 Nuclease V3	IDT (Leuven, Belgium)	1081059
Antibiotic/Antimicotic	Thermo Fisher Scientific (Carlsbad, USA)	15240062
Ascorbic Acid	SIGMA (Saint Louis, USA)	A4034
B-27 Supplement	Thermo Fisher Scientific (Carlsbad, USA)	17504001
B27-Plus	Thermo Fisher Scientific (Carlsbad, USA)	A3582801
β-mercaptoethanol	SIGMA (Saint Louis, USA)	M3148
Brain-derived Neurotrophic Factor (BDNF)	Prepotech (Rocky Hill, USA)	450-02

Cytosine β-D-arabinofuranoside (Ara-C)	SIGMA (Saint Louis, USA)	C1768
Doxycycline	SIGMA (Saint Louis, USA)	D5207
D-Glucose	SIGMA (Saint Louis, USA)	G7021
EDTA 0.02%	SIGMA (Saint Louis, USA)	E8008
Fetal Bovine Serum (FBS)	SIGMA (Saint Louis, USA)	F7524
Fibroblast Growth Factor 2 (FGF2)	Prepotech (Rocky Hill, USA)	100-18B
Glial-Derived Neurotrophic Factor, ATF-1 (GDNF)	Prepotech (Rocky Hill, USA)	450-10
Geltrex	Thermo Fisher Scientific (Carlsbad, USA)	A1413301
Glutamax	Thermo Fisher Scientific (Carlsbad, USA)	35050061
Hanks' Buffered Saline Solution (HBSS)	Thermo Fisher Scientific (Carlsbad, USA)	14170112
HEPES	SIGMA (Saint Louis, USA)	H4034
Hygromycin B	SIGMA (Saint Louis, USA)	H3274
Insulin	CSBio (Sillicon Valley, USA)	CS9212
Laminin	SIGMA (Saint Louis, USA)	L2020
L-Glutamine	Thermo Fisher Scientific (Carlsbad, USA)	A2916801
Lipofectamine STEM		STEM00001
Matrigel	Corning (New York, USA)	354277
MEM Non-essential amino acids (NEAA)	Thermo Fisher Scientific (Carlsbad, USA)	11140050
N2-Supplement	Thermo Fisher Scientific (Carlsbad, USA)	17502001
Neurotrophin-3 (NT3)	Prepotech (Rocky Hill, USA)	450-03

Papain	SIGMA (Saint Louis, USA)	P4762
Phosphate Buffered Saline (PBS)	SIGMA (Saint Louis, USA)	P2272
Penicillin / Streptomycin	Thermo Fisher Scientific (Carlsbad, USA)	15140122
Polyethylenimine	Polysciences (Warrington, USA)	23966
Poly-L-ornithine (PO)	SIGMA (Saint Louis, USA)	A-004-M
Poly-L-lysine (PL)	SIGMA (Saint Louis, USA)	P4832
Puromycin	SIGMA (Saint Louis, USA)	P8833
Sodium pyruvate	Thermo Fisher Scientific (Carlsbad, USA)	11360070
Sodium Selenite	SIGMA (Saint Louis, USA)	S5261
Transferrin	SIGMA (Saint Louis, USA)	T8158
Transforming Growth Factor-β1 (TGFB1)	Prepotech (Rocky Hill, USA)	100-21
Trypan blue	Thermo Fisher Scientific (Carlsbad, USA)	15250061
Trypsin-EDTA, 0.5%	Thermo Fisher Scientific (Carlsbad, USA)	15400054
Y27632	Axon MEDCHEM (Groningen, Netherlands	1683

6.1.3 Commercially available culture medium

Medium	**Supplier**	**Catalog #**
Dulbecco's Modified Eagle's medium (DMEM) Advanced	Thermo Fisher Scientific (Carlsbad, USA)	12634010
Dulbecco's Modified Eagle's medium (DMEM) High Glucose	Thermo Fisher Scientific (Carlsbad, USA)	11965092

mTeSR plus medium	StemCell Technologies	A4034
DMEM/F12 (L-Glutamine, $NaCO_3$)	Thermo Fisher Scientific (Carlsbad, USA)	11330032
mTeSR plus medium	StemCell Technologies	100-0276
Neurobasal-A	Thermo Fisher Scientific (Carlsbad, USA)	10888022
Neurobasal-Plus	Thermo Fisher Scientific (Carlsbad, USA)	A3582901
Opti-MEM	Thermo Fisher Scientific (Carlsbad, USA)	31985070

6.1.4 Custom-made cell culture medium

Medium	**Main component**	**Supplements**
B27 Base medium	Neurobasal-A	1% B27 Supplement, 1% Glutamax, Doxycycline, 10 ng/mL Puromycin ,BDNF, 10 ng/mL NT3
B27 Final medium	Neurobasal-A	1% B27 Supplement, 1% Glutamax, 5% FBS
HEK cell medium / Mouse Astrocytes medium	DMEM High Glucose	10 % FBS,1% Pen/Strep
Essential Medium 8	DMEM/F12 (L-Glutamine**,** $NaCO_3$)	25 mM HEPES, 64 µg/mL Ascorbic Acid, 14 ng/mL Sodium Selenite, 10.7 µg/mL Transferrin, 20 µg/mL Insulin, 100 ng/mL FGF2, 2 ng/mL TGFβ1.
N2 medium	DMEM/F12 plus glutamine and HCO3	1 % N-2 Supplement, 1% NEAA, 10 µg/mL Doxycycline, 10 ng/mL BDNF, 10 ng/mL NT3, 200 ng/mL mouse Laminin

Neural Expansion medium	Neurobasal Plus	1 % Neural induction Supplement
Neural Induction medium	50% DMEM Advanced, 50% Neurobasal Plus	1 % Pen/Strep, 1 % Neural induction Supplement
Neural Maturation medium	50% DMEM Advanced, 50% Neurobasal Plus	1% Glutamax, 1 % N-2 Supplement, 1% Pen/Strep, 1 % B27 Supplement, 10 ng/mL BDNF, 10 ng/mL GDNF

6.1.5 Molecular Biology & Electrophysiology reagents

Reagent	**Supplier**	**Catalog #**
100bp DNA ladder	New England Biolabs (Ipswich, UK)	N3231L
1kb DNA ladder	New England Biolabs (Ipswich, UK)	N3232L
Acetic acid	SIGMA (Saint Louis, USA)	695092
Adenosine 5′-triphosphate (ATP)	SIGMA (Saint Louis, USA)	A6419
Agarose	SIGMA (Saint Louis, USA)	A9539
AquaPolymount	Polysciences (Warrington, USA)	18606-
Bovine serum albumin (BSA)	SIGMA (Saint Louis, USA)	810533
Calcium chloride	SIGMA (Saint Louis, USA)	21115
CloneAmp	Takara(Kyoto, Japan)	639298
Competent Cells	New England Biolabs (Ipswich, UK)	C2988J
DAPI	SIGMA (Saint Louis, USA)	D9542
Dithiothreitol (DTT)	SIGMA (Saint Louis, USA)	D9760

EGTA	SIGMA (Saint Louis, USA)	E3889
EGTA-AM	Thermo Fisher Scientific (Carlsbad, USA)	E1219
Ethanol absolute	Merck (Darmstadt, Germany)	107017
Gel Loading Dye, Purple (6X)	New England Biolabs (Ipswich, UK)	B7024S
Glycerol	Merck (Darmstadt, Germany)	356352
Hydrochloric acid (HCl)	Merck (Darmstadt, Germany)	143007
In-Fusion Assembly Master Mix	Takara(Kyoto, Japan)	638949
Isopropanol	Merck (Darmstadt, Germany)	109634
LB Broth	Merck (Darmstadt, Germany)	71753
Methanol	Merck (Darmstadt, Germany)	106012
Myo-Inositol	SIGMA (Saint Louis, USA)	I5125
Nuclease-free water	SIGMA (Saint Louis, USA)	W4502
Paraformaldehyde (PFA)	SIGMA (Saint Louis, USA)	P6148
PerfeCTa SYBR Green SuperMix Low ROX	Quantabio (Beverly, USA)	733-1251
PMSF	SIGMA (Saint Louis, USA)	P7626
Potassium chloride (KCl)	Merck (Darmstadt, Germany)	104936
Precision gRNA Synthesis	Thermo Fisher Scientific (Carlsbad, USA)	A29377
ProLong Glass antifade	Thermo Fisher Scientific (Carlsbad, USA)	P36980

Potassium hydroxide (KOH)	Merck (Darmstadt, Germany)	109108
Protease inhibitor	Roche (Basel, Switzerland)	04693132001
Proteinase K	SIGMA (Saint Louis, USA)	P2308
Pyruvate	SIGMA (Saint Louis, USA)	P5280
Quickchange II XL Site-Directed Mutagenesis Kit	Agilent(Santa Clara, USA)	200521
Quick Ligase	New England Biolabs (Ipswich, UK)	M2200L
qScript cDNA SuperMix	Quantabio (Beverly, USA)	733-1178
Sucrose	SIGMA (Saint Louis, USA)	S0389
Sodium Carbonate	SIGMA (Saint Louis, USA)	S4132
Sodium dodecyl sulfate (SDS)	SIGMA (Saint Louis, USA)	L3771
Restriction enzymes	New England Biolabs (Ipswich, UK)	----------
Taq Polymerase	Meridian (London, UK)	BIO-21107
Tetrodotoxine (TTX)	HelloBio(Bristol, UK)	HB1034
Triton X-100	SIGMA (Saint Louis, USA)	T8787
Tween-20	SIGMA (Saint Louis, USA)	P2287
T4 DNA Ligase	New England Biolabs (Ipswich, UK)	M0202L

6.1.6 Buffers

Buffer	**Composition**
ACSF	125mM NaCl, 2,5 mM KCl, 1 mM MgCl, 2 mM CaCl, 25 mM glucose, 1.25 mM NaH_2PO_4, 0.4 mM ascorbic acid, 3 mM myo-inositol, 2mM Na-pyruvate,25mM $NaHCO_3$.

ACSF high calcium	125mM NaCl, 2,5 mM KCl, 0.1 mM MgCl, 4mM CaCl, 25 mM glucose, 1.25 mM NaH_2PO_4, 0.4 mM ascorbic acid, 3 mM myo-inositol, 2mM Na-pyruvate,25mM $NaHCO_3$.
Blocking buffer	0.02% Triton X-100, 10% NDS in PBS
Current-clamp internal solution	125mM K–gluconate, 20mM KCl, 4mM MgATP, 10mM Na–phosphocreatine, 0.3mM Na-GTP, 0.5mM EGTA, and 10mM HEPES
Fixation buffer	4% PFA, 4% Sucrose in PBS
RIPA buffer	150mM NaCl, 50mM Tris, 0.1% SDS, 0.5 Sodium Deoxycholate, 1% Triton X-100
Sucrose for puffing	0.5 M sucrose dissolved in DDW
TAE	40mM Tris, 20mM Acetic Acid, 1mM EDTA
Thowbin Buffer	25mM Tris, 192mM glycine
Voltage-clamp internal solution	125mM Cs–gluconate, 20mM KCl, 4mM MgATP, 10mM Na–phosphocreatine, 0.3mM Na-GTP, 0.5mM EGTA, 2mM QX314 (HB1030, Hello Bio) and 10mM HEPES

6.1.7 Primary Antibodies

Target	Supplier	Catalog #
Bassoon (Rabbit)	SIGMA	141003
CAV2.1 (Rabbit)	Synaptic Systems	152103
ELKS (Rabbit)	Synaptic Systems	143003
Homer-1	Synaptic Systems	160003
Liprin-α3 (Rabbit)	Gift from Brose Lab	----------
Munc13a (Rabbit)	Synaptic Systems	126103

Map2 (Chicken)	Novus	NB300-213
Nanog (Rabbit)	StemAb	RCAB004P-F
Piccolo (Rabbit)	Synaptic Systems	142003
PSD-95 (Mouse)	NeuroMab	K28/43
RIM1 (Rabbit)	Synaptic Systems	140003
RIM1/2 (Rabbit)	Synaptic Systems	140213
RIM2 (Rabbit)	Synaptic Systems	140103
RIMBP2 (Rabbit)	Synaptic Systems	316103
SSEA-3 (Mouse)	DSHB	MC-631
SSEA-4 (Rat)	DSHB	MC-813-70
Synapsin (Rabbit)	Custom made	----------
Synaptophysin (Guinea Pig)	Synaptic Systems	101308
TUJ1 (Mouse)	BioLengend	MMS-435P
TUJ1 (Rabbit)	SIGMA	T3952

6.1.8 Plasmids

Plasmids	**Supplier**	**Catalog #**
FSW-GFP-NLS-T2A-msRIM1	Gift from Rosenmund Lab	
FSW-msRIM1-RFP	Gift from Rosenmund Lab	
FUW-TeTx-EGFP	This Study	-
FUW-M2rtTA	Addgene	20342
FUW-oChIEF-tdTomato	This Study	-
pCMV-VSV-G	Addgene	8454
PLV-hRIM1-Scarlet	This Study	-
PLV-hRIM1-GFP	Study	-

PLV-hRIM1-R903Q-Scarlet	This Study	-
PLV-hRIM1-R1193G-Scarlet	This Study	-
PLV-hRIM1-A1349S-Scarlet	This Study	-
pMDLg/pRRE	Addgene	12251
pRSV-Rev	Addgene	12259
RIMS1-pDONR221	DNASU	HsCD00745403
TetO-DLX2-hygro	Addgene	97330
TetO-hAscl1-puro	Addgene	97329
TetO-Ngn2-puro	Addgene	52047

6.1.9 Primers and DNA oligonucleotides

RIMS1 flanking primers (flank exons where ASD mutations are located)

Exon	*Flanking FWD primer*	*Flanking REV primer*
2	AAAGACCTGTGTGGTGATTGATGG	ACTCAGCACCCTGTCTGTATCTT
5	ACCTCTACTCTGGCTGCTGA	TGTTTTTCCATGTGGGGCCT
6	CCTTGCAAGGTAAGTATTTTTCAGC	GGACTGGTCTGAGCTCAAAG
16	GAACCTTTCCACTCAGCCCTAT	CTTACGCTCAGAGCATTGTGAAA
20	TTCATAGAGTTTGGTTAGCAGGT	TGACAAAGCAACTAGAATTCTGAC
21	TGCGTGTTTGTGTTGCTACG	CAGGAACAGATGCCACACCA
23	CCACCTTTGCAACTCTACCCA	GGTGCTTTACCAGAGTTGGC
24	CGAGTTGCTCAGTAGGGGTT	TTCCAGGCACTACATTCATTGG
25	AAACCACATGGCGTTCACATT	CAGATGAAAGGACATAACACAGCC
28	CCACTGAGCATTTCTTTTACAC	ACACATCCACTACACCCAC

RIMS1 screening primers (bind regions where mutations are introduced)

Exon	*Screening CTRL primer*	*Screening MUT primer*
2	TCGCCATGTCCCTGACAACA	CGCCATGTCCCTTCACCAC
5	CAGGATGGAACCCTGAGTGATAC	CAGGATGGAACCCTGAGTGATAA
6	TTTTTCCGGCGTGTCTGGG	TTCCGGCGTGTCTGGGTAA
16	TTGTGCAGGATCTCAGCG	TTGTGCACGATCCCACCA
20	CAGACATCTTGTTAGGCACTATAAAAC	CAGACACCTTGTTAGGCACTATAAAC
21	ACATTTCCCTTCATCATGAATGC	GACATTTCCCTCCATCATGAATGA
23	CCCCCTCCCTAGATAGGAGAC	CCCCTCCCTAGATAGACGGT

24	TTTCCTAGTCTGTTTTTGGATGCT	CTGAAAGATCTTCGATACAGAAGC
25	GGGTTCTCCCAACATGTCTTTCTA	GGGTTCTCCCAACATGTCTTTCTG
28	GCTGGTTCGGGAAATGGC	CTGGTTCGCGAGATGGAC

Flanking RIMS1 primers

Mutation	***Exon***	***Flanking FWD primer***	***Flanking REV primer***
Full KO	9	TTCCTTAGGACACATAGTCATCTC	GCAGTCAAGTCAACTGGAAGAA

Flanking RIMS2 primers

Mutation	***Exon***	***Flanking FWD primer***	***Flanking REV primer***
Full KO	11	CCTGTTTTGTTTCCCCTAAGACC	GCTACCACCCTAAGTCGTTTTC

Inside Primers RIMS1 and RIMS2

Mutation	***Exon***	***Inside FWD***	***Inside REV***
RIMS1KO	9	AGGACGACTTGGTGCTTTCATC	CAGATTGCTGCTGATGTAGAGTT
RIMS2KO	11	ATGGAAGACTACTGCAAGGAGC	TTTGGTGTGGTGCTTTTGTTAAGG

qPCR primers

Target	*Exon*	*Flanking FWD primer*	*Flanking REV primer*
RIMS1	15-16	CTCAGCCATCACCTTTCATGCC	CTGGAGGAACTACGCCAATACC
RIMS2	10-11	GACTGAATCAGGTCGGCTTTGTG	GTGGCTCCTTGCAGTAGTCTTC
RIMS3	6-7	TGCACATTGCCATCATGGACCG	CCCATTCTCCAGCAGGTAAACC
RIMS4	4-5	ACGGTCAGTTGGAGGTGGACAT	GATGCCATTCTCTAGCAGGTAGG
UBE2R2	3-4	CACAGAGTGGAGAACTGCCTTC	CTGAAGCATCGACATTGGCTGG
GAPDH	6-7	GTCTCCTCTGACTTCAACAGCG	ACCACCCTGTTGCTGTAGCCAA

Dual sgRNAs for full KO

Target	*Sequence*
RIMS1 exon9	5-AAATGTAGGTGAAGCCCTGG-3
RIMS1 exon9	5-TACCAAGTAGCCTAGACCAC-3

RIMS1 exon9	5-GCAATCTGGAGAGTAAGGGT-3
RIMS1 exon9	5-GGTCCTAAAACACTTATTCA-3
RIMS2 exon11	5-CAGGAAAGGACAATGATCGG-3
RIMS2 exon11	5-GTGGTTATAGGATTTAGTAG-3

sgRNAs for RIMS1 HDR

Mutation	*Exon*	*Sequence*
1	2	5-TGCGCCCCAGGTGTGTTGTC-3
2	5	5-ACCTGTAGCTGTATCACTCA-3
3	6	5-ACAGGATTACCCAGACACGC-3
4	16	5-TCTTTGCCTTACTGTTGTGC-3
5	20	5-TACGTTCCAGACATCTTGTT-3
6	21	5-GTTAAAGCATTCATGATGAA-3
7	23	5-TAGGAGGTCGTCTCCTATCT-3
8	24	5-ATCCAAAAACAGACTAGGAA-3
9	25	5-CCCAACATGTCTTTCTAGAA-3
10	28	5-ACTGCTGGTTCGGGAAATGG-3

Single-stranded DNA donors for HDR

Mutation	Exon	Sequence
1	2	5-TAATTAATAGTGCGTTGTGCTGTCTATCATGCGCCCCAGGTGCG TGGTGAAGGGACATGG CGAAGC CTGCTGCCTGCAAAACACCAAGAAATGCTGAAAAC-3
2	5	5-GAGTCGTGCTTTCTTTTCTCTTGGTACCTCAGAGCCAGCACCTG TAGCTGTTGTCTGACA GAGTTCCATCCTGACTTGTCTGCTGAGGGCCACTTCCAAAG-3
3	6	5-GCAAAGAAAGGCGGGAAAGCCGAAGGCTTGAGAAAGGGCGATC ACAGGATTAGCCAGA CACGCCCGAAAAACGCGATGAAGGCAAAGCGGCGGATGAGGAA AAGCAAAGAAAAGAGGAGGATTATCAGA-3
4	16	5-AACCAACCAGACACAGAAGTATCTCTTTGCCTTACTGTTGTGCAC GATCCCACCAAATCAG TGATAGTG ACATCTCAGATTATGAGGTTGATGATGGTATTGGCGTAGTT-3
5	20	5-AAATATTCCAGTGAGAACTGCTCTGTAATAAAGGCATCTTGGGA GGTAATGCTTGTAATGT CTGACCAAGTGTCTGGAACGTAGCAACACAAACACGCAGGAAAC AGAAAAATATATATG-3
6	21	5-TTACCTAACCAGTATTTCATCAGTAAATCTCAATACTGTTGAGTTA AATCACTCGTGGTGGA

		GGGAAATGTCCTGTCTAGTCACTGATTTGGTCTTAGTATGTGCA GGCA-3
7	23	5- TCTTGTTCACTGGGCAAACAGGGGTAGATGGTCCCCCTCCCTAG ATAGACGGTGACCTC CTAGTCCCAGGATTCAAATCCAGCATGCGTCTCCGGAGAATG-3
8	24	5- ACACCAAGCCTACCTTTCTGCATCAGAGGCAGTGCCTTTCCTAG TGCTTCTGTATCGAAG ATCTTTCAGACTTTCTGGAGTGCCTGTGGAATGAAATGTTA-3
9	25	5- AAGATCTTTTTTGGCCCTAATGTTTTAGGGTTCTCCCAACATGTC TTTCTGGACGAGGACA CGCAGCCCCAAGAGCAACTGATCAGCCAGTCATTAGGGGA-3
10	28	5- CTCAGATTGCTCTGACATAAAGCTTGTGCTGCTGAGGCGTGAGG CACTGCTGGTTCGCG AGATGGACGAAACATCACTGACATCACTATCTGATGATTTGGCA GAGACGTTATCACAGCTTCTGTACTGAT-3

6.1.10 Devices

Device	**Supplier**
BX51 upright microscope	Olympus(Tokyo, Japan)
CentrifugeS424	Eppendorf (Hamburg, Germany
C100 Automated Cell Counter	RWD (Shenzhen, China)
Contrast microscope Eclipse Ts2	Nikon (Tokyo, Japan)
ddPCR System QX200	BioRad (Hercules, USA)
Digidata 1440 digitizer	Molecular Devices (San Jose, USA)
Droplet Generator QX200	BioRad (Hercules, USA)
Electrophoresis power supply	BioRad (Hercules, USA)
Electrophoresis chamber	BioRad (Hercules, USA)
HERA cell 240i CO2 incubator	Thermo Fisher Scientific (Carlsbad, USA)
Maestro Pro Plate Reader	Axion Biosystems (Atlanta, USA)
Multiclamp700Bamplifier	Molecular Devices (San Jose, USA)
NP80 Nano photometer	Implen (Munich, Germany)
ODYSSEY CLx Imaging System	LI-COR Biosciences (Lincoln, USA)
PC-100 Pipette Puller	Narshige (Tokyo, Japan)
qPCR System 7500	AB / Thermo (Carlsbad, USA)
T100ThermalCycler	BioRad (Hercules, USA)
TCS SP8 confocal microscope	Leica (Oberkochen, Germany)
TCS SP8 confocal/STED microscope	Leica (Oberkochen, Germany)
TEM JEJ1400	JEOL (Tokyo, Japan)
TEM Tecnai F20	FEI (Oregon, USA)
Ultracentrifuge Optima L-100K	Beckman Coulter (California, USA)

6.1.11 Consumables

Material	Supplier
6-well tissue culture plates	Thermo Fisher Scientific (Carlsbad, USA)
12-well tissue culture plates	Corning Inc. (Corning, USA)
24-wel tissue culture plates	Corning Inc. (Corning, USA)
35mm glass bottom dish	Ibidi (Gräfelfing, Germany)
48-well tissue culture plates	Corning Inc. (Corning, USA)
Bacteria culture tubes	VWRInternational (Radnor, PA, USA)
Cell culture dish (10 cm)	Thermo Fisher Scientific (Carlsbad, USA)
Cell culture dish (15 cm)	Greiner Bio-One (Kremsmünster, Austria)
DNA Clean & Concentrator-5	Zymo Research(Freiburg, Germany)
Glass coverslips #1.5 (12 mm)	neoLab (Heidleberg,Germany)
Glass pipettes	(Worlds Precision Instruments (Sarasota, USA)
Glass slides Fisherbrand Superfrost	Thermo Fisher Scientific (Carlsbad, USA)
MEA plates (48 wells)	Axion Biosystems (Atlanta, USA)
Microcentrifugation tubes (1.5 mL)	Thermo Fisher Scientific (Carlsbad, USA)
Microcentrifugation tubes (2.0 mL)	Eppendorf (Hamburg, Germany)
Millex syringe filters (45 µm)	Merck (Darmstadt, Germany)
Mounting media Aquapolymount	Polysciences (Warrington, USA)
Nitrocellulose membrane	Thermo Fisher Scientific (Carlsbad, USA)
Mini-PROTEAN TGX gel	BioRad (Hercules, USA)
Parafilm	Merck (Darmstadt, Germany)
PCR tubes	Merck (Darmstadt, Germany
Plasmid Midiprep ZymoPURE II	Zymo Research (Freiburg, Germany)
Plasmid Miniprep ZymoPURE II	Zymo Research (Freiburg, Germany)
Quick-DNA Microprep Kit	Zymo Research (Freiburg, Germany)
Quick-RNA Microprep Kit	Zymo Research (Freiburg, Germany)
Petri dishes	Greiner Bio-One (Kremsmünster, Austria)
qPCR 96-well plate	AB / Thermo (Carlsbad, USA)
qPCR 96-well plate seals	AB / Thermo (Carlsbad, USA)
T75 Culture Flasks	Corning Inc. (Corning, USA)
Ultracentrifuge 35mL Tubes	Seton (California, USA)
Zymoclean Gel DNA Recovery Kit	Zymo Research (Freiburg, Germany)

6.1.12 Software

Software	Supplier
7500 Software v2.3	Thermo Fisher Scientific (Carlsbad, USA)
Adobe Illustrator CC 2019	Adobe (San José, USA)
AxisNavigator (version 3.5.2)	Axion Biosystems (Atlanta, USA)
Fiji ImageJ (version 1.53t)	NIH (Maryland, USA)
GraphPad Prism 9	GraphPad Software (San Diego, USA)
IgorPro (version 6.3.7.2)	Wavemetrics (Tigard, USA)
Image Studio Lite (version 5.2.5)	LI-COR Biosciences (Lincoln, USA)

IMOD 4.11	University of Colorado(Colorado, USA)
Leica Application Suite X	Leica (Wetzlar, Germany)
MATLAB	MathWorks (Natick, USA)
Microsoft Office	Microsoft Corporation (Redmond, USA)
Neural Metric Tool	Axion Biosystems (Atlanta, USA)
Patchmaster 10 software	HEKA (Lambrecht, Germany)
QuantaSoft Analysis Pro	BioRad(Hercules, USA)
RStudio (version 4.0.2)	RStudio (Boston, USA)
YASARA (version 29.9.23)	CMBI(Nijmegen, Netherlands)

6.2 Methods

6.2.1 Cell lines

Human embryonic H1 stem cells (WA01) and derived targeted clones were cultured on matrigel-coated dishes in mTeSR plus medium at 37 °C with 5% CO2. Cells were split after 3–5 d, depending on colony size, using EDTA (Sigma). Colonies were scraped off and transferred to freshly coated matrigel dishes. Medium was changed every other day.

Human embryonic kidney cells (HEK293T) were cultured on 10 cm culture dishes (Corning) in DMEM 10% FBS 1% Pen/Strep at 37 °C with 5% CO2. Cells were split after reaching 70-80% confluence using trypsin-EDTA. Medium was changed every 2 days.

Hela cells were cultured on T75 culture flasks in DMEM 10% FBS (Sigma) 1% Pen/Strep at 37 °C with 5% CO2. Cells were split after reaching 70-80% confluence using trypsin-EDTA. Medium was changed twice a week. All experiments described here, involving hESC, were approved by the Robert Koch Institute.

6.2.2 LLPS assays and FRAP

HeLa or HEK cells were seeded on 12 well plates and after 6 h were transfected using PEI with 0.8 to 1.2 µg of plasmid DNA. 24h after transfection cells were split and seeded in matrigel coated coverslips or 35 mm glass bottom dishes. After 24 h, cells were either fixed or subjected to live-cell imaging. Live imaging was performed in a Leica SP8 confocal microscope. An 488 argon laser at 100% for 100 ms was used to bleach m-Scarlet fluorescence and the 405nm laser at 100% for 200 ms was used to bleach EGFP fluorescence. Images before and after bleaching a small area containing 1-2 condensates were acquired at 1 Hz. Recordings lasted 130 seconds, 10 seconds before bleaching and 120 seconds after bleaching.

6.2.3 Virus production

Lentivirus were produced as described in [65] with slight modifications. Briefly, HETK293T cells were co-transfected with three helper plasmids (pRSV-REV, pMDLg/pRRE and vesicular stomatitis virus G protein (vsv-g) expression vector) and the lentiviral vector DNA. 15 µg of each helper plasmid and 30 µg of the lentiviral vector were transfected per 145 cm^2 of culture area using 1µg Polyethylenimine (Polysciences) per µg of DNA. Lentiviruses were harvested in the medium 24 and 48 h after transfection, pelleted by centrifugation (50,000 * g for 120 min), re-suspended in Opti-MEM, aliquoted, and frozen at -80 °C.

6.2.4 ESC targeting

Human PSCs were seeded as single cells at low density in a matrigel-coated 24-well plate. The day after, cells were transfected with a purified high fidelity Cas9, a specific synthesized sgRNA and a single stranded DNA donor template using Lipofectamine Stem. After 36 h cells were detached using accutase and seeded as single cells in at very low density in 10 cm culture dishes. A week later, colonies were picked from 10 cm plates and transferred to individual wells of 96-well plates. Colonies were grown for 1 week. Afterwards cells were harvested using accutase and 10% of the cells were transferred to a backup matrigel-coated 96-plate. The remaining cells were pelleted and used for genomic DNA extraction by ethanol precipitation.

6.2.5 Screening and Genotyping of targeted cells

Screening of targeted clones was performed as previously [96] with slight modifications. Briefly, conventional PCR was use employing a set of 4 primers. Two primers that flanked the whole exon where the intended mutation is located (flanking primers) and 2 different primers were designed to anneal over the mutation point (screening primers) either against the wild type sequence (control screening primer) or against the mutated sequence (mutant screening primer). Amplification using the mutant screening primer and a flanking primer allow the identification of targeted clones. Amplification with the control screening primer served as control and to determine whether the mutation is mono or bi –allelic. After identification of candidate clones of all zygosities, they were Sanger sequenced to confirm the PCR results.

6.2.6 Mouse glia culture

Primary mouse glial cells were prepared as previously [97] . Briefly, newborn (p0) mouse cortices were isolated and digested with papain for 20 min, cells were dissociated by trituration using a thin pipette tip, and passed through a cell strainer. Cells were then plated onto T75 flasks in DMEM supplemented with 10% FBS. Upon reaching confluence, glial cells were trypsinized and re-seeded twice to remove potential trace amounts of mouse neurons before the glia cell cultures were used for co-culture with human-induced neurons.

6.2.7 Generation of human induced neurons

Excitatory Neurons

Human induced excitatory neurons (iGluts) were generated as described previously [65] with slight modifications. Briefly wild type and mutant PSCs were dissociated using accutase (Sigma). Then were seeded as single cells in matrigel-coated 6-well plates (Corning) and simultaneously infected with rtTA and NgN2 expressing lentiviruses in mTeSR plus medium supplemented with the rho kinase inhibitor Y27632. The next day (day 0) half of the medium was replaced by DMEM/F12 supplemented with 1% N2 supplement, 1% non-essential amino acids, 10 ng/ml BDNF, 10 ng/ml NT-3, 0.2 µg/ml Laminin and 2 µg/ml Doxycycline. On day 1 medium was replaced fully adding 1µg/ml puromycin. On day 2 the cells were dissociated using accutase and seeded on matrigel-coated glass coverslips in Neurobasal-A medium supplemented with 1% B27 supplement, 1 % Glutamax, 10 ng/ml BDNF, 10 ng/ml NT-3, 2 µg/ml Doxycycline. On day 3 mouse glia was added to the induced neurons to support the synapse formation. On day 5 half of the media was changed by Neurobasal-A supplemented with 1% B27, 1% Glutamax, 2 µg/ml Doxycycline and 5% FBS to support glia viability. This media was changed once or twice a week until culture analysis.

In experiments aiming to assess evoked synaptic transmission, wild type or mutant cells were further separated into two groups. One group of cells was infected with differentiation lentivirus described above and with lentiviruses expressing Channelrhodopsin oChiEF fused to tdTomato [70] (termed ChR). Another group was infected with differentiation lentiviruses and lentiviruses to express nuclear-localized GFP. Four days later, cells were mixed at a ratio of 90/10% (90% with ChR and 10% with nGFP), re-seeded on matrigel-coated coverslips along with mouse glia and cultured as described above.

Neural Precursor cells (NSCs) derived forebrain Neurons

NSCs were generated from PSCs according to published protocols [98] with slight modifications. PSCs were split with accutase and 300-800k cells were seeded in a 6-well format. 24h after the split medium was changed to Neural Induction Medium (day 0). Medium was changed every second day. On day 7 cells were split with accutase and 3M cells were seeded in Neural Expansion Medium (NEM) supplemented with 5 µM ROCK inhibitor. These cells were considered P1 NSCs. Cells were split again when reaching 100% confluence, cell number was slowly decreased with each split until P4. From P4 onwards, cells were seeded without ROCK inhibitor and used for experiments.

NSCs maturation and differentiation into neurons was performed as described before [20] with modifications. Briefly 1M NPCs were seeded on Geltrex coated 6 well plate in Neural Expansion Media. 24h after media was replaced by Maturation Media (day 0). Medium was changed every other day until day 6. On day 6 cells were split with accutase and seeded for differentiation in Ornithin-Laminin coated coverslips in Maturation Media. 24h after seeding media was replaced by Neuronal Differentiation Media. Media was replaced every 3 days until cells reached confluence. Then cells were treated with 5µg/ml mitomycin C for 7 minutes to stop proliferation. Until analysis media was changed every 2 days using Neuronal Differentiation Media.

6.2.8 Immunofluorescence

Immunofluorescence was performed as previously [97] with slight modifications. Briefly, cultured induced neurons were washed twice with pre-warmed PBS. Fixed in ice-cold 4% PFA 4% Sucrose in PBS for 15 min at room temperature. Incubated in Glycine 0.1M NH4Cl 0.1M for 5 min. Washed three times with PBS and incubated in 0.2% Triton x-100 10% donkey serum in PBS for 1 h. Primary antibodies were applied overnight at 4 degrees inside a humid chamber. Cells were then washed three times with PBS and fluorescent-labeled secondary antibodies were incubated for 2 h at room temperature protected from light. Finally, cells were washed 2 times with PBS and once with ddH2O and mounted in slides using Aqua Poly/mount.

6.2.9 STED microscopy

STED imaging was conducted similarly as described previously [99]. Briefly. induced neurons were culture in #1.5 glass coverslips and ICC was performed as for confocal imaging, except that five PBS washing steps were done after each antibody incubation and that Alexa 488 anti-guinea pig (Thermo), STAR 580 nanobody anti-mouse (Abberior) and STAR 635P anti-rabbit were used as secondary antibodies. Image acquisition was done in a Leica SP8

Confocal/STED 3X microscope with an oil immersion 100x 1.44 numerical aperture objective and gated detectors (2-6 ns range for all 3 signals). Images were acquired from synapses rich areas of 33.2 μm^2 sampled at ~16 nm per pixel. Signal from the 488 antibody was acquired in confocal mode and signals from the 580 and the 635 antibodies were acquired in STED mode sequentially (to avoid bleed through) and using the same STED laser line (775 nm, to maximize alignment). Line accumulation (4-8x) and frame averaging (3x) were applied. Images were acquired blindly to the genotype of the samples and identical settings were used for all the samples within an experiment/batch.

For the analysis, individual “side view” synapses were manually selected considering the presence of an elongated PSD-95 signal at one edge of a cloud of Synaptophysin signal. Intensity profiles were obtained by drawing a rectangle of 1200 * 200 nm centered in and perpendicular to the PSD-95 elongated signal using an ImageJ custom macro. Intensity profiles were recorded for all 3 signals and proper alignment / orientation of the profiles was checked and corrected in R Studio. Intensity traces were obtained by averaging individual traces over the raw data values. Representative images in figures were linearly adjusted using bright and contrast identically across samples.

6.2.10 High-Pressure Freezing electron microscopy and electron tomography

iGluts were differentiated normally and re-seeded in matrigel-coated sapphire disks after puromycin selection at DIV4. After 4 weeks in culture cells were high-pressure frozen at 315 bars in a HPF device (HPM010 Baltic). Freeze substitution was performed in acetone solution supplemented with 2% osmium, 0.1% uranyl-acetate and 5% H_2O in a freeze-substitution device (AFS2) with the following program: -90°C for 1h, warm up to 20 °C at 5°C / hour. Then kept at 20°C for 1h. Afterwards the samples were embedded into epon resin and incubated at 60°C overnight. Thin (70 nm) or thick (250 nm) sections were generated with an ultra-microtome (UC7) and post-stained with Uranyless followed by lead citrate. Thick sections were also treated with a solution containing protein-A conjugated with 15nm gold particles as a fiducial marker.

TEM micrographs from thin sections were acquired in a JEM-1400 operating at 80kVand a 4k x 4k pixels digital camera TemCam F416 at 1.2 nm/pixel. For tomography, grids containing thick sections were placed in a high-tilt holder (Model 2040, Fischione Instruments) and the sample was recorded on a Tecnai F20 EM operating at 200kV using the SerialEM software package [100]. Images were taken every degree over a ±60° range on an FEI Eagle 4K x 4K CCD camera at a magnification of 19000x and a binning of 2 (pixel size 1.13 nm). The tilted

images were aligned by using the positions of the fiducial gold particles. The tomograms were generated using the R-weighted back-projection algorithm. Tomograms were displayed as slices one voxel thick, the vesicles modeled and analyzed with the IMOD software package [101].

For the analysis of TEM images from thin sections, synapses were manually segmented using the MATLAB/ImageJ routines from the program SynapsEM [102]. Segmentations were performed in a blind manner to the genotypes to be compared.

For the analysis of reconstructed tomograms, 3D models were manually generated using 3dMOD. Distances and size properties were then extracted from the models using the *mtk* and *imodinfo* IMOD programs.

6.2.11 Western blotting

Western blot was performed as described before [97]. Briefly, proteins were extracted from human neuronal cultures incubating them in RIPA buffer, supplemented with PMSF and cOmplete protease inhibitor cocktail for 20 minutes. Lysates were centrifuge at 15000 * g for 15 minutes and the supernatant containing the proteins was frozen at -80 °C.

Proteins were separated by SDS-PAGE in 4-20% pre-cast polyacrylamide gels and wet-transferred to a nitrocellulose membrane. Membranes were blocked with 5% BSA for 1 hour and primary antibodies were incubated overnight at 4 °C. After washing the membranes three times with TBST-X secondary antibodies were incubated for 2h. Membranes were imaged in an Odissey DLx.

6.2.12 Longitudinal MEA recordings

At day 3 of the differentiation iGluts were dissociated and seeded in PEI-Laminin-coated 48-well Lumos MEA plates. Mouse glia was added the next day. Cultures were maintained in Neurobasal-A supplemented with B27 supplement, Glutamax and 5% FBS. Cells were recorded in a Maestro Pro reader 3 times per week during 10 minutes starting from day 11. Last recording was on day 60. Data was extracted and handled using the Neural Metric Tool software or the MeaRtool R package [103].

6.2.13 Electrophysiology

General. On the day of recording, a coverslip containing induced neurons was placed in a RC-27 chamber, mounted under an Olympus upright microscope, equipped with DIC and fluorescent capabilities. Neurons were maintained at 26±1 C. Induced neurons were continuously perfused with oxygenated (95%O_2/5%CO_2) ASCF solution. Cells were

approached and patched under visual control. For all recordings, I used 3.0±0.5 Mega Ohm glass pipettes, pulled with a PC10 puller.

Voltage clamp recordings. All recordings presented in this thesis were done under whole cell voltage-clamp configuration. For this, I clamped the voltage of induced neurons at -70 mV. I used the internal solution described in the Materials section. Under these conditions, excitatory currents were detected as inward (downward) deflections. For recordings of miniature postsynaptic current recordings, tetrodotoxin 0.5 µM was added to the ACSF.

Evoked currents. In experiments where I measured evoked synaptic transmission, I recorded from GFP^+/ChR^- neurons in voltage clamp at -70 mV holding potentials. For this, cells were first identified by their GFP expression, and then approached and patched under DIC optics. Evoked currents were triggered by activation of presynaptic inputs to recorded neurons with a single, short (5 ms) pulse of blue light (488), generated via a CoolLED illumination system (pE-300) controlled by a TTL pulse. For each cell, I typically recorded evoked currents in 10 consecutive trials, separated by 1-minute intervals. This allowed me to estimate the CV of amplitude and kinetics. For estimating the amplitude of evoked currents, all trials derived from a single cell were averaged. For experiments in which EGTA sensitivity was measured, cells were incubated with 100 µM EGTA-AM or the vehicle (DMSO) during 15 minutes at 37 °C, prior to recordings.

Sucrose-evoked currents. In these experiments, cells were recorded in voltage clamp, identical to what was described above, but stimulated with hypertonic (0.5 M) sucrose solution for 5 secs. Sucrose solution was delivered in the vicinity of recorded cells (100 µm away), using a low resistance glass pipette (~1 Mega Ohms), connected to a custom pressure device (5 psi).

6.2.14 ddPCR and CNV analysis

Genomic DNA was isolated from targeted ESC clones using column purification. DNA was diluted to 5 ng/µl and frozen at -20°. ddPCR was performed using the iCS-digitalTM PSC 24-probe kit (Stem Genomics) following the manufacturer instructions. Droplets were read in a QX200 droplet reader and analysis was performed with the QuantaSoft software.

6.2.15 PCR and qPCR

Genomic DNA was extracted from cell pellets lysates using Phenol-chloroform. PCR were performed using the Mytaq kit with the following general program:

Initial denaturation	**95 °C**	**5 min**	**X 1**

Denaturation	95 °C	15 s	X 34
Annealing	59 °C	15 s	
Extension	72 °C	1 min	
Final extension	72 °C	5 min	X1

RNA was isolated from lysates using the Zymo Quick-RNA Microprep Kit following the manufacturer's instructions. Extracted RNA samples were stored at -80°C until use. cDNA synthesis was performed with the qScript cDNA SuperMix kit according to the manufacturer's guidelines. Quantitative assessment of gene expression was analyzed by qPCR, which was performed in 96-well format in the Applied Biosystems qPCR 7500 system. Per reaction, 5 µL Power SYBR Green PCR Master Mix were mixed with 2 µL nuclease-free water, 1 µL 10 µM primer mix, containing 5 µM forward and 5 µM reverse primer and 2 µL cDNA. The following PCR conditions were used:

1	50 °C	2 min	X 1
2	95 °C	2 s	
3	95 °C	15 s	X 40
4	60 °C	1 min	

6.2.16 Cloning and mutagenesis

For molecular cloning of oCHIEF, hRIMS1, EGFP and mScarlet into expression plasmids, vectors and inserts were amplified by PCR using the high fidelity kit CloneAmp and then gel purified. Fragments and vectors were cloned using In-Fusion cloning kit using a 3:1 insert: vector ratio. Afterwards 2 µl of reaction mixture were used to transform 50 µl of Stellar competent cells. Cells were plated in LB plates prepared with the corresponding antibiotic and incubated for 12-16 h. 5 - 10 colonies were amplified and plasmid DNA was extracted. Digestion and sequencing were performed to verify the correct sequence of generated vectors. Site-directed mutagenesis was performed using the QuickChange II XL Site-Directed Mutagenesis Kit following the manufacturer instructions. DNA was extracted from resistant colonies and sanger sequencing was performed to validate the proper insertion of desired mutations.

6.2.17 RIM1 molecular visualization

Alphafold's predicted RIM1 structure was downloaded from https://alphafold.ebi.ac.uk (entry Q86UR5) and loaded into YASARA software where different angle views were selected and exported as ray-traced screenshots.

6.2.18 Data analysis

Most of the data are presented as bar graphs depicting the mean values, with individual data points displayed to illustrate data distribution. Despite the large number of clones analyzed in this study, each mutation was assessed by comparing specific matched pairs of control and mutant clones (WT vs. KI, WT vs. HET, and WT vs. dKO). For this reason, statistical significance was primarily tested using an unpaired t-test. Statistical significance was indicated by stars on the top part of the plots. If no significance was found, no symbol was used.

In all experiments (except EM of missense clones, NPC-NSC differentiation experiments), each genetic condition was represented by two control (WT) and two mutant (KI, HET, or dKO) clones to increase analytical robustness and mitigate potential confounding effects arising from ESC variability (See Table 1). Final data analysis was carried out merging both clones corresponding to the same genetic condition. Individual data points typically correspond to measurements from single cells (patch-clamp), single-cell or synapse images (confocal, STED, EM), or individual wells (MEA). Data were collected from multiple cells, images, or wells obtained from independent differentiation experiments or batches (generally at least three). For Western blot and qPCR analyses, each data point represents samples collected from independent differentiation experiments.

Bibliography

1. Christopoulou, E. and C. Charrier, *Molecular mechanisms of the specialization of human synapses in the neocortex.* Curr Opin Genet Dev, 2024. **89**: p. 102258.
2. Assendorp, N., et al., *CTNND2 moderates the pace of synaptic maturation and links human evolution to synaptic neoteny.* Cell Rep, 2024. **43**(10): p. 114797.
3. Enard, W., et al., *A humanized version of Foxp2 affects cortico-basal ganglia circuits in mice.* Cell, 2009. **137**(5): p. 961-71.
4. Jorstad, N.L., et al., *Transcriptomic cytoarchitecture reveals principles of human neocortex organization.* Science, 2023. **382**(6667): p. eadf6812.
5. Keough, K.C., et al., *Three-dimensional genome rewiring in loci with human accelerated regions.* Science, 2023. **380**(6643): p. eabm1696.
6. Libe-Philippot, B., et al., *Synaptic neoteny of human cortical neurons requires species-specific balancing of SRGAP2-SYNGAP1 cross-inhibition.* Neuron, 2024. **112**(21): p. 3602-3617 e9.
7. Pak, C., et al., *Cross-platform validation of neurotransmitter release impairments in schizophrenia patient-derived NRXN1-mutant neurons.* Proc Natl Acad Sci U S A, 2021. **118**(22).
8. Jones, R.A., et al., *Cellular and Molecular Anatomy of the Human Neuromuscular Junction.* Cell Rep, 2017. **21**(9): p. 2348-2356.
9. Geschwind, D.H., *Autism: many genes, common pathways?* Cell, 2008. **135**(3): p. 391-5.
10. Parenti, I., et al., *Neurodevelopmental Disorders: From Genetics to Functional Pathways.* Trends Neurosci, 2020. **43**(8): p. 608-621.
11. Bourgeron, T., *A synaptic trek to autism.* Curr Opin Neurobiol, 2009. **19**(2): p. 231-4.
12. Ebrahimi-Fakhari, D. and M. Sahin, *Autism and the synapse: emerging mechanisms and mechanism-based therapies.* Curr Opin Neurol, 2015. **28**(2): p. 91-102.
13. Bourgeron, T., *From the genetic architecture to synaptic plasticity in autism spectrum disorder.* Nat Rev Neurosci, 2015. **16**(9): p. 551-63.
14. Huguet, G., E. Ey, and T. Bourgeron, *The genetic landscapes of autism spectrum disorders.* Annu Rev Genomics Hum Genet, 2013. **14**: p. 191-213.
15. Chung, C., W. Shin, and E. Kim, *Early and Late Corrections in Mouse Models of Autism Spectrum Disorder.* Biol Psychiatry, 2022. **91**(11): p. 934-944.
16. Zerbi, V., et al., *Brain mapping across 16 autism mouse models reveals a spectrum of functional connectivity subtypes.* Mol Psychiatry, 2021. **26**(12): p. 7610-7620.
17. Takahashi, K. and S. Yamanaka, *Induction of pluripotent stem cells from mouse embryonic and adult fibroblast cultures by defined factors.* Cell, 2006. **126**(4): p. 663-76.
18. Jopling, C., S. Boue, and J.C. Izpisua Belmonte, *Dedifferentiation, transdifferentiation and reprogramming: three routes to regeneration.* Nat Rev Mol Cell Biol, 2011. **12**(2): p. 79-89.
19. Powell, S.K., et al., *Induction of dopaminergic neurons for neuronal subtype-specific modeling of psychiatric disease risk.* Mol Psychiatry, 2023. **28**(5): p. 1970-1982.
20. Samara, A., et al., *Robust neuronal differentiation of human embryonic stem cells for neurotoxicology.* STAR Protoc, 2022. **3**(3): p. 101533.
21. Nehme, R., et al., *Combining NGN2 Programming with Developmental Patterning Generates Human Excitatory Neurons with NMDAR-Mediated Synaptic Transmission.* Cell Rep, 2018. **23**(8): p. 2509-2523.

22. Yang, N., et al., *Generation of pure GABAergic neurons by transcription factor programming.* Nat Methods, 2017. **14**(6): p. 621-628.
23. Breckwoldt, K., et al., *Differentiation of cardiomyocytes and generation of human engineered heart tissue.* Nat Protoc, 2017. **12**(6): p. 1177-1197.
24. Lim, C.S., et al., *Understanding the molecular basis of autism in a dish using hiPSCs-derived neurons from ASD patients.* Mol Brain, 2015. **8**(1): p. 57.
25. Ben-Reuven, L. and O. Reiner, *Modeling the autistic cell: iPSCs recapitulate developmental principles of syndromic and nonsyndromic ASD.* Dev Growth Differ, 2016. **58**(5): p. 481-91.
26. Marco de la Cruz, B., et al., *Liprin-alpha proteins are master regulators of human presynapse assembly.* Nat Neurosci, 2024. **27**(4): p. 629-642.
27. Kwart, D., et al., *A Large Panel of Isogenic APP and PSEN1 Mutant Human iPSC Neurons Reveals Shared Endosomal Abnormalities Mediated by APP beta-CTFs, Not Abeta.* Neuron, 2019. **104**(5): p. 1022.
28. Craig, A.M., E.R. Graf, and M.W. Linhoff, *How to build a central synapse: clues from cell culture.* Trends Neurosci, 2006. **29**(1): p. 8-20.
29. Gray, E.G., *Electron microscopy of synaptic contacts on dendrite spines of the cerebral cortex.* Nature, 1959. **183**(4675): p. 1592-3.
30. Palay, S.L., *Synapses in the central nervous system.* J Biophys Biochem Cytol, 1956. **2**(4 Suppl): p. 193-202.
31. Sudhof, T.C., *The cell biology of synapse formation.* J Cell Biol, 2021. **220**(7).
32. Sudhof, T.C., *Towards an Understanding of Synapse Formation.* Neuron, 2018. **100**(2): p. 276-293.
33. Emperador-Melero, J. and P.S. Kaeser, *Assembly of the presynaptic active zone.* Curr Opin Neurobiol, 2020. **63**: p. 95-103.
34. Sudhof, T.C., *The presynaptic active zone.* Neuron, 2012. **75**(1): p. 11-25.
35. Chou, V.T., S.A. Johnson, and D. Van Vactor, *Synapse development and maturation at the drosophila neuromuscular junction.* Neural Dev, 2020. **15**(1): p. 11.
36. Rizalar, F.S., D.A. Roosen, and V. Haucke, *A Presynaptic Perspective on Transport and Assembly Mechanisms for Synapse Formation.* Neuron, 2021. **109**(1): p. 27-41.
37. Sando, R., et al., *Assembly of Excitatory Synapses in the Absence of Glutamatergic Neurotransmission.* Neuron, 2017. **94**(2): p. 312-321 e3.
38. Deng, L., et al., *RIM proteins activate vesicle priming by reversing autoinhibitory homodimerization of Munc13.* Neuron, 2011. **69**(2): p. 317-31.
39. Kaeser, P.S., et al., *RIM proteins tether Ca2+ channels to presynaptic active zones via a direct PDZ-domain interaction.* Cell, 2011. **144**(2): p. 282-95.
40. Acuna, C., X. Liu, and T.C. Sudhof, *How to Make an Active Zone: Unexpected Universal Functional Redundancy between RIMs and RIM-BPs.* Neuron, 2016. **91**(4): p. 792-807.
41. Wang, S.S.H., et al., *Fusion Competent Synaptic Vesicles Persist upon Active Zone Disruption and Loss of Vesicle Docking.* Neuron, 2016. **91**(4): p. 777-791.
42. Patel, M.R., et al., *Hierarchical assembly of presynaptic components in defined C. elegans synapses.* Nat Neurosci, 2006. **9**(12): p. 1488-98.
43. Chen, X., et al., *Phase separation at the synapse.* Nat Neurosci, 2020. **23**(3): p. 301-310.
44. McDonald, N.A., R.D. Fetter, and K. Shen, *Assembly of synaptic active zones requires phase separation of scaffold molecules.* Nature, 2020. **588**(7838): p. 454-458.
45. Qiu, H., et al., *Short-distance vesicle transport via phase separation.* Cell, 2024. **187**(9): p. 2175-2193 e21.

46. Tang, A.H., et al., *A trans-synaptic nanocolumn aligns neurotransmitter release to receptors.* Nature, 2016. **536**(7615): p. 210-4.
47. Wang, Y., et al., *Rim is a putative Rab3 effector in regulating synaptic-vesicle fusion.* Nature, 1997. **388**(6642): p. 593-8.
48. Kaeser, P.S. and T.C. Sudhof, *RIM function in short- and long-term synaptic plasticity.* Biochem Soc Trans, 2005. **33**(Pt 6): p. 1345-9.
49. Wang, Y., S. Sugita, and T.C. Sudhof, *The RIM/NIM family of neuronal C2 domain proteins. Interactions with Rab3 and a new class of Src homology 3 domain proteins.* J Biol Chem, 2000. **275**(26): p. 20033-44.
50. de Jong, A.P.H., et al., *RIM C(2)B Domains Target Presynaptic Active Zone Functions to PIP(2)-Containing Membranes.* Neuron, 2018. **98**(2): p. 335-349 e7.
51. Dong, S., et al., *De novo insertions and deletions of predominantly paternal origin are associated with autism spectrum disorder.* Cell Rep, 2014. **9**(1): p. 16-23.
52. Guo, H., et al., *Inherited and multiple de novo mutations in autism/developmental delay risk genes suggest a multifactorial model.* Mol Autism, 2018. **9**: p. 64.
53. Iossifov, I., et al., *De novo gene disruptions in children on the autistic spectrum.* Neuron, 2012. **74**(2): p. 285-99.
54. Wang, T., et al., *De novo genic mutations among a Chinese autism spectrum disorder cohort.* Nat Commun, 2016. **7**: p. 13316.
55. Krumm, N., et al., *Excess of rare, inherited truncating mutations in autism.* Nat Genet, 2015. **47**(6): p. 582-8.
56. Rolland, T., et al., *Phenotypic effects of genetic variants associated with autism.* Nat Med, 2023. **29**(7): p. 1671-1680.
57. Krupp, D.R., et al., *Exonic Mosaic Mutations Contribute Risk for Autism Spectrum Disorder.* Am J Hum Genet, 2017. **101**(3): p. 369-390.
58. Lipstein, N., et al., *Synaptic UNC13A protein variant causes increased neurotransmission and dyskinetic movement disorder.* J Clin Invest, 2017. **127**(3): p. 1005-1018.
59. RK, C.Y., et al., *Whole genome sequencing resource identifies 18 new candidate genes for autism spectrum disorder.* Nat Neurosci, 2017. **20**(4): p. 602-611.
60. Satterstrom, F.K., et al., *Large-Scale Exome Sequencing Study Implicates Both Developmental and Functional Changes in the Neurobiology of Autism.* Cell, 2020. **180**(3): p. 568-584 e23.
61. Kim, S.W., et al., *Whole genome sequencing analysis identifies sex differences of familial pattern contributing to phenotypic diversity in autism.* Genome Med, 2024. **16**(1): p. 114.
62. Zhou, X., et al., *Integrating de novo and inherited variants in 42,607 autism cases identifies mutations in new moderate-risk genes.* Nat Genet, 2022. **54**(9): p. 1305-1319.
63. Bozdagi, O., et al., *Haploinsufficiency of the autism-associated Shank3 gene leads to deficits in synaptic function, social interaction, and social communication.* Mol Autism, 2010. **1**(1): p. 15.
64. Bonsi, P., et al., *Postsynaptic autism spectrum disorder genes and synaptic dysfunction.* Neurobiol Dis, 2022. **162**: p. 105564.
65. Zhang, Y., et al., *Rapid single-step induction of functional neurons from human pluripotent stem cells.* Neuron, 2013. **78**(5): p. 785-98.
66. Gracheva, E.O., et al., *Direct interactions between C. elegans RAB-3 and Rim provide a mechanism to target vesicles to the presynaptic density.* Neurosci Lett, 2008. **444**(2): p. 137-42.
67. Kaeser, P.S., et al., *RIM1alpha and RIM1beta are synthesized from distinct promoters of the RIM1 gene to mediate differential but overlapping synaptic functions.* J Neurosci, 2008. **28**(50): p. 13435-47.
68. Muller, M., et al., *RIM controls homeostatic plasticity through modulation of the readily-releasable vesicle pool.* J Neurosci, 2012. **32**(47): p. 16574-85.

69. Petzoldt, A.G., et al., *RIM-binding protein couples synaptic vesicle recruitment to release sites.* J Cell Biol, 2020. **219**(7).
70. Lin, J.Y., et al., *Characterization of engineered channelrhodopsin variants with improved properties and kinetics.* Biophys J, 2009. **96**(5): p. 1803-14.
71. Eggermann, E., et al., *Nanodomain coupling between Ca(2)(+) channels and sensors of exocytosis at fast mammalian synapses.* Nat Rev Neurosci, 2011. **13**(1): p. 7-21.
72. Imig, C., et al., *Ultrastructural Imaging of Activity-Dependent Synaptic Membrane-Trafficking Events in Cultured Brain Slices.* Neuron, 2020. **108**(5): p. 843-860 e8.
73. Rosenmund, C. and C.F. Stevens, *Definition of the readily releasable pool of vesicles at hippocampal synapses.* Neuron, 1996. **16**(6): p. 1197-207.
74. Assou, S., et al., *Recurrent Genetic Abnormalities in Human Pluripotent Stem Cells: Definition and Routine Detection in Culture Supernatant by Targeted Droplet Digital PCR.* Stem Cell Reports, 2020. **14**(1): p. 1-8.
75. Jin, G., et al., *Liprin-α/RIM complex regulates the dynamic assembly of presynaptic active zones via liquid-liquid phase separation.* 2024: p. 2024.08.29.610253.
76. Emperador-Melero, J., et al., *Distinct active zone protein machineries mediate Ca(2+) channel clustering and vesicle priming at hippocampal synapses.* Nat Neurosci, 2024. **27**(9): p. 1680-1694.
77. Jaffrey, S.R. and M.F. Wilkinson, *Nonsense-mediated RNA decay in the brain: emerging modulator of neural development and disease.* Nat Rev Neurosci, 2018. **19**(12): p. 715-728.
78. Kupferschmidt, D.A., et al., *Active Zone Proteins RIM1alphabeta Are Required for Normal Corticostriatal Transmission and Action Control.* J Neurosci, 2019. **39**(8): p. 1457-1470.
79. Schoch, S., et al., *RIM1alpha forms a protein scaffold for regulating neurotransmitter release at the active zone.* Nature, 2002. **415**(6869): p. 321-6.
80. Kovacevic, J., et al., *Protein instability, haploinsufficiency, and cortical hyper-excitability underlie STXBP1 encephalopathy.* Brain, 2018. **141**(5): p. 1350-1374.
81. Patel, P.A., et al., *Haploinsufficiency of X-linked intellectual disability gene CASK induces post-transcriptional changes in synaptic and cellular metabolic pathways.* Exp Neurol, 2020. **329**: p. 113319.
82. Nakamura, Y., et al., *Nanoscale distribution of presynaptic Ca(2+) channels and its impact on vesicular release during development.* Neuron, 2015. **85**(1): p. 145-158.
83. Stanley, E.F., *Single calcium channels and acetylcholine release at a presynaptic nerve terminal.* Neuron, 1993. **11**(6): p. 1007-11.
84. Sakamoto, H., et al., *Synaptic weight set by Munc13-1 supramolecular assemblies.* Nat Neurosci, 2018. **21**(1): p. 41-49.
85. Kiyonaka, S., et al., *RIM1 confers sustained activity and neurotransmitter vesicle anchoring to presynaptic Ca2+ channels.* Nat Neurosci, 2007. **10**(6): p. 691-701.
86. Acuna, C., et al., *RIM-BPs Mediate Tight Coupling of Action Potentials to Ca(2+)-Triggered Neurotransmitter Release.* Neuron, 2015. **87**(6): p. 1234-1247.
87. Chanda, S., et al., *Direct Reprogramming of Human Neurons Identifies MARCKSL1 as a Pathogenic Mediator of Valproic Acid-Induced Teratogenicity.* Cell Stem Cell, 2019. **25**(1): p. 103-119 e6.
88. Schmidt, R., et al., *MINFLUX nanometer-scale 3D imaging and microsecond-range tracking on a common fluorescence microscope.* Nat Commun, 2021. **12**(1): p. 1478.
89. Strauss, S. and R. Jungmann, *Up to 100-fold speed-up and multiplexing in optimized DNA-PAINT.* Nat Methods, 2020. **17**(8): p. 789-791.
90. Wu, X., et al., *RIM and RIM-BP Form Presynaptic Active-Zone-like Condensates via Phase Separation.* Mol Cell, 2019. **73**(5): p. 971-984 e5.

91. Guzikowski, N.J. and E.T. Kavalali, *Functional specificity of liquid-liquid phase separation at the synapse.* Nat Commun, 2024. **15**(1): p. 10103.
92. Ko, J., et al., *LRRTM2 functions as a neurexin ligand in promoting excitatory synapse formation.* Neuron, 2009. **64**(6): p. 791-8.
93. Etherton, M.R., et al., *Mouse neurexin-1alpha deletion causes correlated electrophysiological and behavioral changes consistent with cognitive impairments.* Proc Natl Acad Sci U S A, 2009. **106**(42): p. 17998-8003.
94. Chen, L.Y., et al., *Conditional Deletion of All Neurexins Defines Diversity of Essential Synaptic Organizer Functions for Neurexins.* Neuron, 2017. **94**(3): p. 611-625 e4.
95. Luo, F., et al., *Neurexins regulate presynaptic GABA(B)-receptors at central synapses.* Nat Commun, 2021. **12**(1): p. 2380.
96. Kwart, D., et al., *Precise and efficient scarless genome editing in stem cells using CORRECT.* Nat Protoc, 2017. **12**(2): p. 329-354.
97. Patzke, C., et al., *Neuromodulator Signaling Bidirectionally Controls Vesicle Numbers in Human Synapses.* Cell, 2019. **179**(2): p. 498-513 e22.
98. Yan, Y., et al., *Efficient and rapid derivation of primitive neural stem cells and generation of brain subtype neurons from human pluripotent stem cells.* Stem Cells Transl Med, 2013. **2**(11): p. 862-70.
99. Tan, C., et al., *Rebuilding essential active zone functions within a synapse.* Neuron, 2022. **110**(9): p. 1498-1515 e8.
100. Mastronarde, D.N., *Automated electron microscope tomography using robust prediction of specimen movements.* J Struct Biol, 2005. **152**(1): p. 36-51.
101. Kremer, J.R., D.N. Mastronarde, and J.R. McIntosh, *Computer visualization of three-dimensional image data using IMOD.* J Struct Biol, 1996. **116**(1): p. 71-6.
102. Watanabe, S., et al., *SynapsEM: Computer-Assisted Synapse Morphometry.* Front Synaptic Neurosci, 2020. **12**: p. 584549.
103. Gelfman, S., et al., *meaRtools: An R package for the analysis of neuronal networks recorded on microelectrode arrays.* PLoS Comput Biol, 2018. **14**(10): p. e1006506.

List of Publications

Gaowei Jin*, **Joaquín Campos***, Yang Liu, Berta Marcó de la Cruz, Shujing Zhang, Mingfu Liang, Kaiyue Li, Xingqiao Xie, Cong Yu, Fredrik H. Sterky, Claudio Acuna, Zhiyi Wei. **Liprin-α/RIM complex regulates the dynamic assembly of presynaptic active zones via liquid-liquid phase separation.** 2025. *In Revision at PLOS Biology*

Tetzlaff SK, Reyhan E, Layer N, Bengtson CP, Heuer A, Schroers J, Faymonville AJ, Langeroudi AP, Drewa N, Keifert E, Wagner J, Soyka SJ, Schubert MC, Sivapalan N, Pramatarov RL, Buchert V, Wageringel T, Grabis E, Wißmann N, Alhalabi OT, Botz M, Bojcevski J, **Campos J**, Boztepe B, Scheck JG, Conic SH, Puschhof MC, Villa G, Drexler R, Zghaibeh Y, Hausmann F, Hänzelmann S, Karreman MA, Kurz FT, Schröter M, Thier M, Suwala AK, Forsberg-Nilsson K, Acuna C, Saez-Rodriguez J, Abdollahi A, Sahm F, Breckwoldt MO, Suchorska B, Ricklefs FL, Heiland DH, Venkataramani V. **Characterizing and targeting glioblastoma neuron-tumor networks with retrograde tracing**. *Cell*. 2025 Jan 23;188(2):390-411.

Marcó de la Cruz B*, **Campos J***, Molinaro A, Xie X, Jin G, Wei Z, Acuna C, Sterky FH. **Liprin-α proteins are master regulators of human presynapse assembly**. *Nat Neurosci*. 2024 Apr;27(4):629-642.

Campos J, Gleitze S, Hidalgo C, Núñez MT. **IP_3R-Mediated Calcium Release Promotes Ferroptotic Death in SH-SY5Y Neuroblastoma Cells.** *Antioxidants* (Basel). 2024 Feb 4;13(2):196.

Weigel B, Tegethoff JF, Grieder SD, Lim B, Nagarajan B, Liu YC, Truberg J, Papageorgiou D, Adrian-Segarra JM, Schmidt LK, Kaspar J, Poisel E, Heinzelmann E, Saraswat M, Christ M, Arnold C, Ibarra IL, **Campos J**, Krijgsveld J, Monyer H, Zaugg JB, Acuna C, Mall M**. MYT1L haploinsufficiency in human neurons and mice causes autism-associated phenotypes that can be reversed by genetic and pharmacologic intervention.** *Mol Psychiatry*. 2023 May;28(5):2122-2135.

Koch J, Xin Q, Obr M, Schäfer A, Rolfs N, Anagho HA, Kudulyte A, Woltereck L, Kummer S, **Campos J**, Uckeley ZM, Bell-Sakyi L, Kräusslich HG, Schur FK, Acuna C, Lozach PY. The phenuivirus **Toscana virus makes an atypical use of vacuolar acidity to enter host cells**. *PLoS Pathog*. 2023 Aug 14;19(8):e1011562.

Kapell H, Fazio L, Dyckow J, Schwarz S, Cruz-Herranz A, Mayer C, **Campos J**, D'Este E, Möbius W, Cordano C, Pröbstel AK, Gharagozloo M, Zulji A, Narayanan Naik V, Delank A, Cerina M, Müntefering T, Lerma-Martin C, Sonner JK, Sin JH, Disse P, Rychlik N, Sabeur K, Chavali M, Srivastava R, Heidenreich M, Fitzgerald KC, Seebohm G, Stadelmann C, Hemmer B, Platten M, Jentsch TJ, Engelhardt M, Budde T, Nave KA, Calabresi PA, Friese MA, Green AJ, Acuna C, Rowitch DH, Meuth SG, Schirmer L. **Neuron-oligodendrocyte potassium shuttling at nodes of Ranvier protects against inflammatory demyelination**. *J Clin Invest*. 2023 Apr 3;133(7): e164223.

Mencacci NE, Brockmann MM, Dai J, Pajusalu S, Atasu B, **Campos J**, Pino G, Gonzalez-Latapi P, Patzke C, Schwake M, Tucci A, Pittman A, Simon-Sanchez J, Carvill GL, Balint B, Wiethoff S, Warner TT, Papandreou A, Soo A, Rein R, Kadastik-Eerme L, Puusepp S, Reinson K, Tomberg T, Hanagasi H, Gasser T, Bhatia KP, Kurian MA, Lohmann E, Õunap K, Rosenmund C, Südhof TC, Wood NW, Krainc D, Acuna C. **Biallelic variants in TSPOAP1, encoding the active-zone protein RIMBP1, cause autosomal recessive dystonia.** *J Clin Invest*. 2021 Apr 1;131(7): e140625.

Kamm GB, Boffi JC, Zuza K, Nencini S, **Campos J**, Schrenk-Siemens K, Sonntag I, Kabaoğlu B, El Hay MYA, Schwarz Y, Tappe-Theodor A, Bruns D, Acuna C, Kuner T, Siemens J. **A synaptic temperature sensor for body cooling**. *Neuron*. 2021 Oct 20;109(20):3283-3297.

*Co-first auth

Supplementary Figures

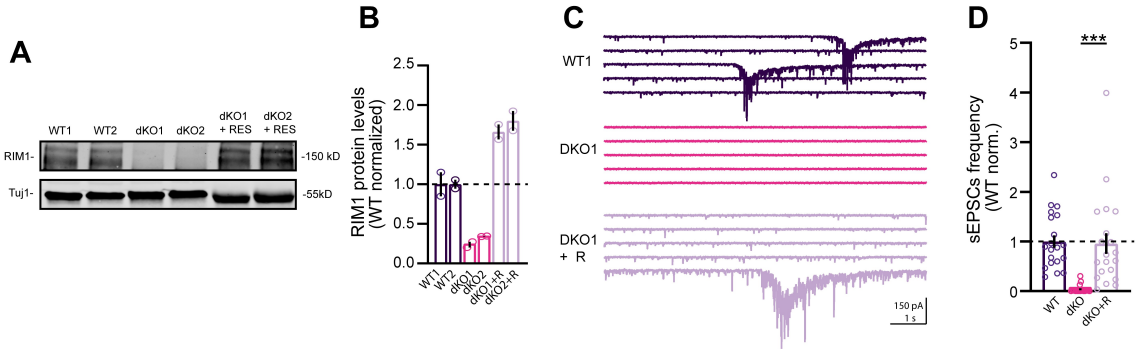

Figure S1. RIM1/2 double knock out physiologic phenotype is greatly rescued by RIM1 only re-expression. Representative western blot of WT, dKO, and dKO iGluts over-expressing RIM1 samples (A). Quantification of RIM1/2 protein levels for each clone (B). Representative traces of patch clamp recordings from WT, dKO and dKO rescued iGluts (C). Quantification of spontaneous EPSC frequency (D). Bar plots indicate the mean of the data. Error bars = SEM. N = 1/10 (batches/cells). Unpaired t-test. *** $p < 0.001$.

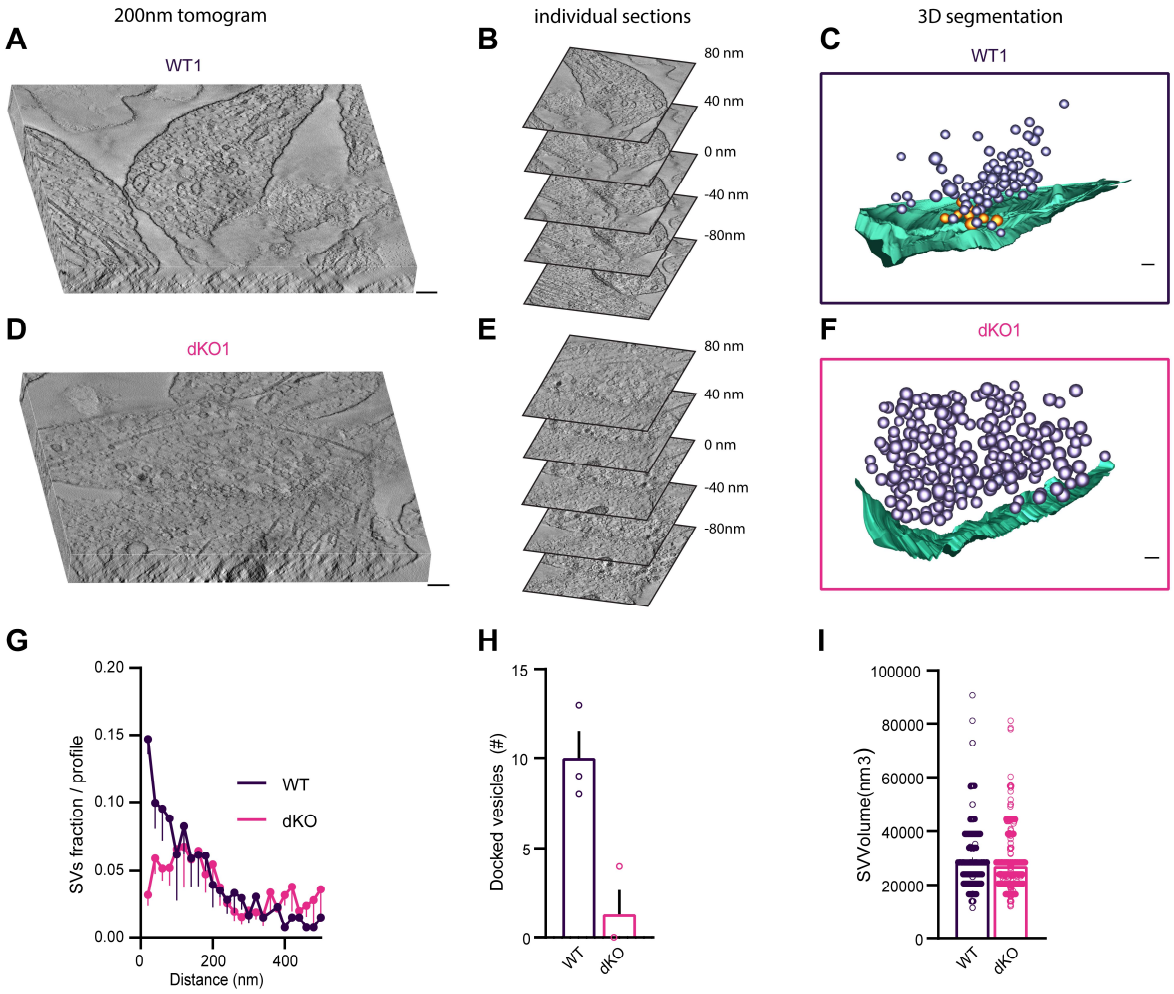

Figure S2. Electron tomography reveals a dramatic reduction of docked synaptic vesicles in RIM1/2 dKO iGluts. A 200 nm reconstituted tomogram of a RIM1/2 WT (A) and RIM1/2 dKO (D) synapses. Scale bars = 100 nm. Individual sections of the reconstituted tomograms at different heights for WT (B) and dKO (E) synapses are shown. Manual segmentations of the presynaptic membrane and SVs for WT (C) and dKO (F) synapses are presented (SVs contacting the membrane a shown in orange). Scale bars = 40 nm. Quantification of SVs as function of distance from the active zone membrane (G). Quantification of the number of docked vesicles(H). Quantification of SV volume(I). Bar plots indicate the mean of the data. Error bars = SEM. N = 3/2 (WT/dKO tomograms).

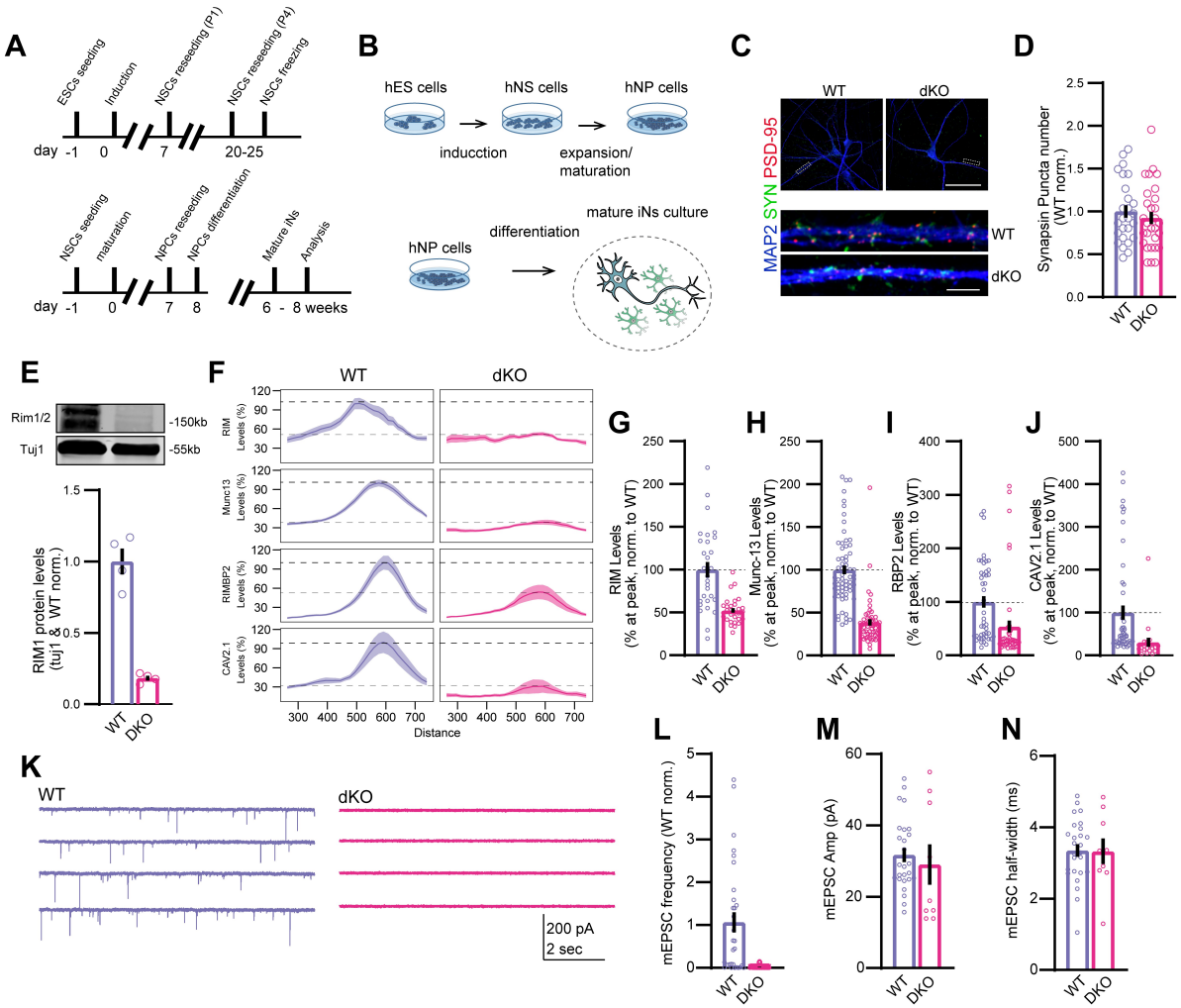

Figure S3. NSC-NPC-neuronal differentiation using small molecules and growth factors preserves RIM1/2 double knockout phenotypes observed in NGN2-induced differentiation. Schematic timeline of the two-step protocol for generating human iGluts using small molecules and growth factors. First, NSCs are generated, passaged three times, and subsequently stored. Starting from NSCs, an enriched NPC culture is produced, which is then used for neuronal differentiation(A). Diagram of the two-step differentiation protocol for iN generation (B). Confocal images of human iGluts derived from NPC differentiation, stained for MAP2, Synapsin, and PSD-95 (C). Scale bars: Low magnification = 50 µm; cropped regions = 5 µm. Quantification of Synapsin puncta number (D). Representative Western blot showing RIM1/2 expression in RIM1/2 WT and RIM1/2 dKO iGluts, along with quantification of RIM1/2 protein levels (E). Quantification of synaptic levels of RIM1, Munc13, RIMBP2, and CAV2.1 using STED microscopy (F). Quantification of maximum synaptic intensity levels for RIM1 (G), Munc13 (H), RIMBP2 (I), and CAV2.1 (J). (K) Representative mEPSC traces for RIM1/2 WT and RIM1/2 dKO iGluts, with quantification of mEPSC frequency (L), amplitude (M), and half-width (N). Bar plots indicate the mean of the data. Error bars = SEM. Sample sizes: N=26−29/1. N=26−29/1 (cells/batches for panels C & D), N=20−64/1. N=20−64/1 (profiles/batches for panels F–J). N=30/1 (cells/batches for panels K–N). NSC-NPC neuronal differentiations were performed by Dorothea Schall.

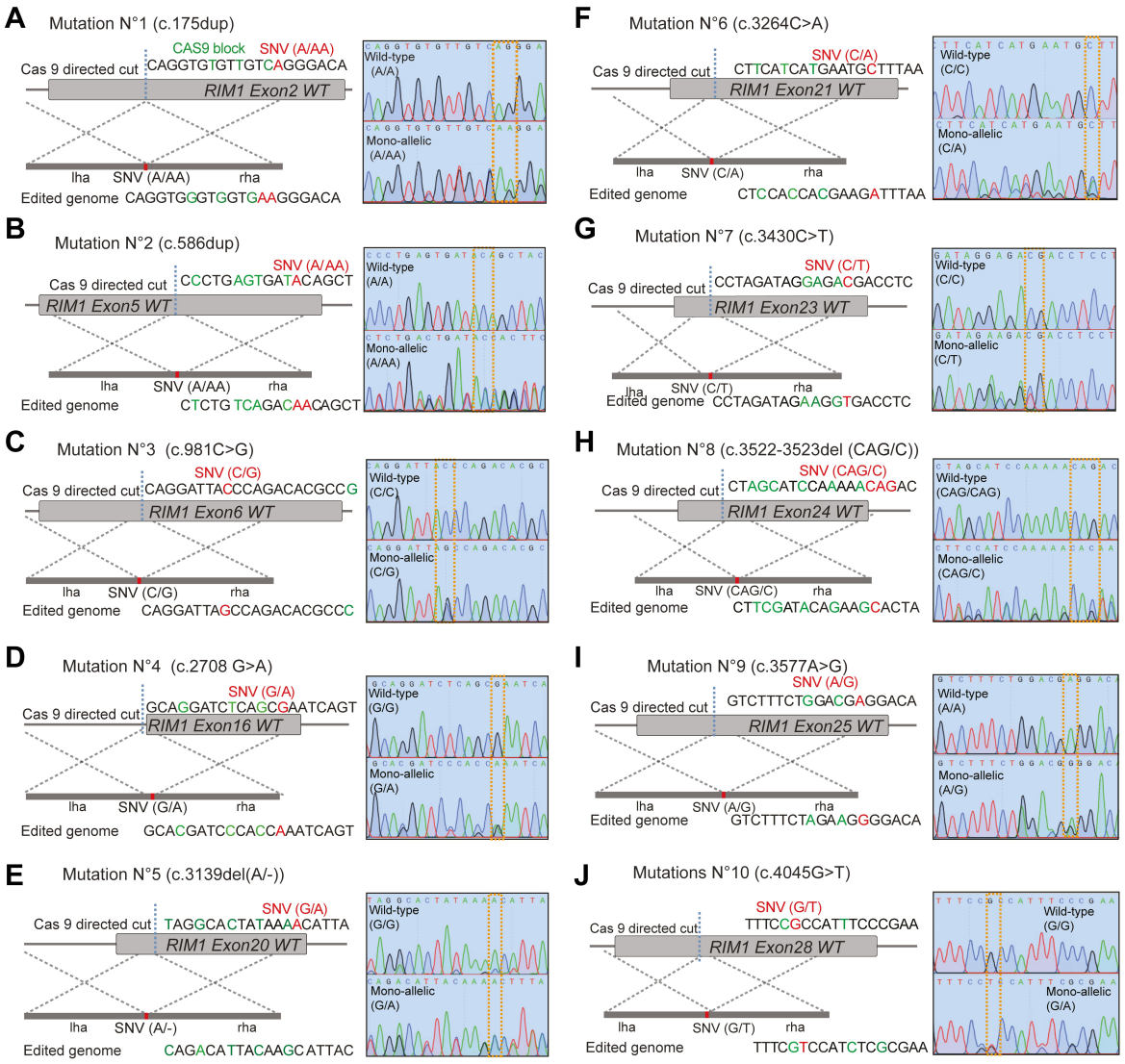

Figure S4. Strategies and WT and KI clones resulting chromatograms of RIM1 ASD-linked mutations targeting. (Left) Schematic of RIM1-exon 2 targeting strategy to introduce mutation c.175dup (Arg59Fs). (right) Chromatograms of wild-type and mono-allelic knock-in isolated clones. B-J, same for remaining mutations. SNV single nucleotide variant. Lha, left homology arm. Rha, right homology arm.

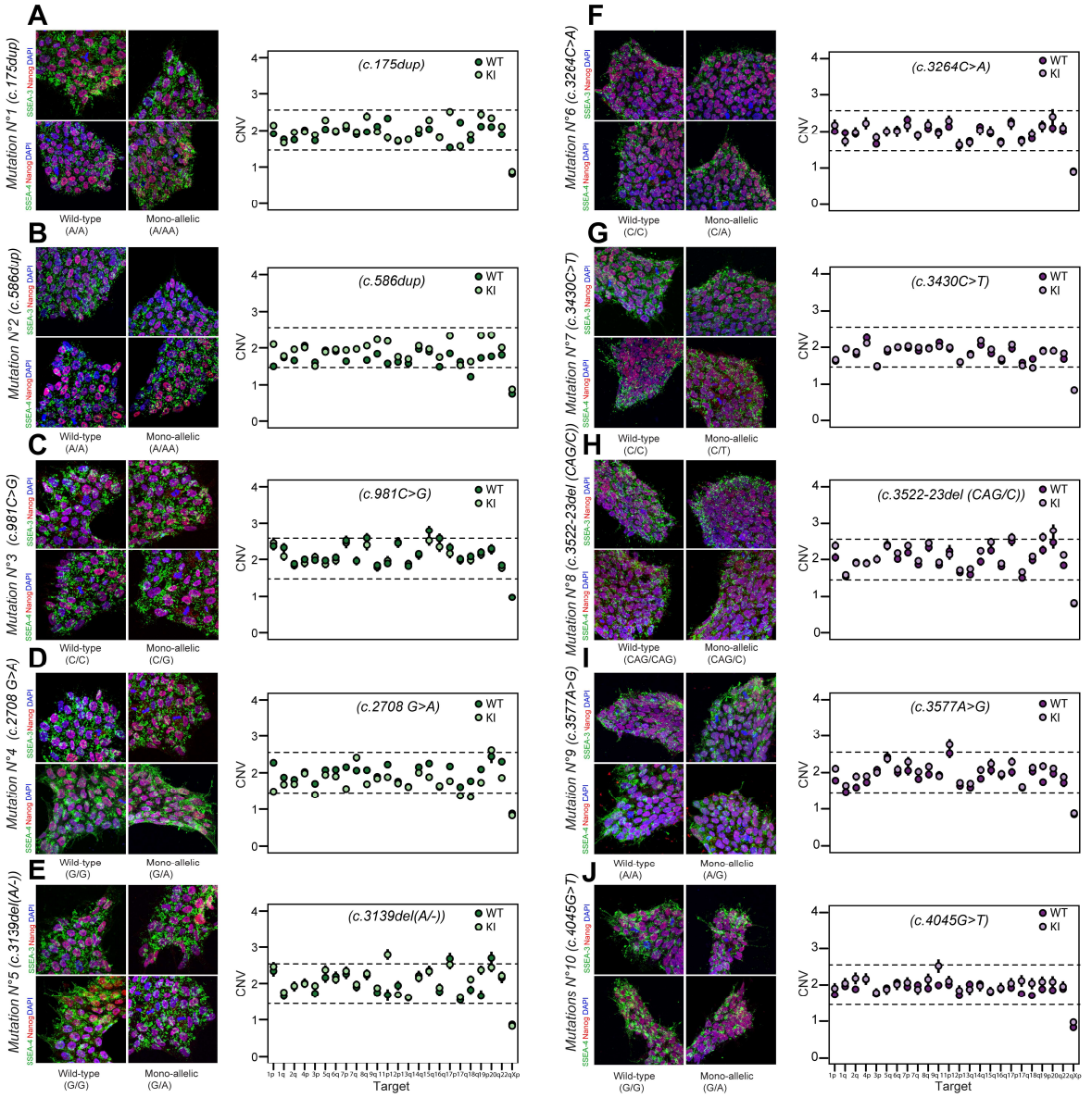

Figure S5. Validation of RIM1 ASD-linked mutation-targeted ESC lines. Wild-type (WT) and knock-in (KI) ESC lines were validated for the expression of stem cell markers and assessed for normal copy number variation (CNV) at 24 hotspots to ensure genomic stability. (left) Confocal images of PSCs targeted at RIM1 exon 2 to introduce the mutation c.175dup (Arg59Fs), stained for SSEA-3, Nanog, and DAPI, or SSEA-4, Nanog and DAPI. (right) CNV analysis of WT and KI ESC clones targeted at RIM1 exon 2 with mutation c.175dup (A). B-J, same for indicated RIM1 ASD mutations.

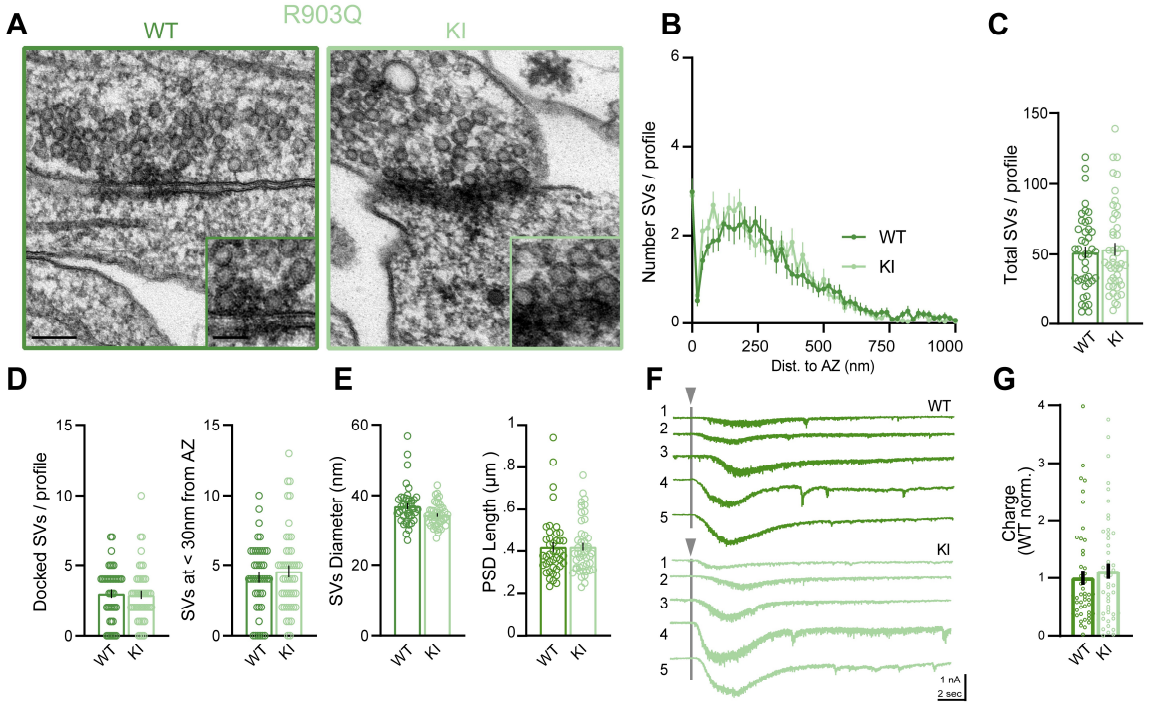

Figure S6. Normal synaptic ultrastructure in RIM1 R903Q knock-in iGluts. Representative electron microscope images of high-pressure frozen RIM1 WT and RIM1 R903Q KI iGluts (A). Quantification of the number of SVs per profile as a function of their distance from the AZ (B). Quantification of the total number of SVs per profile (C). Quantification of the number of docked SVs per profile. and of the number of SVs located within 30 nm of the AZ (D). Quantification of SV diameters and PSD length (E). Scale bars: 400 nm in main panels; 100 nm in insets 42-47/1 (profiles/batches). Schematics depicting recording setup for RRP and representative sucrose evoked current traces (F). Quantification of sucrose evoked total charge (G). N = 48/2 (cells/batches). Bar plots indicate the mean of the data. Error bars = SEM.

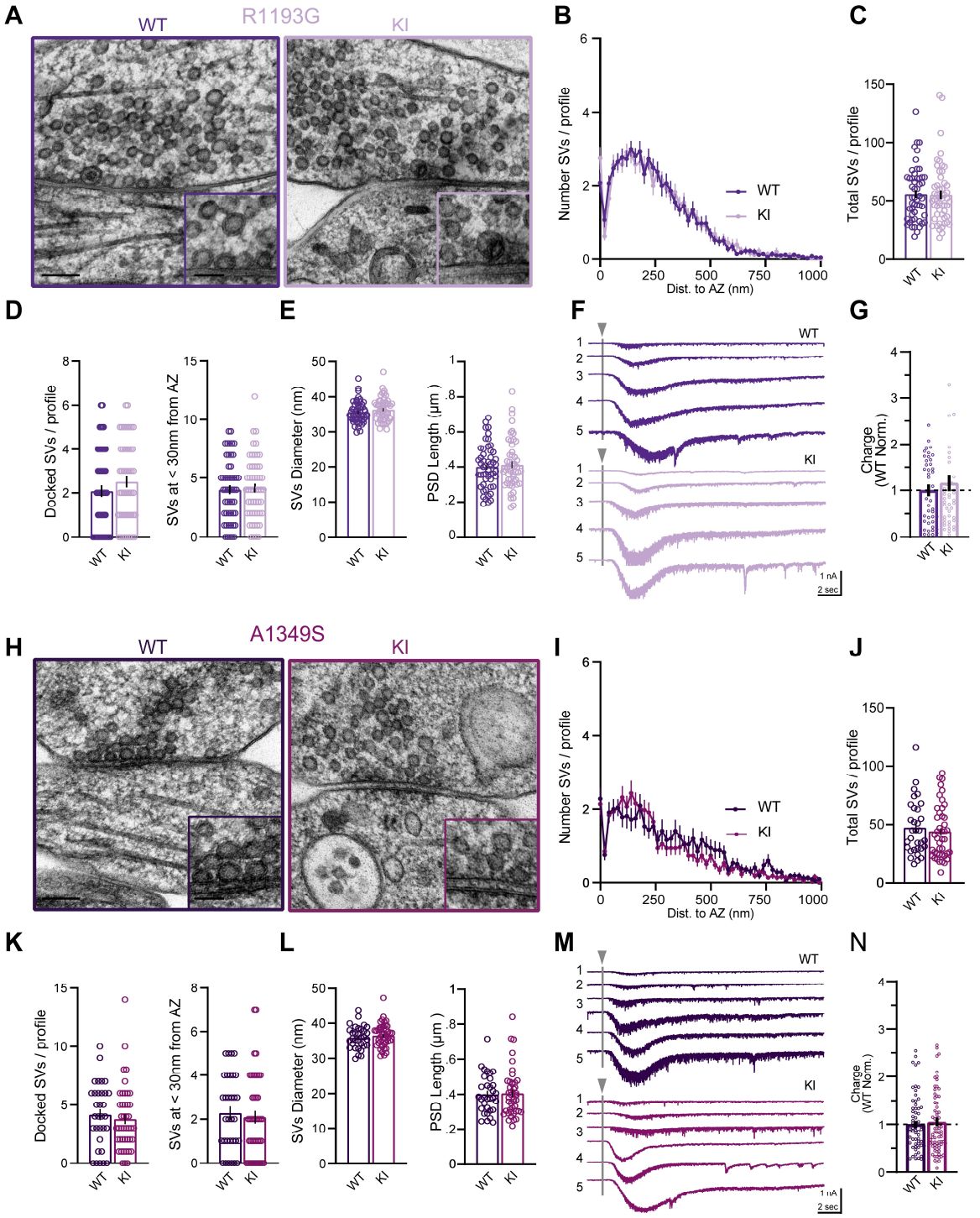
A
WT
R1193G
KI
B
Number SVs / profile
Dist. to AZ (nm)
WT
KI
C
Total SVs / profile
D
Docked SVs / profile
SVs at < 30nm from AZ
E
SVs Diameter (nm)
PSD Length (µm)
F
WT
KI
1 nA
2 sec
G
Charge (WT Norm.)
H
WT
A1349S
KI
I
Number SVs / profile
Dist. to AZ (nm)
WT
KI
J
Total SVs / profile
K
Docked SVs / profile
SVs at < 30nm from AZ
L
SVs Diameter (nm)
PSD Length (µm)
M
WT
KI
1 nA
2 sec
N
Charge (WT Norm.)

Figure S7. Normal synaptic ultrastructure in RIM1 R1193G and A1349S knock-in iGluts (previous page). Representative electron microscope images of high-pressure frozen RIM1 WT and RIM1 R1193G KI iGluts (A) and RIM1 WT and RIM1 A1349S (H). Quantification of the number of SVs per profile as a function of their distance from the AZ (B, I). Quantification of the total number of SVs per profile (C, J). Quantification of the number of docked SVs per profile. and of the number of SVs located within 30 nm of the AZ (D, K). Quantification of SV diameters and PSD length (E, L). Scale bars: 400 nm in main panels; 100 nm in insets N = 32-52/1 (profiles/batches). Schematics depicting recording setup for RRP and representative sucrose evoked current traces (F, M). Quantification of sucrose evoked total charge (G, N). N = 48-65/2-3 (cells/batches). Bar plots indicate the mean of the data. Error bars = SEM.

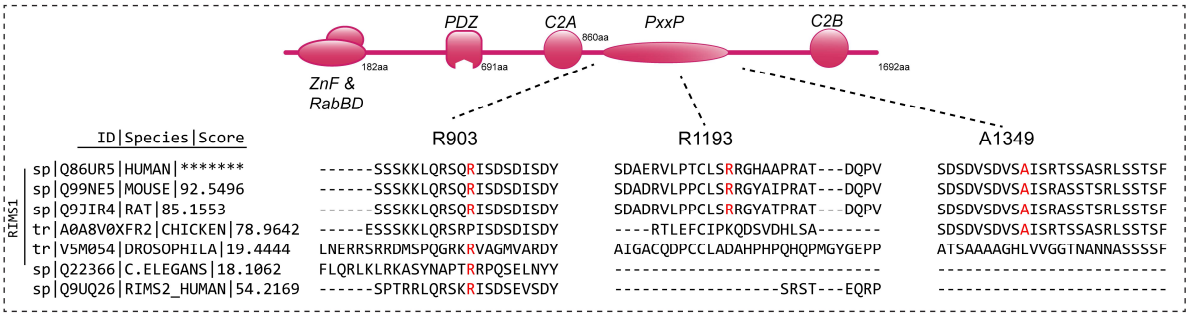

Figure S8. Conservation of ASD-Linked Missense Mutations in RIMS1 Across Mammals. Protein sequence alignment of human RIM1 with RIM1 from various species, as well as with human RIMS2, highlights the conserved regions surrounding the three ASD-associated missense mutations analyzed in this study.

Declaration

I hereby declare that I have prepared the dissertation ““Human presynaptic active zone: basic biology and disease”” myself and have not use any other sources than those explicitly mentioned.

I have not applied to be examined at any other institution, nor have I used the dissertation in this or any other form at any other institution as an examination paper, nor submitted it to any other faculty as a dissertation.

Heidelberg, 28.02.2025

Joaquín Damián Joacaz Campos Munoz

Contributions

The study here presented was only possible with the contribution from several people:

Dr. Acuna was fundamental for planning, implementing and reviewing this project.

Jennifer Baltazar carried out the targeting of mutation T396F.

Jana F. Tegethoff and Dr. Moriz Mall performed MEA recordings and helped with western blots acquisition.

Some preliminary patch-clamp recordings were performed by Dr. Claudio Acuna, Jennifer Baltazar and Fiona Freyberger. The experiments performed by Jennifer Baltazar and Fiona Freyberger were not included in the final analyses presented in this thesis. The experiments performed by Dr. Acuna were included in the Figure 8.

Dorothea Shall and Dra. Simone Berkel performed NSCs-NPCs neuronal differentiations.

Dra. Annarita Patrizzi and Matthias Schick at the DKFZ provided help with ddPCR.

Dra. Charlotta Funaya and Linda Wiest at the Heidelberg University EMCF carried out EM sample preparation and trained me in the use of EM microscopes.

Dr. Holger Lorenz trained me in the use of confocal and STED microscopes and provide advice for STED and live cell imaging.

Acknowledgments

The journey that comes to an end with this thesis has been, above all, a happy adventure. Even though it was marked by a pandemic, the loss of my father, and the challenges of a chronic illness, I cannot think of a better or more meaningful period in my life. This is largely thanks to the incredible people who surrounded me and made this odyssey one worth remembering.

First, I want to express my deepest gratitude to my PhD mentor, Dr. Claudio Acuna, for his trust, guidance, and continuous support. His ambition, rigor, creativity and cheerfulness played a fundamental role in shaping both my scientific work and personal growth. Without his influence, this journey would have been much harder—and far less rewarding.

I am also sincerely grateful to Dra. Schrenk Siemmens, Dr. Moritz Mall, and Dr. Amit Agarwal for their support and insightful advice, both in scientific discussions and on a personal level. Their guidance has been invaluable, and I deeply appreciate the time and effort they dedicated to helping me along the way.

I would like to thank my examiners and members of my Thesis Advisory Committee: Prof. Dr. Gudrun Rappold and Prof. Dr. Thomas Koch for their consistent support and will to improve my project. I truly appreciate the gift of their time in every meeting we had. Also I would like to sincerely thank Prof. Dr. Shaaf for graciously accepting the invitation to evaluate this work with great kindness and professionalism.

From my laboratory, I want to thank Gabriela and Chiara for their support, their openness to collaboration, and for always being willing to discuss science. To Dorothea, whose contributions were instrumental to give this project more validity. And to Felipe and Ram from Amit's lab—your generosity with reagents, equipment, and knowledge made a real difference, and I am truly grateful.

Beyond the lab, I owe a special thanks to my BJJ teammates and to HJC for all the fun and good energy. Words fall short in describing how each rolling session nourished both my body and spirit.

To my closest friends, Felipe, Tomás, Pablo, and Dennis, thank you for always reminding me that no beer ever tastes as good as the ones shared with old friends. Your company has been a constant source of joy and laughter.

To my siblings, Salomé, Vicente, and Miel—I love and admire you deeply. And to my mother, Andrea—your wisdom and kindness have been a constant source of strength, and I will always be grateful for your unwavering support.

Finally, to my wife, Belén Pinto—my partner in everything. Your patience, encouragement, and belief in me have been my greatest motivation. None of this would have been possible without you.